Title
Towards a Wireless Pacing System for Vascular Implantation

Author
Abiri, Parinaz

Publication Date
2019

Peer reviewed|Thesis/dissertation

UNIVERSITY OF CALIFORNIA

Los Angeles

Towards a Wireless Pacing System for Vascular Implantation

A dissertation submitted in partial satisfaction of the

requirements for the degree Doctor of Philosophy

in Bioengineering

by

Parinaz Abiri

2019

ABSTRACT OF THE DISSERTATION

Towards a Wireless Pacing System for Vascular Implantation

by

Parinaz Abiri

Doctor of Philosophy in Bioengineering

University of California, Los Angeles, 2019

Professor Tzung K Hsiai, Chair

Over 1 million patients are implanted annually with a pacemaker for the treatment of cardiac arrhythmias and conduction disorders. However, despite numerous advancements in pacemaker technology, lead-related complications associated with these devices continue to compromise patient safety and survival. Wireless power transfer holds great promise for improving health outcomes in biomedical implants such as the pacemaker. However, efficient power transfer and effective operational range have remained a challenge within anatomical constraints. In this work, we demonstrated an intravascular, wirelessly-powered, batteryless, microscale pacer deployed to the anterior cardiac vein (ACV). First, we employed a novel intermittent transmission remote-control architecture with improved power efficiency to enable sufficient power transfer without compromising on Specific Absorption Rate (SAR). We then integrated this architecture into a 3-tiered, 2-sub-system, 4-coil design, which operates on two different frequencies. Our pacemaker was designed to achieve wireless power transfer over a 55 mm range from an external transmitter to an intravascular receiver. A charging sub-system was designed to transmit power over 25 mm using inductive power transfer to a subcutaneous receiver, which then charged a battery feeding

the transmitter of a stimulation sub-system. We then introduced a stimulator circumferentially confined to a 3 mm diameter hollow-cylinder that delivered >5 V using wireless power transfer at 13.56 MHz, with over 20 mm transmitter-receiver displacement between the subcutaneous unit and pacer unit. Further validation was performed using Finite Element Method (FEM) simulation of the cardiac cycle, guided by anatomical variations established by Magnetic Resonance Images (MRI). Finally, we demonstrated the capacity for both *ex vivo* and *in vivo* pacing of pig hearts following pacer deployment in the ACV. This introduced, for the first time, the unprecedented capacity for wireless intravascular pacing with potential for multi-organ stimulation. Thus, the proposed system design has the potential to bypass the multitude of complications associated with pacemaker wires, repeated procedures for battery replacement, and mechanically burdened fixation mechanisms.

The dissertation of Parinaz Abiri is approved.

Yu-Chong Tai

Alireza Khademhosseini

Linda L Demer

Peyman Benharash

Tzung Hsiai, Committee Chair

University of California, Los Angeles

2019

Dedicated to my beloved parents

and incredible brothers.

TABLE OF CONTENTS

LIST OF FIGURES

LIST OF TABLES

ACKNOWLEDGEMENTS

I would like to thank my amazing advisor, Dr. Tzung Hsiai, whose extraordinary support, mentorship, and guidance has made my graduate experience truly rewarding and very memorable. His trust in me to initiate my own project without any background in the subject and only a promise of dedication was an unbelievable support and was the encouragement that pushed me forward in my project. His endless dedication to his students has been a powerful catalyst in my educational endeavors. His life teachings have also been especially enlightening as I pursue my career goals.

Of course, this project would not have been possible without the amazing support, advice, and encouragement of my many other mentors. Dr. Yu-Chong Tai has been my greatest challenger and inspiration in making engineering leaps. Dr. Linda Demer has been my idol physician scientist whose perseverance and dedication has motivated my own career goals. Dr. Ali Khademhosseini has been my inspiration to think outside the box in any project or decision. Dr. Peyman Benharash has been an amazing influence on my learning how to take advantage of my medical background as a researcher. Finally, I want to acknowledge the late Dr. Warren Grundfest, who was an amazing mentor, not only to myself, but also many others throughout his extraordinary life as a physician, scientist, and educator.

I would also like to simply thank all of my committee members for their valuable feedback and interest in my work for the past few years.

Additionally, I would like to thank the many other scientists, engineers, and clinicians who supported me on this project and helped make this investigation possible, specifically, Dr. Alireza Yousefi, Dr. Sandra Duarte-Vogel, Dr. Adam Abiri, Dr. Shervin Moloudi, Arash Abiri, Varun Gudapati, Tzu-Chieh Chou, Dr. Kim-Lien Nguyen, Dr. Malcolm Bersohn, Dr. Dejan Markovic, Mehrdad Roustaei, Usama Anwar, Dr. Jeffrey Hsu, Dr. Jianguo Ma, Dr. Rene Packard, Dr. Yichen

Ding, and Dr. Yuan Luo. It would not have been possible to build this project from ground-up without the amazing multidisciplinary mentorship provided by this amazing group of scientists.

I would also like to thank my lab mates, colleagues, and friends for their continuous support, valuable feedback, and assistance throughout these past years. Their persistent support and listening skills made our lab an amazing workplace surely to be missed.

Finally, I would like to acknowledge the generous funding provided by National Institute of Health's National Heart, Lung, and Blood Institute (NHLBI) and National Institute of General Medical Sciences (NIGMS) as well as the UCLA MSTP David Geffen Scholarship.

VITA

Education

- MD, UC Los Angeles, June 2021 (expected)
- PhD in Bioengineering, UC Los Angeles, June 2019 (expected)
- MS in Bioengineering, UC Los Angeles, December 2016
- BS in Biomedical Engineering, UC Irvine, June 2013

Honors & Awards

- Oral Presentation Winner in Bioengineering Research Day Competition, UCLA, 2019
- 1st Prize in Department of Medicine Research Day Poster Competition, UCLA, 2018
- 2018 Grad Slam Finalist, UCLA, 2018
- David Geffen UCLA MSTP Scholarship, UCLA, 2013
- Summa Cum Laude, UC Irvine, 2013
- Multidisciplinary Design Program Fellowship, UC Irvine, 2011

Work Experience

- Founder, **PulseMed Inc**. (02/16-present)
- Graduate Student Researcher, **UCLA Cardiovascular Engineering Lab** (06/15-06/19)
- ASUCLA Communication Board Member, **ASUCLA** (09/17-06/19)
- Intern, **Medtronic Inc**. (04/11-10/15)
- Undergraduate Student Researcher, **UCI BioMEMS Lab** (01/10-05/13)
- Intern, **Prediction Probe Inc**. (07/08-06/11)

Volunteer Experience

- Volunteer, **Anatomy Academy** (11/18-present)
- Volunteer, **Kid KiPOW** (12/18-04/19)
- Volunteer, **Kaiser Permanente** (06/11-03/13)

Peer-Reviewed Publications

- **Abiri P**, *et al*. A Three-Tiered Wireless Pacemaker with Optimized Coil Design. *In Revision*.
- **Abiri P**, *et al*. Multi-Dimensional Analysis of a Novel Approach for Wireless Simulation. *In Revision*.
- **Abiri P***, Luo Y* *et al*. Non-Invasive Electrical Impedance Tomography for Multi-Scale Detection of Liver Fat Content. *Theranostics* 2018; 8(6):1636-1647.
- **Abiri P**, *et al*. Inductively Powered Wireless Pacing via a Miniature Pacemaker and Remote Stimulation Control System. *Scientific Reports* 2018; 7(1): 6180.
- Abiri A*, Ding Y*, **Abiri P**, *et al*. Simulating Developmental Cardiac Morphology in Virtual Reality Using a Deformable Image Registration Approach. *Annals of Biomedical Engineering*. 2018 Dec;46(12):2177-2188.
- Abiri A*, Ding Y*, **Abiri, P**, *et al*. Integrating light-sheet imaging with virtual reality to recapitulate developmental cardiac mechanics. *JCI Insight*. 2017; 2(22):e97180.
- Packard RRS, Luo Y, **Abiri P**, *et al*. 3-D Electrochemical Impedance Spectroscopy Mapping of Arteries to Detect Metabolically Active but Angiographically Invisible Atherosclerotic Lesions. *Theranostics* 2017; 7(9):2431-2442.

- Hsu YH, Moya ML, **Abiri P**, Hughes CW, George S, Lee AP. Full Range Physiological Mass Transport Control in 3D Tissue Cultures. *Lab on a Chip*. 13(1): 81-9. 2013.
- Ding Y, Lee J, Ma J, Sung K, Yokota T, Singh N, Dooraghi M, **Abiri P**, Wang Y, Kulkarni R, Nakano A, Nguyen T, Fei P, Hsiai TK. Light-sheet fluorescence imaging to localize cardiac lineage and protein distribution. *Scientific Reports*. 7: 42209. 2017
- Ma J, Luo Y, Packard RRS, Ma T, Ding Y, **Abiri P**, Tai YC, Zhoug Q, Shung KK, Li R, Hsiai TK. Ultrasonic transducer-guided electrochemical impedance spectroscopy to assess lipid-laden plaques. *Sensors & Actuators B-Chemical*. (2016): 154-161

Book Chapters

- **Abiri P**, *et al*. Wirelessly Powered Medical Implants Via Radio Frequency Electromagnetic Radiation. *Interfacing Bioelectronics with Biomedical Sensing*. Ed. Cao H, Ed. Coleman T, Ed. Khademhosseini A, Ed. Tzung TK. Springer. *In Press*.
- Luo Y, **Abiri P**, *et al*. Epidermal EIT electrode arrays for detecting fatty liver infiltration. *Interfacing Bioelectronics with Biomedical Sensing*. Ed. Cao H, Ed. Coleman T, Ed. Khademhosseini A, Ed. Tzung TK. Springer. *In Press*.
- Luo Y, Packard RRS, **Abiri P**, *et al*. Flexible intravascular EIS sensors for detecting metabolically active plaque. *Interfacing Bioelectronics with Biomedical Sensing*. Ed. Cao H, Ed. Coleman T, Ed. Khademhosseini A, Ed. Tzung TK. Springer. *In Press*.

Patents

- **Abiri P**, *et al*. Multi-Tiered Wireless Powering System for Long-Term Implantable Medical Devices. The Regents of the University of California, assignee. *Patent Pending*.
- Hsiai TK, Tai YC, Packard RRS, Luo Y, **Abiri P**. A Method for the 3D characterization of vascular plaque using electrochemical impedance spectroscopy. *Patent Pending*.

Selected Presentations

- **Abiri P**, *et al*. In Vivo Detection of Metabolically Active Plaque using 3D Electrochemical Impedance Spectroscopy. *Biomedical Engineering Society Annual Meeting*. Atlanta GA. 2018.
- **Abiri P**, *et al*. A Wireless Pacing System Miniaturized for Vascular Implantation. *38th Annual Conference of the IEEE EMBC*. Honolulu, HI. 2018.
- **Abiri P**, *et al*. An Ex Vivo Study of an Inductively Powered Remote-Controlled Miniature Pacer. *Biomedical Engineering Society Annual Meeting*. Phoenix, AZ. 2017.
- **Abiri P**, *et al*. Inductive Power Transfer System for a Wireless Batteryless Miniature Implantable Cardiac Pacer. *38th Annual Conference of the IEEE EMBC*. Orlando, FL. 2016.
- **Abiri P**, *et al*. Data Analysis Automation and Software Integration to Increase Process Efficiency. *Annual Medtronic Science & Technology Conference*, Minneapolis, MN. 2013.
- **Abiri P**, *et al*. Medical Device Reconstruction Software Within a .Net Framework, *Annual Medtronic Science & Technology Conference*, Minneapolis, MN. 2012.
- **Abiri P**, *et al*. Intravascular Deployment of a Wirelessly Powered Leadless Micro-Pacer. *Cardiology Grand Rounds (Invited Talk)*, Los Angeles, CA. 2018.
- **Abiri P**, *et al*. A Next Generation Implantable Device: A Wirelessly Powered Intravascular Pacer. *IEEE EMB Buenaventura Chapter (Invited Talk)*, Los Angeles, CA. 2019.
- **Abiri P**, et al. Introducing a Wirelessly Powered Miniaturized Intravascular Pacer. *Health Lectures UCLA (Invited Talk)*. Los Angeles, CA. May 2019

1. INTRODUCTION

1.1. BACKGROUND

Implantable permanent cardiac pacemakers have saved millions of lives over the past five decades since their introduction. However, these devices continue to compromise patient health and safety as a result of functional limitations that impact structural stability. A cardiac pacemaker consists of a pulse generator, which contains all the circuitry and battery, and leads, which are wires that transmit current generated at the pulse generator to the tip electrodes that then stimulate the cardiac muscle tissue (**Figure 1**). Pacemakers are implanted either subcutaneously or submuscular through an incision made near the shoulder. The leads are then commonly inserted through the subclavian vein into the cardiac chambers, where they are fixated either passively or actively. In passive fixation, the lead is held against the endocardial trabeculae through tines that grab onto linings of the heart. In active fixation, the lead is fixated through a helix that screws into the cardiac tissue.

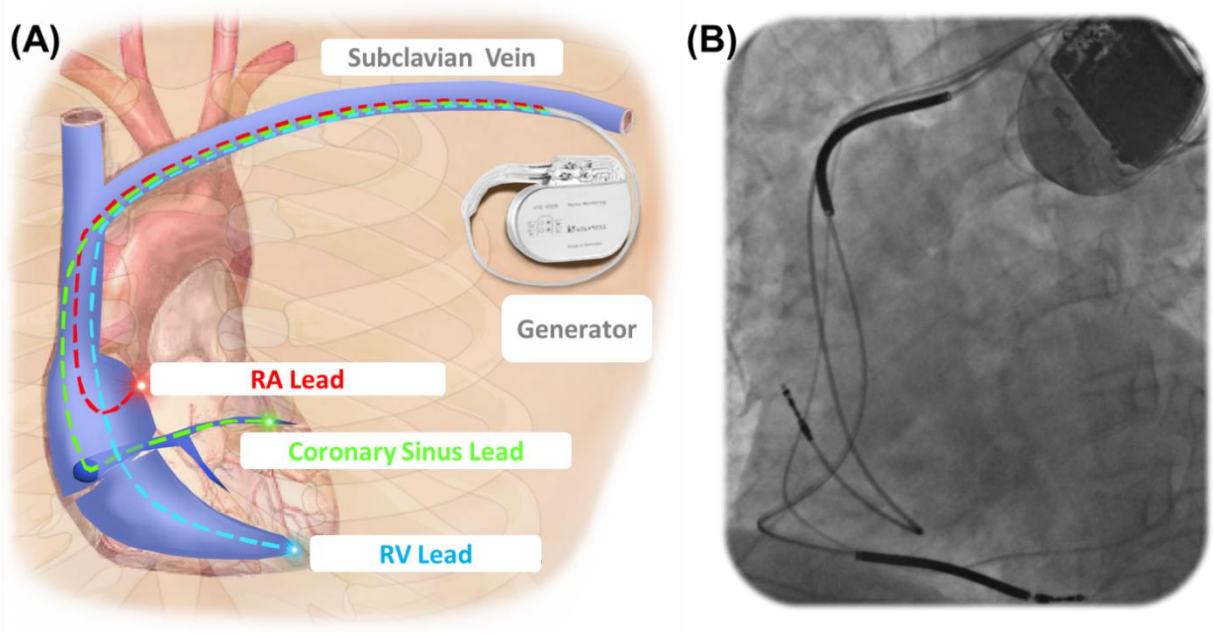

Figure 1: Current Pacemaker Technology. (A) Illustration of pacemaker pulse generator and various leads traversing the vessels to enter the cardiac chambers; a pacemaker can have multiple leads for pacing and sensing to be positioned accordingly for single-chamber or dual-chamber pacing [P1]. (B) Chest radiograph of a patient with an implant with pulse generator and connected pacing and sensing leads [P2].

While pacemakers of this form have been implanted in patients every day for decades, these devices are not short of complications. Over 1 million patients are currently implanted with a pacemaker annually with nearly one-in-ten of these patients experiencing lead-associated complications [1], [2]. With an increasing number of implants performed yearly under dozens of indications, including sinus node dysfunction, atrioventricular block, post-myocardial infarction, post-cardiac transplantation, tachycardia prevention, congenital heart disease, bifascicular block, and more, there is an urgent clinical need to minimize the complications associated with pacemaker implants.

These complications may include lead dislodgement, extracardiac stimulation, vascular occlusion and hemorrhaging, and electrical abnormalities that develop as a result of insulation breaks and conductor coil fracture [3], [4] (**Figure 2A**). Lead implants additionally increase the risk for infection to the heart valves and erosion of the conduction fibers [5]. Other complications include tissue puncture during the implant procedure, causing perforation and rupture of the heart or air entrapment in the lungs known as pneumothorax [6]. The complications may often be life-threatening and lead to additional surgeries in patients who can range from very young children to elderly adults. Despite this long list of problems that would ideally be resolved by device replacement, these complications are compounded by immune-mediated responses that render lead extraction dangerous [7]. Once implanted, the pacemaker lead-tissue interface develops fibrosis and adhesion to the surrounding tissue, rendering lead removal a life-threatening procedure [7] (**Figure 2B**). If lead extraction is deemed more dangerous than desertion, additional leads are implanted and the defective device is simply abandoned in the body with the potential to induce additional complications in the future [8].

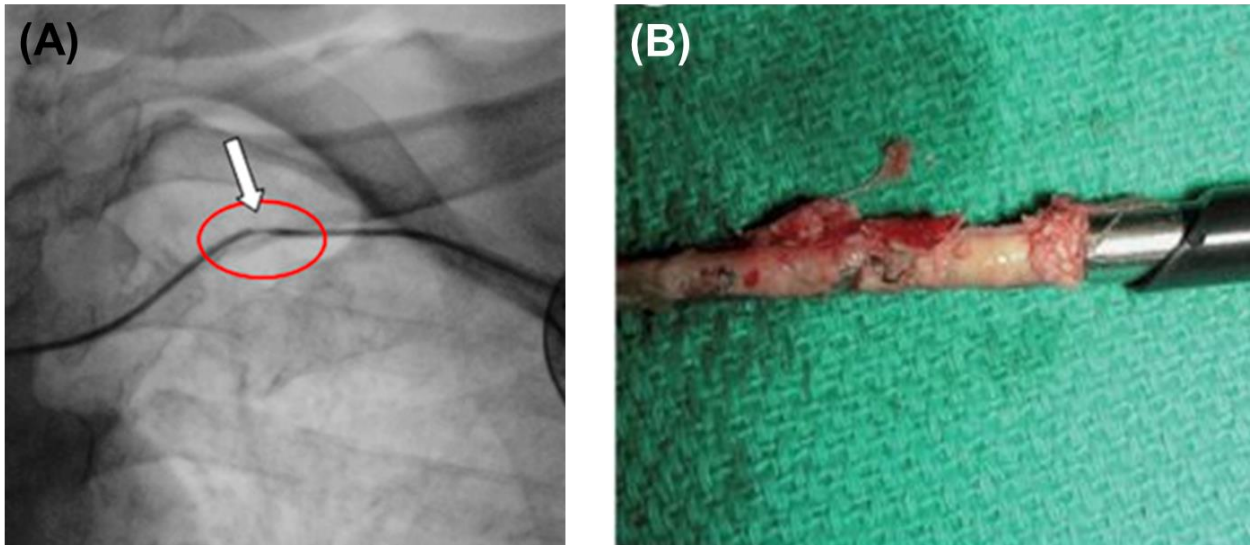

Figure 2: Pacemaker Lead-Associated Complications. (A) Insulation break of pacemaker lead as a result of medial subclavicular musculotendinous complex [9][P3]. (B) Fibrosis surrounding extracted pacemaker lead, resulting in life-threatening removal procedure [10].

Due to these concerns, in recent years, there has been a shift to focus on the elimination of leads in permanently implanted medical devices. Eliminating these wires significantly minimizes many lead-related complications. In addition to pacemakers, implantable stimulators, including neuromodulation devices used for spinal cord, deep brain, and peripheral nerve stimulation, are confined by the same lead-based architecture. Thus, developing wireless power transfer for a variety of implantable devices, including the pacemaker, has the potential to mitigate a host of device-related complications.

1.2. Alternatives to a Lead-Based System Designs

To address lead-related complications, battery-based leadless pacemakers have been introduced [11] (**Figure 3A**). Most recently, the FDA approval of the Medtronic Micra has marked a positive step towards leadless devices. However, integrating a battery with the pacer body increases device size and weight [11]–[13]. Large deployment catheters limit patient accessibility and increase

fluoroscopy time [12], [13]. Furthermore, repetitive mechanical burden also develops on the fixation anchor in the myocardium, thus risking embolization. Similar to lead-associated complications, device extraction is hazardous in case of end of device shelf-life or malfunction (**Figure 3B**). In the case of battery exhaustion or device failure, an additional pacemaker implantation is indicated in the already space-limited cardiac chambers [12], [13]. An FDA report has further revealed the risk for right ventricular (RV) perforation, pericardial effusion, and device embolization [12], [13].

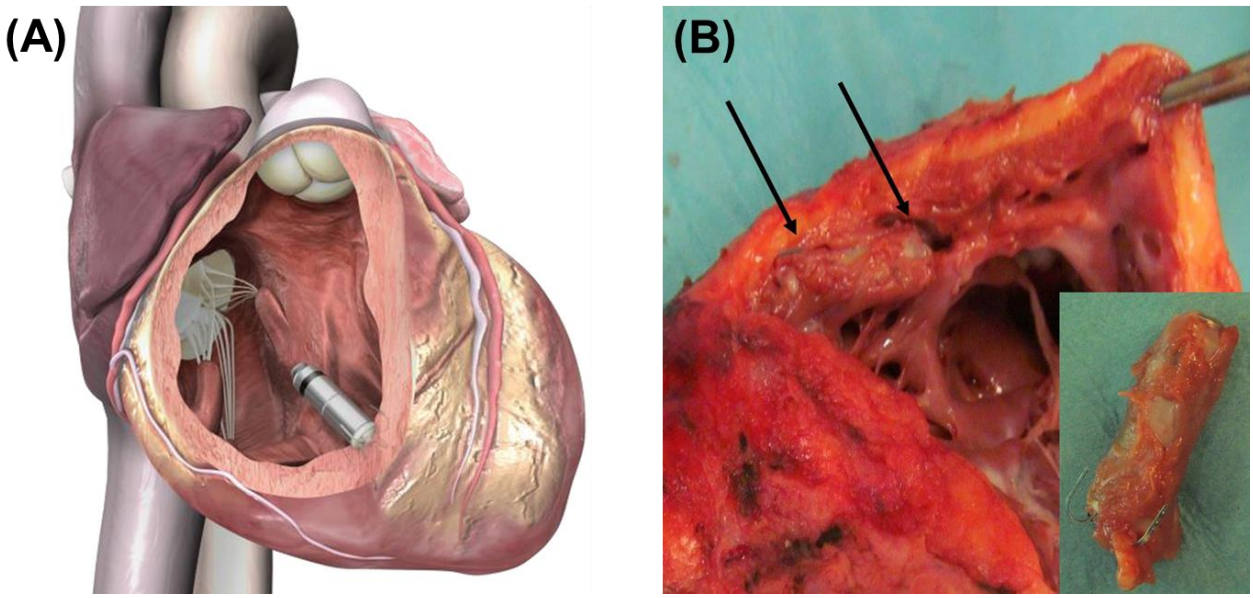

Figure 3: Leadless Pacemakers. (A) Medtronic Micra leadless pacemaker implanted in the right ventricular apex and fixated via tines attached to the distal end of the device [14]. (B) Fibrosis developed surrounding the leadless pacemaker as a result of immune response four months after device implantation [15].

Alternative solutions for leadless devices have been proposed, including utilization of energy harvesters of mechanical energy [16]–[19] and acoustic energy [20]–[23] (**Figure 4**). However, these solutions are limited by size requirements and reliance on an endocardial anchor,

invasive epicardial fixation, dependency on multiple implants and incisions, and/or insufficient energy harvesting for pacing.

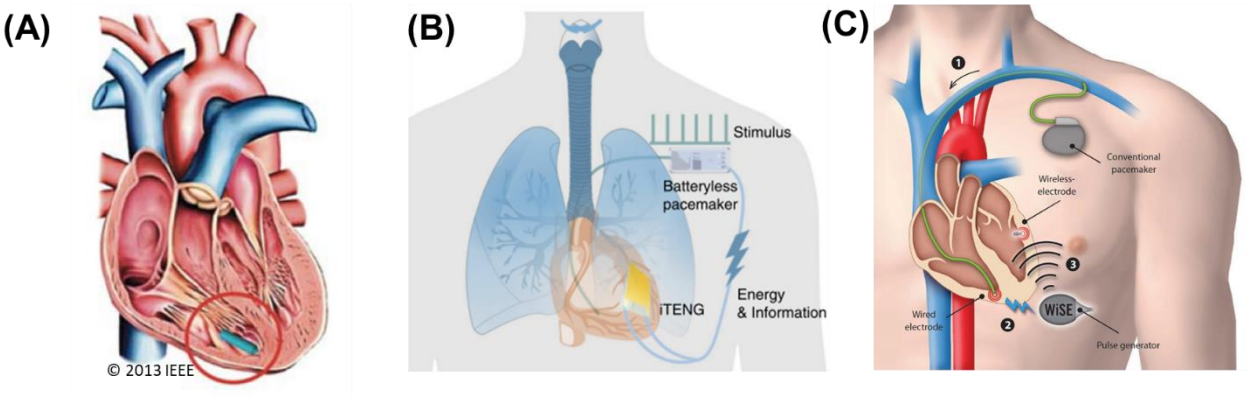

Figure 4: Research in Leadless Pacemaker Technology. (A) Endocardial energy harvester of mechanical motion [24]. (B) Epicardial energy harvester of mechanical motion [25]. (C) Energy harvester of ultrasound with four implants and incisions [20].

1.3. RF-Based Wireless Power Transfer Systems

Recent years have placed much focus on power harvesting through radio frequency (RF), with the potential to produce sufficient energy for long-term implants. While this technology was developed over a century ago and has been used in practice for years in consumer electronics as well as theorized for charging of electric vehicles, its utilization in medical devices has been limited due certain inherent challenges that result from anatomical constraints that limit sufficient wireless power transfer.

1.3.1. Far-Field Wireless Power Transfer

Far field wireless power transfer is a well-known technology for providing real-time power to electronic devices, with a recent growing interest in powering medical implants. Far-field is defined as RF transmission to a receiving antenna that is more than a few wavelengths away from

the transmitting antenna [26]. This distance results in the decoupling of the transmitter from the receiver; thus, the receiver has no impact on the transmitter's radiation field [27]–[29]. In far-field, the radiation field is uniform (assuming a uniform radiator) in shape with the electric (E) field moving orthogonal to the magnetic (M) field. Furthermore, the radiative power decreases in strength much more slowly compared to other forms of RF transmission, where the power density (i.e. Poynting vector [27]) of electromagnetic radiation decreases as a function of the square of the distance:

$$S = \frac{P_t}{4\pi R^2} \tag{1}$$

where S is the power density, P_t is the transmitted power, and R is the distance from the lossless isotropic (uniformly-radiating) transmitter antenna.

Another advantage of the far-field approach lies in the ability to design the antenna such that it radiates more strongly in a specific direction. For example, the power beam can be focused using an array of antennas or dish antennas. It is important to note that the far-field approach has lower efficiency in water-rich environments, such as biological tissues. The power transfer efficiency in far-field is described in [29], and can be decomposed into three power conversion efficiency components:

$$eff = \frac{P_{dc}^r}{P_{dc}^t} = \frac{P_{rf}^r}{P_{dc}^t} \times \frac{P_{rf}^r}{P_{rf}^t} \times \frac{P_{dc}^r}{P_{rf}^r} \tag{2}$$

where $\frac{P_{rf}^r}{P_{dc}^t}$ is the DC-to-RF (frequency up-conversion form DC to a designated high frequency) conversion efficiency at the energy transmitter, $\frac{P_{rf}^r}{P_{rf}^t}$ is the RF-to-RF transmission efficiency (i.e.

medium loss), and $\frac{P_{dc}^{r}}{P_{rf}^{r}}$ is the RF-to-DC (conversion down-conversion from high frequency to DC) conversion efficiency at energy receiver (e.g. rectenna [30]). The chief bottleneck in medical applications is the RF-to-RF transmission efficiency due to losses through the medium consisting primarily of water. This efficiency can, however, be improved by directional transmission and beam-forming.

Due to the long-range radiative nature of far-field power harvesting, safety considerations are significant in its application to medical devices. The use of power harvesting using far-field electromagnetic waves in medical devices has been studied by a few investigators. Bakogianni *et al* examined the efficiency of a power link at various sub-1 GHz frequencies (433 MHz, 868 MHz, 915 MHz), noting optimal reliability at the highest frequency of 915 MHz at which -5dBm power level is achieved at 40 cm distance and transmitter output of 30 dBm [31]. Liu *et al* analyzed the safety considering for an implantable rectenna (rectifying antenna) for far-field wireless power transfer using a planar inverted-F antenna in combination of a parasitic patch for improved power harvesting efficiency. The proposed system (Rx = 3 x 8 mm, Patch = 4 x 8 mm) was shown to achieve a power level of -11 dBm at an operating frequency of 2.45 GHz and distance of 0.5 m [32]. While Bakogianni *et al* and Liu *et al* were both able to develop a miniature implant, the received power was insufficient for direct stimulation for cardiac pacing or alternatively demanded an integrated charge storage unit, such as a battery, for long-term power harvesting. Sun *et al* presented a batteryless wirelessly powered pacemaker that harvested energy at 9 GHz. A miniature receiver chip (Rx = 4 mm x 1 mm) was thus presented with which a 1.3 V stimulation pulse was initiated at 2 cm distance between the transmitting and receiving units [33]. This system, however, was designed with an inherent interdependency between pulse rate, pulse duration, and voltage threshold, thus creating a limitation for cardiac pacing applications.

Overall, while far-field is a promising technology for wireless power transfer, it continues to suffer from the inability to provide sufficient power without exceeding tissue absorption or anatomical size limits.

1.3.2. MID-FIELD WIRELESS POWER TRANSFER

Mid-field utilizes a combination of inductive and radiative modes. The idea of mid-field powering was only recently given prominence by Dr. Ada Poon, whose research has focused on increasing wireless power transfer efficiency to very small implants inside the body [34], [35]. In their numerical studies of the mid-field approach, they demonstrated that it can be an efficient way to transfer power to deep implants in the body despite millimeter-sized receiver antennas.

In their mid-field approach, the human body is considered to be a multi-layer tissue model, where each layer has specific EM wave propagation characteristic. By optimizing the physical realization of the source planar antenna, they attempted to achieve the highest efficiency for delivering power to a small receiver coil in the body. They rewrote the efficiency equation as the function of current density J_S on the source (planar structure) and dyadic Green's functions G_E and G_H (defined as $\boldsymbol{E}(\boldsymbol{r}) = i\omega\mu\int \bar{\boldsymbol{G}}_{\boldsymbol{E}}(\boldsymbol{r}-\boldsymbol{r}')\boldsymbol{J}_{\boldsymbol{S}}(\boldsymbol{r}')d\boldsymbol{r}'$ and $\boldsymbol{H}(\boldsymbol{r}) = \int \bar{\boldsymbol{G}}_{\boldsymbol{H}}(\boldsymbol{r}-\boldsymbol{r}')\boldsymbol{J}_{\boldsymbol{S}}(\boldsymbol{r}')d\boldsymbol{r}'$, where E and H are electric and magnetic fields). They then worked towards reaching the maximum efficiency achievable by any arbitrary source surface current density J_S.

The source was then realized with a slot array structure. The patterned metal plate (slot array) was placed near the skin at sub-wavelength distances away from the small receiver coil. The ability to focus the field allowed a much smaller antenna to harvest a relatively larger amount of energy. As shown in Ho *et al*, a miniature cardiac implant (Rx = 2 mm diameter and 3.5 mm

height) was able to receive 200 uW of power at 5 cm distance from the transmitter (Tx = 60 mm x 60 mm) at 1.6 GHz operating frequency with 500 mW of input [34].

While mid-field wireless power transfer has made significant leaps in powering miniature medical devices, it continues to suffer certain limitations. Although continuous midfield powering has achieved 200 µW over a 5 cm while below SAR safety thresholds, this power output is only able to meet the requirements of a pacemaker chip (8 µW [36]), and not able to meet the up to 50 mW demands for direct cardiac stimulation. Increased power output via mid-field wireless power transfer would thus requires higher energy coupled into the system, which would surpass SAR limits.

1.3.3. Near-Field Wireless Power Transfer

Inductive power transfer occurs as a result of a changing electrical current that induces the formation of an electromagnetic field around a transmitting antenna (**Figure 5**). Near-field acts near the source antenna, formally defined as less than one wavelength (λ) away from the antenna [37]. This region can be separate into two areas: (1) the reactive zone, ranging up to $\lambda/2\pi$ distance, and (2) the radiative zone, ranging from $\lambda/2\pi$ to λ distance [26]. In the reactive zone, in which we primarily operate in near-field applications, either the electric (E) or magnetic (H) field dominate. In the commonly used loop antenna, the magnetic field is dominant [26].

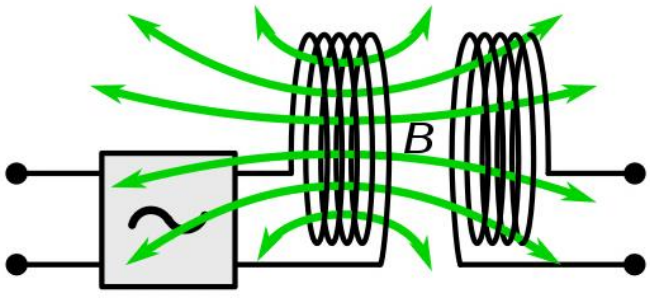

Figure 5: Illustration of Inductive Power Transfer Physics. Alternating current (AC) in a transmitting coil induces a magnetic field that generates a voltage in a nearby power receiving conductor [P4].

This magnetic field is then able to induce a voltage in a nearby conductor, thus transferring power wirelessly from one conducting system to another (**Figure 5**). When a transmitting coil and receiving coil interact in this phenomenon, they are said to be coupled by the magnetic field between them. The strength of the magnetic field from the transmitter antenna decreases rapidly in near-field, following the inverse-cube law over distance ($1/d^3$) [37]. This rapid decline has two implications: (1) power is contained within only a few wavelengths away from the source and any near-field effects are negligible further away; (2) the receiving coil must be within a small region to maintain power transfer efficiency from the transmitting to the receiving system.

In near-field, power transfer efficiency (PTE) is greatly dependent on the geometry of the transmitting and receiving coils as well as the distance and alignment between the coils. These dependencies cause some major challenges in the utilization of IPT in medical devices due to anatomical boundaries in the body that limit antenna size and introduce substantial variations in power transfer range and alignment. For example, in the case of neural implants, the receiver is often extremely limited in size; or, in the case of cardiac implants, the receiver faces the challenge of motion-induced variations in distance and alignment.

Finally, tissue energy absorption is also a significant player in IPT systems. Depending on the dielectric constant, a substance absorbs different amounts of energy. The level of tissue energy absorption depends on the tissue type (e.g. skin, fat, muscle, etc.) and the electric (E) field generated as a result of IPT. The strength of the E-field depends on the amount of power transferred and the frequency of transmission. The Federal Communication Commission (FCC) has

established SAR safety limits for humans at 1.6 W/kg averaged over 1 g. An IPT system must follow these guidelines [38].

Several different near-field system architectures have been established to deliver power wirelessly to a stimulation system, each to be discussed in the following sections.

1.3.3.1. BATTERYLESS DIRECT STIMULATION

In the first architecture to be discussed, power is transferred sequentially as follows:

1. Power supply (**Figure 6A**)
2. Transmitter unit with transmitter coil and circuitry (**Figure 6B**)
3. Receiver unit with receiver coil and circuitry (**Figure 6C**)
4. Control circuitry (**Figure 6D**)
5. Stimulation electrodes (**Figure 6E**)

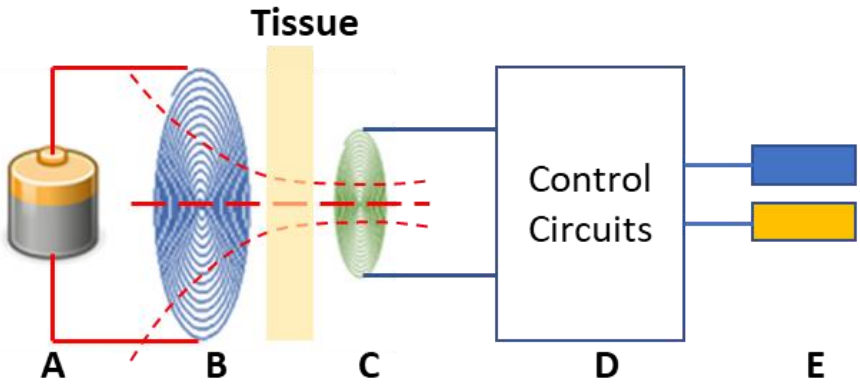

Figure 6: Batteryless Direct Simulation System Architecture. Power is wirelessly transferred from a transmitter coil to a receiver coil, then directly sent to the stimulating electrodes with rate and duration determined by a control circuity in the receiver.

This architecture defines the most direct method to transmit power from a remote power source. Power is delivered continuously from a transmitter (Tx) to the control circuitry in the receiver (Rx), where rate and duration of stimulation are then controlled based on pre-defined settings or sensor data input.

This structure is utilized in the vast majority of systems implemented in literature. Heetderks *et al* utilized this architecture in the analysis of power transfer efficiency for significantly large transmitter to receiver size ratios. Millimeter and submillimeter-sized neural implant receivers (Rx Ø = 0.4 – 1.5 mm, Length = 3 mm) were coupled to large transmitters (Tx Ø = 90 – 32 mm) at 2 MHz and 20 MHz operating frequency [39]. Given a 4 W power supply, 0.09 – 50 mW was received by the implant without accounting for displacement between the transmitter and receiver. Von Arx *et al* also described a fully-integrated neuromuscular electrical stimulation system (FITNESS) operating at 4 MHz (Tx Ø = 80 mm, Rx = 2 x 8 mm^2) and 30 mm distance between the transmitter and receiver, capable of delivering 20mW to the receiver [40]. Neagu *et al* similarly focused their design on a small receiver (Rx Ø = 4.5 mm). With transmitter and receiver coil separations of 1 mm and 3.5 mm and operating frequency of 3 MHz, they obtained a maximum system output of 2 mW [41]. In all cases, it can be seen that power transfer efficiency suffers severely as a result of small receiver size, either limiting the received power or range of transmission, or sacrificing on SAR regulatory compliance.

Larger receiver sizes can be more practical when needing higher power transfer efficiency but can also be limiting in implant location and device application. Ali *et al* designed an inductive link with larger a receiver coil (Tx Ø = 27 mm, Rx Ø = 12.6 mm) for medical implants at 2.5 MHz frequency and achieved 40 mW output while simultaneously transferring data at a rate of 128kbps [42]. Similarly, Li *et al* designed a wirelessly powered system for medical devices (Tx Ø = 25 mm,

Rx Ø = 9.5 mm) at 13.56 MHz and achieved 60 mW output and 92.5% efficiency at 3 mm coil separation [43]. Ghovanloo *et al* and Parramon *et al* were able to achieve longer range of power transfer at 10 mm and 15 mm, respectively [44], [45]. At 5 MHz and using larger receiver coils (Tx Ø = 40 mm, Rx Ø = 20 mm), Ghovanloo obtained 78% power transfer efficiency. Parramon increased operating frequency (10 MHz) and decreased coil sizes (Tx Ø = 20 mm, Rx Ø = 10 mm) to achieve 19 mW output. Monti *et al* took advantage of the same system design at a significantly higher frequency of 434 MHz (Tx Ø ≅ 68 mm, Rx Ø ≅ 33 mm), obtaining 51 mW at 1 cm and 10 mW at 2 cm given a power supply of 1 W on the transmitter side [46].

In summary, the batteryless direct stimulation design demands sacrifice in either size or efficiency. In the case of a small implant, the architecture faces the challenge of delivering sufficient power while remaining below SAR limits due to large power requirements for stimulation and inherent inefficiency in an asymmetrical IPT system. In the case of a large implants with increased efficiency, the architecture faces the challenge of meeting anatomical constraints for implant position.

1.3.3.2. BATTERY-BASED STIMULATION

In the second architecture to be discussed, power is transferred sequentially as follows:

1. Power supply (**Figure 7A**)
2. Transmitter unit with transmitter coil and circuitry (**Figure 7B**)
3. Receiver unit with receiver coil and circuitry (**Figure 7C**)
4. Energy-storage unit (**Figure 7D**)
5. Control circuitry (**Figure 7E**)

6. Stimulation electrodes (**Figure 7F**)

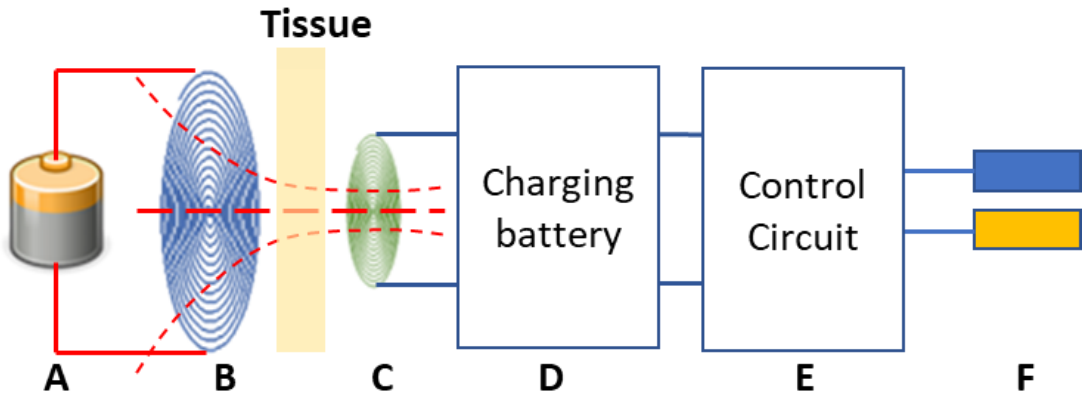

Figure 7: Battery-Based System Architecture. Power is wirelessly transferred from a transmitter coil to a receiver coil, then sent to a charge storage unit for energy harvesting; a control circuity in the receiver determined pulse rate and duration before sending power to the stimulating electrodes.

This architecture defines a high-reliability method to transmit power from a remote power source. Power can be transferred continuously or intermittently from a transmitter to an energy-storage unit (ESU), such as a small battery or capacitor, in the receiver. The ESU then delivers the power needed to feed the control unit as well as the stimulation pulse. Due to the intermediary presence of an ESU, the instantaneous power needed for stimulation does not need to be provided via the wireless connection, but rather from the ESU, thus allowing for more freedom in inductive power transfer system efficiency. This ability is important as it allows a lower efficiency system to be implemented, in which power is slowly accumulated to the necessary threshold and delivered when appropriate.

The battery-based architecture is valuable in cases in which there is sufficient space for an ESU and a low-efficiency system has to be tolerated despite the need for high instantaneous stimulation power. In Lee *et al*, a wireless cardiac defibrillator was designed using this architecture

due to the large power requirements for defibration. In their design, an inductive power transfer system delivered power to a rechargeable battery, which would then feed into a control system and stimulator circuitry [47]. Lee *et al* alternatively described an IPT system designed to charge a series of capacitors preceding delivery to a stimulator. Given a 2.7 Vpp input, the system (Tx Ø = 40 mm, Rx Ø = 10 mm) with a 2 MHz operating frequency was able to charge pairs of 1μF capacitors up to 2 V in 420 μs, achieving a high measured charging efficiency of 82% [48].

In summary, while the addition of a battery in the receiver enables power accumulation in a low-efficiency system for delivering sufficient power to deep tissue implants, it also entails an increase in device size that limits implant position and fixation. Furthermore, a system consisting of an ESU is limited by the amount of time needed to sufficiently charge the ESU in preparation for stimulation. Thus, there is interdependency between pulse duration, pulse rate, charge rate, and coupling efficiency.

1.3.3.3. MULTI-COIL STIMULATION

In the third near-field architecture to be discussed, power is transferred sequentially as follows:

1. Power supply (**Figure 8A**)
2. Transmitter unit with transmitter coil and circuitry (**Figure 8B**)
3. Relay coil (**Figure 8C**)
4. Receiver unit with receiver coil and circuitry (**Figure 8D**)
5. Logic circuitry (**Figure 8E**)
6. Stimulation electrodes (**Figure 8F**)

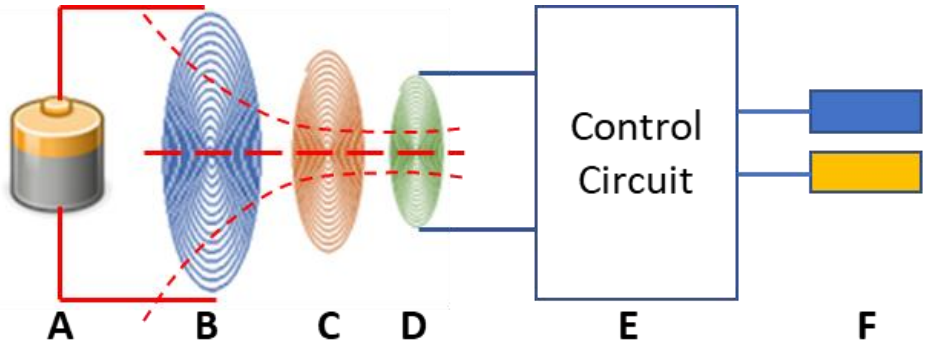

Figure 8: Multi-Coil Stimulation Architecture. Power is wirelessly transferred from a transmitter coil to a receiver coil, then directly sent to the stimulating electrodes with rate and duration determined by a control circuity in the receiver.

In this architecture, the presence of one or more intermediary relay coils can significantly increase power transfer efficiency of the IPT system. This design allows for higher efficiency where there is anatomical leniency for the presence of additional relay coils.

Kurs *et al* has presented a four-coil system defined by two primarily interacting coils called the "source" and "device" coils, and their interacting loop coils: one that is part of the driving circuit connected to the "source" (defined as "A") and one that is part of the load connected to the "device" (defined as "B"). The system was designed such that coupling aws primarily present between A and source, source and device, device and B. Their system was shown to transfer 60 W with 40% efficiency over 2 m of distance [49].

Ramrakhyani *et al* similarly described a four-coil structure in which the transmitting system consisted of a "driver" coil in proximity to a "primary" coil, and the receiving system consisted of a "secondary" coil in proximity to a "load" coil. Given a 700 kHz operating frequency over ranges of 10-20 mm (Rx Ø = 22 mm), power transfer efficiency in the four-coil system was shown to be 80% compared to the two-coil system at 40% [50].

In Lee *et al*, a 3-coil system was defined, in which a relay coil was only present in proximity of the secondary coil of the receiver. The local Rx loop allowed compensation for changes in load and coupling variations to improve power transfer efficiency. The overall power transfer efficiency was shown to be 10.5% and 4.7% greater than a similar open- and single closed-loop system [51].

Kiani *et al* compared the efficiency of a 4-coil system (2 relay coils), 3-coil system (1 relay coil), and 2-coil system (0 relay coils). At 13.56 MHz and 12 cm coupling distance, their experiments demonstrated higher efficiency in a 3-coil system, with 35%, 37%, and 15% efficiency in 2-, 3-, and 4-coil inductive links, respectively [52]. Finally, the placement of multiple coils in a domino format in coaxial and noncoaxial structures was analyzed by Zhong *et al*, in which unequal spacing between the subsequent coils was found to be more efficient than equal spacing [53].

In summary, while a multi-coil inductive power transfer system architecture allows for increased power transfer efficiency and range of wireless power transfer, it demands the implantation of multiple components whose relative positions must be optimized for maximum efficiency. These limitations may, therefore, hinder practicality in many medical applications in which the number of incisions must be minimized and anatomical constraints limit control over the positions of the implants.

2. DESIGN OF A MINIATURE PACING SYSTEM

Despite numerous advancements in the past few decades in medical device development for the treatment and diagnosis of disease, the ability to power these devices has not been able to keep up with the growing trend in miniaturization and adaptability. The need for large batteries, the danger and inconvenience of multiple surgeries for battery replacement, and the presence of long implanted wires that can cause life-threatening complications have been lingering limitations in the medical device world.

Previous work on wirelessly powered medical devices has often focused on improving coil-to-coil inductive power transfer efficiency. However, given the anatomical and physiological constraints for medical implants, there is a limited capacity for adjusting the variables that control the amount of power delivery in an inductively powered wireless system. To address both the size and absorption requirements, we sought to instead direct our design criteria towards the system architecture itself, specifically by minimizing the power-consuming functionalities and components of the wireless power receiving unit.

A pacing system was developed with two key design criteria: (1) to resolve the mechanical failure points in the fixation mechanism by extensive miniaturization of the pacer, and (2) to achieve sufficient wireless power transmission from the power source to the geometrically constrained pacer. The former would allow for implantation external to the cardiac chambers to avoid high intra-cardiac pressure gradients, while enabling intravascular deployment of the device to the anterior cardiac vein. The latter would be achieved without exceeding specific absorption rate (SAR) limits.

2.1. REMOTE-CONTROLLED STIMULATION

We designed an inductive power transfer system in which the pacer function was entirely controlled by intermittent power input into the wireless power transmitter tank circuit. The proposed wireless pacing system consisted of two physically isolated components as shown in the block diagram (**Figure 9A**) and circuit diagram (**Figure 9B-C**). The pacing unit was miniaturized by maintaining only the core essentials for delivering a stimulatory pulse to the myocardium. Therefore, it consisted of no internal control mechanism with its function being to act solely as a transformation unit, acquiring an AC input from the parallel resonant tank circuit to convert into a DC output for cardiac stimulation (**Figure 9C**). In addition, this pacing module did not encompass any charge storage unit, such as a battery or capacitor. The entirety of the functional components and control structure for the pacer was integrated into the transmitter, consisting of the control circuitry, class E power amplifier (PA), and series resonant tank circuit (**Figure 9B**). An analog switch would permit power delivery at the desired heart rate and pulse width for intermittent power transfer to the tank, and ultimately the receiver on the epicardium.

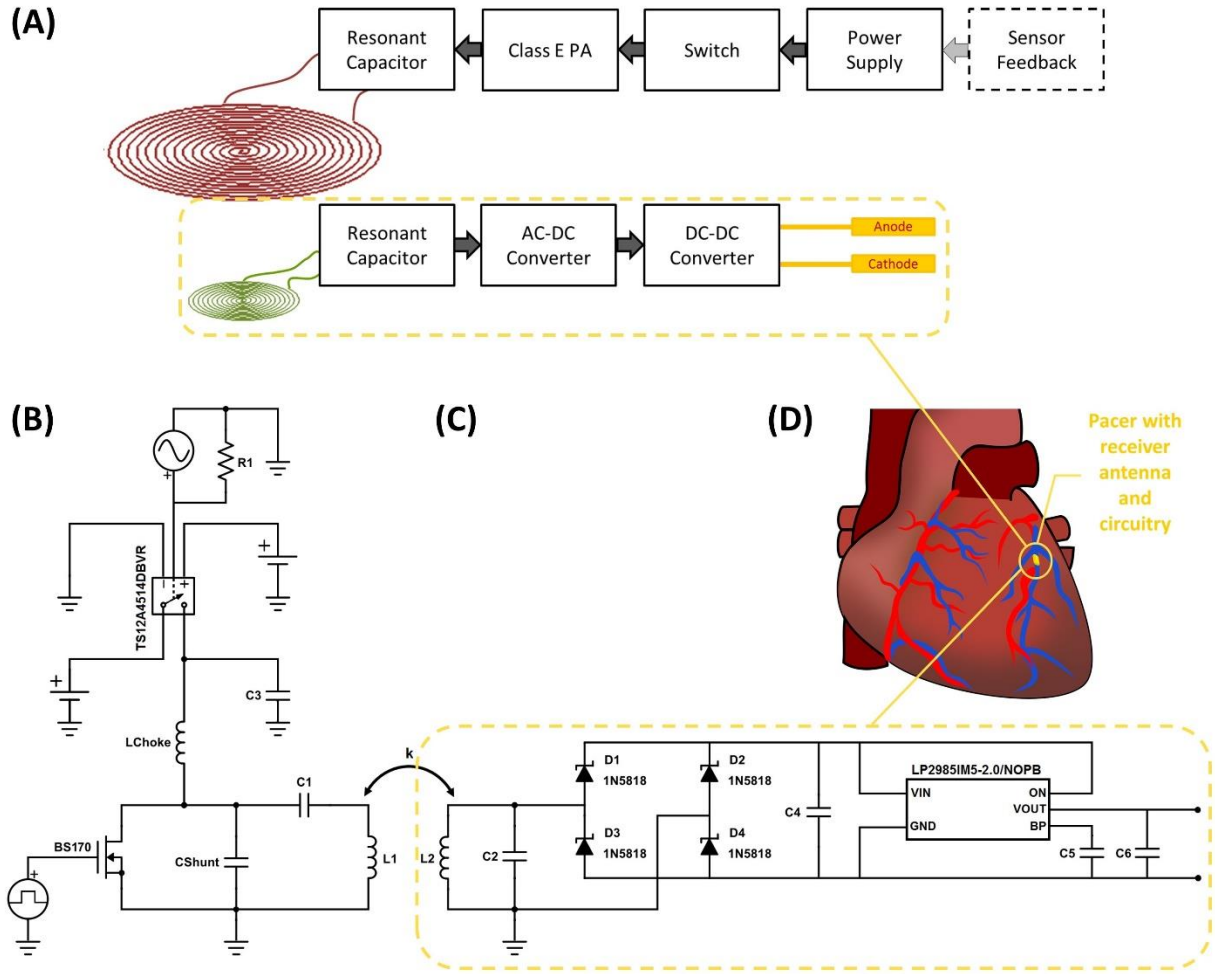

Figure 9: System Architecture. (A) A block diagram highlights the wireless pacing system with "remote-controlled" stimulation on the receiver side using intermittent power transfer from the transmitter side. (B) The transmitter circuitry consisted of the primary functional components of the pacemaker that remotely control and power the stimulator on the heart, including a switch, potential control input from a sensor, Class-E PA, and series resonant tank circuit. (C) The receiver circuitry consisted of only the components necessary to output a regulated voltage to the two electrodes, including a parallel resonant tank circuit, bridge rectifier, and voltage regulator. (D) A cartoon diagram depicts the pacer implant location into the anterior cardiac vein, which is made possible through miniaturization using a remote-controlled stimulation system.

In this architecture, power would be transferred sequentially as follows:

1. Power supply (**Figure 10A**)
2. Control circuitry (**Figure 10B**)
3. Transmitter unit with transmitter coil and circuitry (**Figure 10C**)
4. Receiver unit with receiver coil and circuitry (**Figure 10D**)
5. Stimulation electrodes (**Figure 10E**)

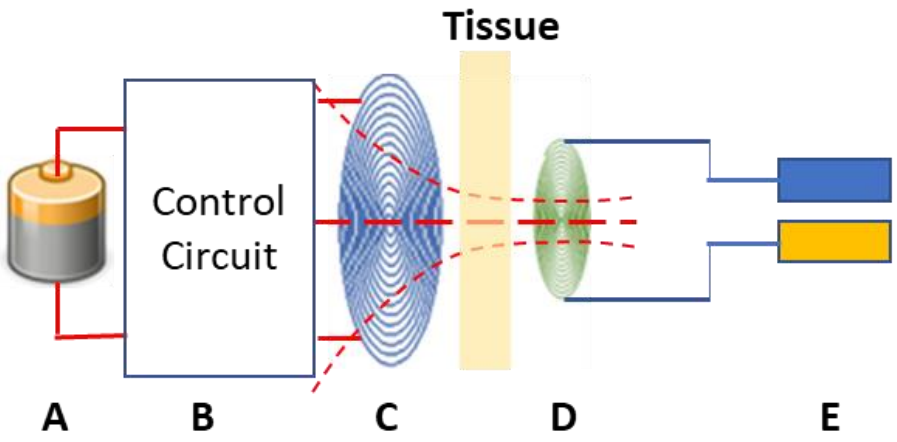

Figure 10: Remote-controlled stimulation architecture. Power is modulated through a control circuitry, which determines rate and duration before sending power to the transmitter coil. Feedback control from a sensor may be placed here. Power is then wirelessly transferred from a transmitter coil to a receiver coil, then sent directly to the stimulating electrodes.

Thus, pacing activity was entirely controlled remotely via intermittent power delivery from the transmitter at short pulses. In the case of cardiac pacing, pulse duration for stimulation (and thus wireless power transmission) would range between 0.2 to 1 ms. The pacer would enter "idle mode" during the non-stimulation period and switch to "active mode" during stimulation. In this work, we set the "active mode" duration to 1 ms. This stimulation duration is considered to be in

the upper range for an effective pulse width as a result of the leveling effect of the strength-duration curve [54]. At 60 beats per minutes (BPM), this 1 ms “active mode” would be separated by intervals of 999 ms in “idle mode.” Unlike continuous wireless power transmission, the receiver would not consume power during the prominent “idle mode” as there would be no power-consuming circuitry or function in the remote receiver during this period; this would effectively reduce the power consumption by 1000-fold. This reduction would be further amplified by a shorter pulse duration within a given time period. Therefore, the power efficiency is often improved by > 1000-fold as pulse duration typically ranges between 0.2 ms to 1 ms.

The advantages of separating the stimulator from the control system are thus four-fold. The first lies in the size reduction of the receiver through the removal of complex control circuitry. The second resides in the reduction in power requirements of the remote device. Wired transmission is far more power efficient than a wireless approach. Thus, by placing the majority of components inside the transmitting module with direct connection to a battery, the overall power requirements of the device were substantially reduced. The third advantage lies in a further reduction in power consumption via delivery of several short-pulse wireless transmissions as opposed to a single long transmission that continuously supplies the circuit or charges a small charge storage unit. This intermittent-type powering mechanism is achieved with the receiver designed only to function as a stimulator with greater than 99.9% inactivity and with less than 0.1% of the time during which power is needed for pacing. In contrast, inclusion of additional functions would require continuous power supply. Consequently, while 99.9% of the time the pacer would be in a “idle mode” (i.e. not delivering a stimulatory pulse), some power would continue to be needed for maintaining the remaining functions. Power reduction through intermittent transmission is analogous to the method implemented by Bluetooth Low Energy (BLE), in which cyclic intervals of “activity” and “sleep”

allow for power consumption primarily in the “active” periods. In our pacing system, “sleep” intervals have zero power consumption and “active” intervals consume power exactly equivalent to that necessary to stimulate cardiac tissue without additional losses from a logic circuitry. The transmitting circuitry will, accordingly, become active only when the switch allows passage of current into the system, thus, significantly reducing power losses in the non-ideal inductive power transmission circuit. The fourth advantage is the consequential reduction in tissue absorption as a result of decreased time of transmission. This reduction allows for increased amplitude for each short duration pulse to increase power transfer while remaining below SAR safety limits.

2.2. THREE-TIERED PACEMAKER DESIGN

As a reminder, our goal was to design a pacemaker with (1) miniaturization of the pacer while (2) maintaining sufficient wireless power transmission from the power source to the geometrically constrained pacer. Our remote-controlled intermittent transmission stimulation architecture was able to achieve our first goal; however, extensive variations in patient anatomy (e.g. large BMI) would necessitate further increase in wireless power transfer range.

To address the limitations of inductive power transfer, we established a three-tiered system design consisting of two independently functioning two-coil systems (**Figure 11**). We defined these two systems as the “Stimulation Sub-System” (SSS) and “Charging Sub-System” (CSS). Each sub-system functioned under two distinct operating frequencies to avoid system-to-system interference and inter-dependence.

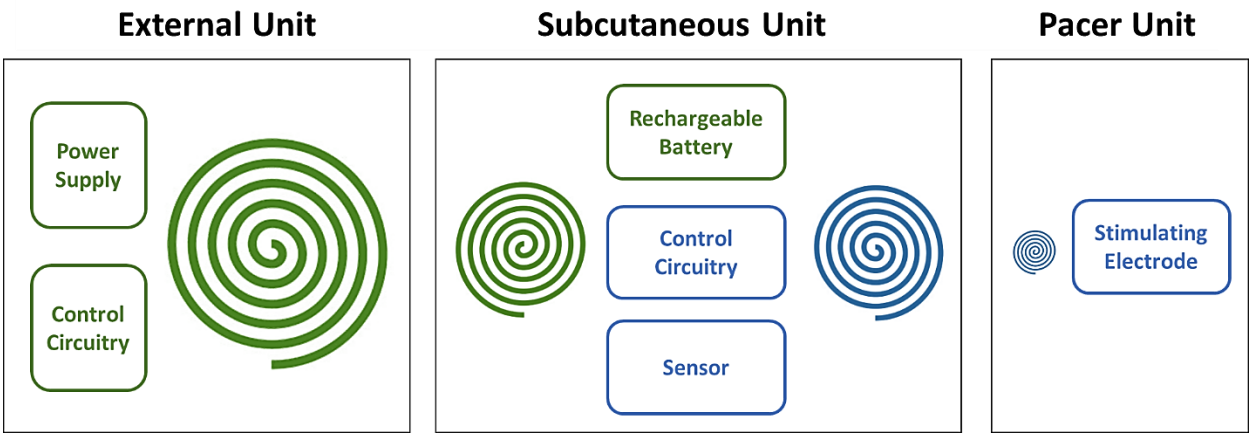

Figure 11: 3-Tiered, 4-Coil, 2-Sub-system Architecture. Each unit is shown in individual boxes with the external unit being the primary power source, the subcutaneous unit being the intermediary component to store and release power to the pacer unit for intermittent short-pulse stimulation. In this figure, the Charging Sub-System (CSS) is illustrated in green and Stimulation Sub-System (SSS) is illustrated in blue.

The three tiers of the complete pacemaker system consisted of (1) an "External Unit" to encase the transmitter coil and control circuitry of the CSS, (2) a "Subcutaneous Unit" to encase the receiver coil of the CSS, a charging circuitry, a rechargeable battery, sensors, the control circuity of the SSS, and the transmitter coil of the SSS, and (3) a "Pacer Unit" to encase the receiver coil of the SSS, a rectifier and regulator, and stimulation electrodes (**Figure 12**).

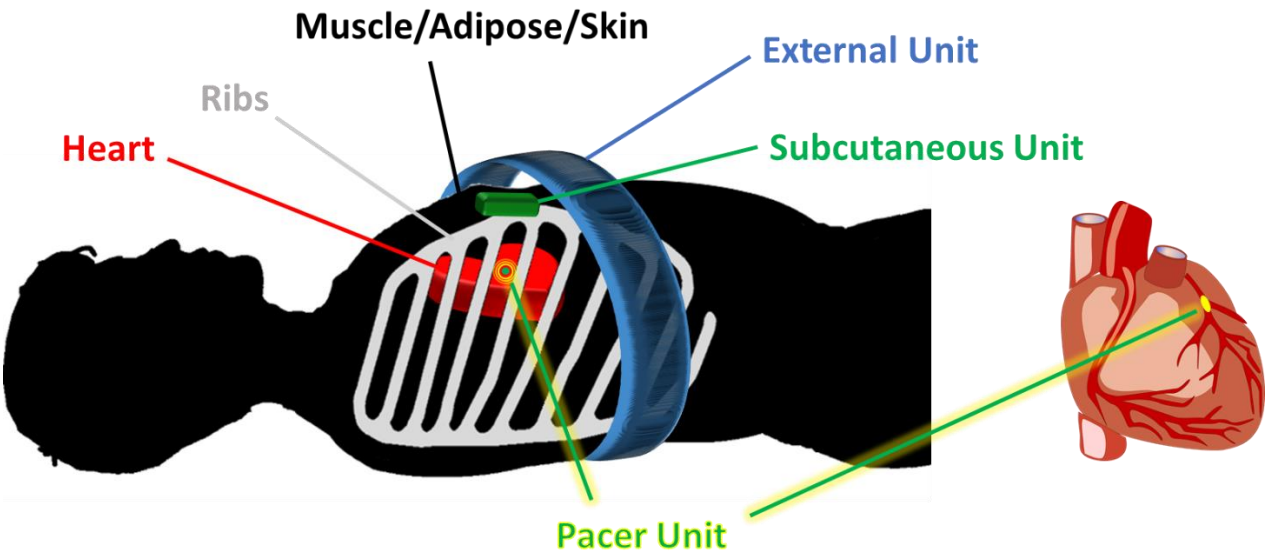

Figure 12: System Implant Structure. The relation of the external unit, subcutaneous unit, and pacer unit is illustrated in the presence of skin/adipose, tissue/muscle, ribs, and the heart. The external unit is placed above the surface of the skin. The subcutaneous unit is placed underneath the skin and above the sternum and ribs. The pacer unit is placed in contact with the heart in a coronary vessel via a similar fixation mechanism as a stent.

The proposed architecture entailed the utilization of intermittent wireless power transfer to independently meet the demands of each sub-system (**Figure 13**). We began with the simulation unit, the first of the implanted components in the SSS. In the case of a cardiac pacemaker, the device was designed for catheter-based intravascular deployment to the anterior cardiac vein (ACV). This design required a millimeter-sized receiver coil, thus resulting in an inherently inefficient inductive power transfer system. We overcame this limitation by taking advantage of a remote-controlled stimulation architecture as previously described in **Section 2.1. Remote-Controlled Stimulation** [55]. As such, for a heart rate of 60 beats per minute (BPM), power would be wirelessly and intermittently transmitted from the second implanted component, the subcutaneous unit, at a pulse frequency of 1 Hz for a pulse duration of 0.2 ms to 1 ms. This

architecture is essential for reducing power consumption, specific absorption rate (SAR), and receiver size. These conditions are optimal for the SSS, in which its simulation unit has significantly limited space available within the anatomical constraints of the ACV. A rechargeable battery was placed in the subcutaneous unit to meet the power demands of the SSS. This battery would be charged as a consequence of the CSS. The receiver of this sub-system was encased in the implanted subcutaneous unit, while the transmitter was encased in the external unit. This external unit would only to be worn during infrequent charging sessions. This frequency and the charging duration would be dependent on the SSS power consumption, battery capacity, and efficiency of the CSS wireless transfer system.

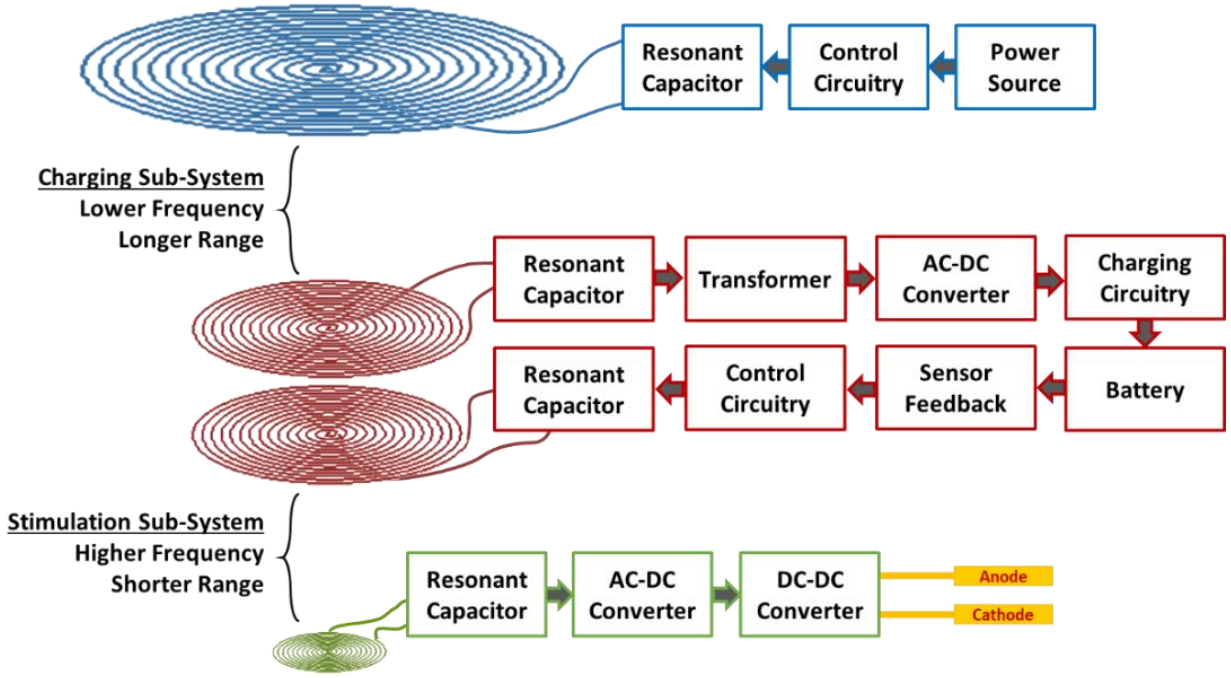

Figure 13: Block diagram of CSS and SSS system design. Each sub-system utilizes intermittent remote-controlled inductive power transfer at a different frequency, resulting in the stimulation of cardiac tissue over a long range.

This three-tiered, two-sub-system design ultimately entail several advantages that optimize its application in biomedical implantable devices. The ability to use different frequencies decouples the power transmission between the two sub-system and allows for adaption to the environmental constraints encountered by each sub-system, including space availability, transmission range, and transmission frequency. In the case of the SSS, the pacer unit faces extreme anatomical constraints in the anterior cardiac vein, whereas the subcutaneous unit has more freedom underneath the skin within the anterior chest wall. In the case of the CSS, the external unit has maximum freedom in size but must also transmit power over a longer range in the setting of variations in the thickness of the chest wall and manual positioning of the chest strap by the patient. Flexibility in frequency selection is also important for meeting SAR demands in each sub-system in which the length and frequency of transmission also varies. The SSS experiences short and frequent transmission, while the CSS experiences long but infrequent transmissions.

In the following sections, we will focus on the design criteria for each of the sub-systems based on these environmental differences and their power recruitments.

3. WIRELESS POWER TRANSFER IN STIMULATION SUB-SYSTEM

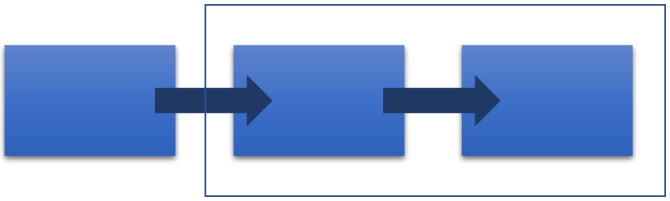

3.1. FEASIBILITY ANALYSIS OF PACER ARCHITECTURE

3.1.1. COIL DESIGN CRITERIA

The power transfer efficiency of an inductive link depends on two primary factors: (1) the quality factor of the transmitting and receiving coils, and (2) the coupling coefficient between the interacting conductors, as shown in Equation (3) [56]:

$$\eta = \frac{k^2 Q_1 Q_{2L}}{1 + k^2 Q_1 Q_{2L}} \cdot \frac{Q_{2L}}{Q_L}, \tag{3}$$

where Q_1 is the quality factor of the transmitter antenna, Q_2 is the quality factor of the receiver antenna, $Q_{2L} = Q_2 Q_L / Q_2 + Q_L$, and $Q_L = R_{Load} / 2\pi f L_2$.

Both variables presented significant design challenges. The quality factor, Q, represents the ability of the resonant circuit to retain energy and is heavily influenced by transmission frequency, f, as shown in Equation (4) [57]:

$$Q = \frac{2\pi f L}{R_{eff}} \tag{4}$$

where f is the operating frequency, L is antenna inductance, and R_{eff} is the effective ohmic losses.

While a higher frequency increases the quality factor, it also leads to an increase in tissue absorption. This presented two key challenges: (1) the device must adhere to guidelines established

by the Federal Communications Committee (FCC) for radio frequency (RF) Specific Absorption Rate (SAR) limits, and (2) increase in tissue absorption leads to decreased power transfer from the transmitter coil to the receiver coil [38].

The coupling coefficient, *k*, is heavily influenced by antenna geometry, as shown in Equation (5) [37]:

$$k = \frac{r_1^2 r_2^2}{\sqrt{r_1 r_2}\left(\sqrt{r_1^2 + D^2}\right)^3} \cos\theta \tag{5}$$

where r_1 is transmitter coil radius, r_2 is receiver coil radius, D is distance between coils, and θ is the misalignment angle.

Coil geometry also impacts the inductance, which in turn influences the quality factor, as shown in Equation (4). However, the dimensions of the device are restricted to the small size capacity of the cardiac implant location. The dimensions of the receiving unit, which will be in contact with the cardiac tissue, must be maintained below a few millimeters to prevent mechanical stresses on the fixation anchor, thus ultimately leading to significant reductions in the coupling coefficient.

Two additional challenges were presented as a result of motion-induced variations between distance and alignment between coils due to cardiac contraction:

(1) Changes in the relative position of the two coils impacts their tuning due to a change in mutual inductance, which is a result of the interaction of one coil's magnetic field on the other. A simple method to account for this variation in inductance without the addition of more complex circuity is through dependence on a larger frequency bandwidth, which can be defined as follows:

$$Q = \frac{f}{B} \tag{6}$$

where Q is the quality factor, f is the operating frequency, and B is the bandwidth.

As a result of this relationship, while a higher Q means increased power transfer efficiency, it also means a lower bandwidth. Thus, the system demands a compromise in design criteria to optimize the effectiveness of wireless power transfer.

(2) Coupling coefficient can be defined by the mutual inductance:

$$M = k\sqrt{L_1 L_2} \tag{7}$$

where M is the mutual inductance, k is the coupling coefficient, L_1 is the transmitter coil inductance, and L_2 is the receiver coil inductance.

As the coupling coefficient increases, so does the mutual inductance. However, the mutual inductance affects tuning of the circuitry. Therefore, here, we are inclined to make a second compromise for optimal design.

With these concepts in mind, our coil design was then guided by two physical constraints: (1) geometric constraints for the implants, and (2) requirements for the range of power transfer. The coils were developed as planar spiral coils to maintain flexibility and to minimize size along the z-direction (i.e. device thickness). The boundary condition for the overall inductor size was preset based on implant position, thus allowing variability only in the inductance and effective resistance according to Equations (4) & (5).

The coil inductances were impacted by the number of turns, wire radius, and wire spacing within the coil's geometric boundaries as determined by using the Modified Wheeler formula by

Mohan *et al* [58]. The AC resistance of the coil was impacted similarly by these factors, as shown in Equation (8) [57]:

$$R_{AC} = \frac{l}{2\pi a \sigma \delta} \tag{8}$$

where l is wire length, a is wire radius, σ is wire conductivity, and δ is skin depth defined by Equation (9) [57]:

$$\delta = \frac{1}{\sqrt{\pi f \mu_o \mu_r \sigma}} \tag{9}$$

where μ_o is the permeability of air, and μ_r is the permeability of copper.

While inductance must be maximized to improve Q, the impacting variables negatively influence coil resistance as shown in Equations (8) and (9): (1) an increase in the number of turns increases wire length, leading to $\uparrow l$ and $\uparrow R_{AC}$, (2) a decrease in wire radius reduces surface area of conduction, resulting in $\downarrow a$ and $\uparrow R_{AC}$, (3) an increase in frequency decreases skin depth of conduction, leading to $\uparrow f$, $\downarrow \delta$, and $\uparrow R_{AC}$. Furthermore, a reduction in the wire-to-wire spacing increases eddy current dampening and wire resistance. Thus, these parameters dictated the variations in coil designs [57].

3.1.2. Receiver Coil Design

The stimulation unit of the SSS was the final recipient of power in our multi-level system and encountered the most stringent constraints. Analogous to the deployment of an intravascular stent, the device was designed to be fixated in the anterior cardiac vein (**Figure 14**), thus limiting the device size to the vessel diameter of 3.8 ± 0.7 mm [59]. This location was selected to provide the

optimal combination of minimizing distance to the transmitter, while maximizing the space for a larger implant and maintaining ease-of-access for catheter-based deployment.

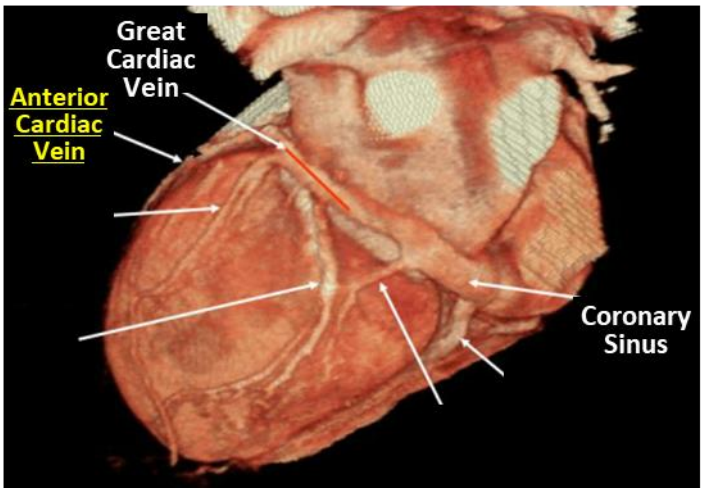

Figure 14: Coronary Veins. The anterior cardiac vein is shown to be a branch of the great cardiac vein, which is a branch of the coronary sinus. This access point provides for a catheter-based delivery mechanism to the implant position [59].

Three different coil designs were investigated with 4 turns of a 30 AWG wire: (1) a coil with a circular geometry and no spacing between each turn **(Figure 15B**), (2) a coil with an elliptical geometry with no spacing between coils in the x-direction and over 2 mm of spacing between coils in the y-direction (**Figure 15C**), and (3) a coil with a circular geometry and spacing between coils equal to that of the wire diameter that forms into a half-cylindrical shape via a gradual fold in the z-direction along the y-axis of the coil; this configuration was further supplemented by a meandering trace with three turns of the coil (**Figure 15D**). The wrapped modification into a half-cylinder achieved a smaller size in the x-direction, while maintaining distance between the turns of the coil along the diagonal direction to minimize proximity effects and capacitive coupling. Furthermore, the addition of the meandering structure to the spiral-shaped antenna can improve power transfer efficiency over a greater range despite misalignment. The

meander allowed for the placement of a condensed linear antenna structure with an alternative field capture in a small space to enhance power absorption. Thus, the coil provided sufficient power transfer in the setting of dynamic cardiac contractions, which create variations in the transmitter-to-receiver transmission angle [60].

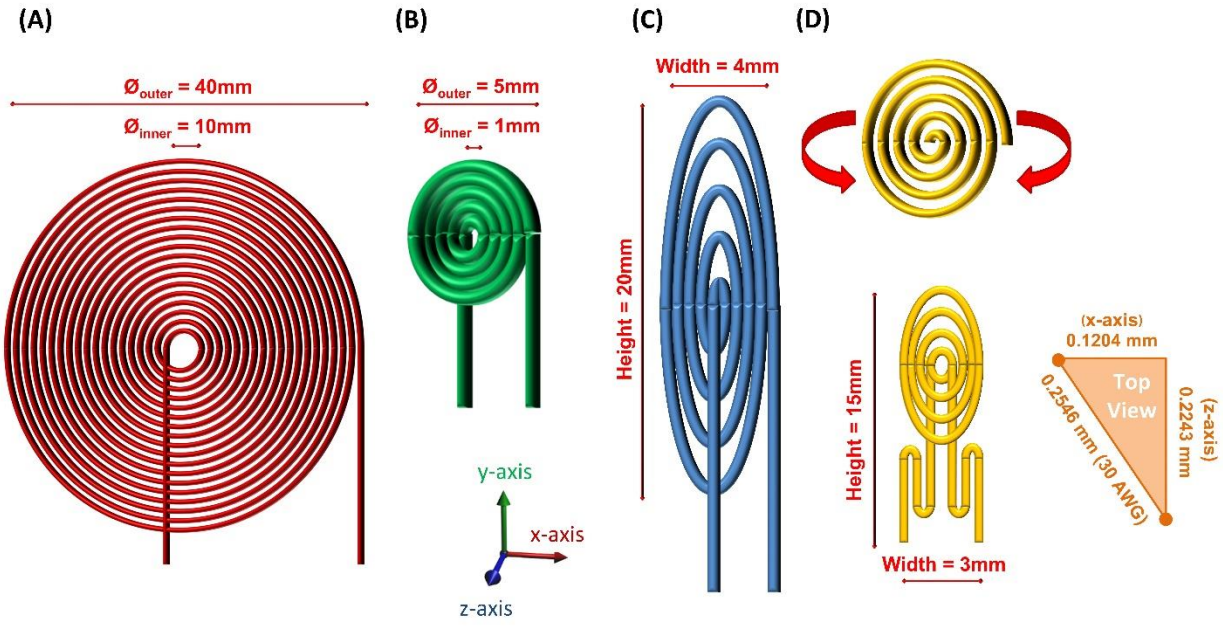

Figure 15: Transmitter and Receiver Antenna Design. (A) The transmitter coil was designed as a planar spiral coil with a 10 mm inner diameter, 40 mm outer diameter, 23 AWG wire, and 18 turns of the coil. (B) Receiver coil designed with 4 turns of 30 AWG wire with a circular geometry and no spacing between each turn resulting in a 5 mm outer diameter. (C) Receiver coil designed with 4 turns of 30 AWG wire with elliptical geometry without spacing between coils in the x-direction, resulting in a width of 4 mm, and over 2 mm of spacing between the coils in the y-direction, leading to a height of 20 mm, and (D) Receiver coil designed with 4 circular turns and 3 meandering turns of a 30 AWG wire. The upper figure highlights a coil with a circular geometry and spacing between coils equal to that of the wire diameter. This configuration wraps into the z-direction along the y-axis of the coil and forms into a half-cylindrical shape. This design was further supplemented by a meandering structure, resulting in a final antenna shape shown at the bottom-left with width of 3

mm, height of 15 mm, and depth of 2 mm. The lower right diagram demonstrates > 50% space reduction along the x-direction through the transfer of coil spacing into the diagonal.

3.1.3. TRANSMITTER COIL DESIGN

The transmitter coil of the subcutaneous unit had more flexibility in size and shape due to more available space in the anterior chest wall. To minimize aesthetic side-effects, the transmitter was designed as a planar coil with a diameter of 40 mm, with a 23 AWG copper wire, spaced apart by a distance equal to that of the wire diameter with 18 turns of the coil (**Figure 15A**).

3.1.4. CIRCUIT DESIGN

The system was designed using a carrier frequency of 13.56 MHz based on frequency band assignments for medical devices and tissue absorption criteria in consideration with power transfer efficiency goals [61]–[63]. The resonant capacitor, C_{res}, for each corresponding inductor was computed using Equation (10) [57]:

$$C_{res} = \frac{1}{L(2\pi f)^2} \tag{10}$$

where L is the inductance and f is the carrier frequency.

Power transfer for an inductive link is maximized when LC tank circuits of the transmitter and receiver are both tuned to the same resonant frequency, in this case 13.56 MHz (**Table I**).

Table I: Summary of Theoretical Computations for Transmitter and receiver Coils

Parameter	Transmitter	Circular Receiver	Elliptical Receiver	Cylindrical Receiver
L (nH)	9940	160	225	134
C (pF)	14	890	610	1040

A Class E Power Amplifier (PA) was implemented for the transmitter for its capacity to maintain high efficiency with low DC input current and high AC output current into the tank circuit. The Class E PA was designed based on principles described by Sokal [64]. In the selection of the MOSFET, essential parameters included the low on-resistance ($R_{DS(ON)}$), low output capacitance (C_{oss}), and low gate threshold voltage ($V_{GS(th)}$). We elected to proceed with the BS170 MOSFET (MFG P/N BS170FTA). For the DC input, stimulation rate was controlled via an IC switch (MFG P/N TS12A4514DBVR),

A bridge rectifier and low-dropout regulator were employed in the receiver circuity following the tank circuit. The rectifier was implemented using Schottky diodes (MFG P/N SMSA3923-011LF) to minimize power drop across the diode. A resistor was used to simulate the load impedance experienced at the electrode-tissue interface.

3.1.5. Coil Displacement Measurements

The range for power transmission was assessed via thoracic Magnetic Resonance Images (MRI) to determine the anatomic displacement between the transmitting and receiving units. All imaging studies were approved by the UCLA Institutional Review Boards (IRBs) and informed consent was obtained from participants. Measurements were made at six equidistant points along the red box highlighted in **Figure 16** and the average value was used to estimate the displacement between the right ventricular (RV) free wall, near the septal wall and the RV apex, and the anterior chest wall, below the adipose tissue, at the sternal border. Adipose tissue anterior to the sternum poses the greatest source of variation in the distance between the transmitter and receiver. For this reason, in bypassing the fat layer, we were able to better predict the interaction between the transmitter-receiver pair and improve power transfer efficiency.

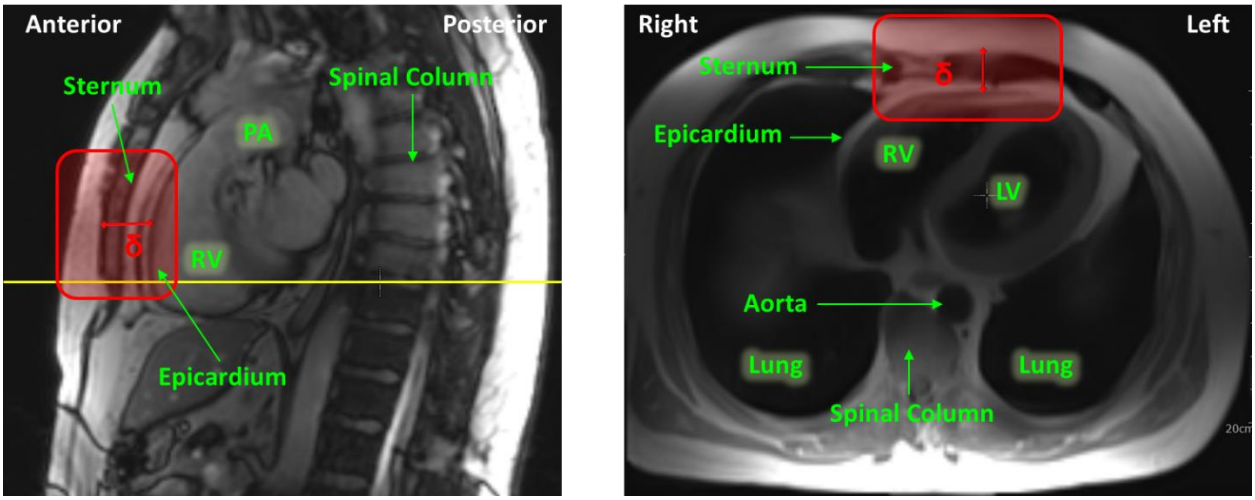

Figure 16: Determining Range of Function. Thoracic MR images in which the left image shows the sagittal view with the yellow line representing the cross-reference line for the axial black blood image in right image. The red box represents the region in which measurements were made in both views. The distance, δ, represents the displacement measured along the region of the red box in which the receiver will be located in the anterior cardiac vein and the transmitter will be located in the anterior chest wall below the adipose tissue along the sternal border. PA: pulmonary artery, RV: right ventricle, LA: left ventricle.

MRI displacement measurements revealed an estimated transmitter-to-receiver distance of 2.0 ± 0.85 cm, which established the testing criteria.

3.1.6. Comparison of Power Transfer Efficiency Over Distance

3.1.6.1 Simulation Studies

Three receiver coil geometries were modeled in Solidworks computer-aided design software. The models were imported into ANSYS Maxwell Finite Element Analysis software (**Figure 17**). The transmitter of **Figure 15A** was positioned at varying distances apart from the receiver coil. Based on the estimated range of anatomical displacement between the transmitter and receiver implant

position from MRI measurements, inductive power transfer from the transmitter to each of the three receivers was examined from a range of 1.0 cm to 3.0 cm.

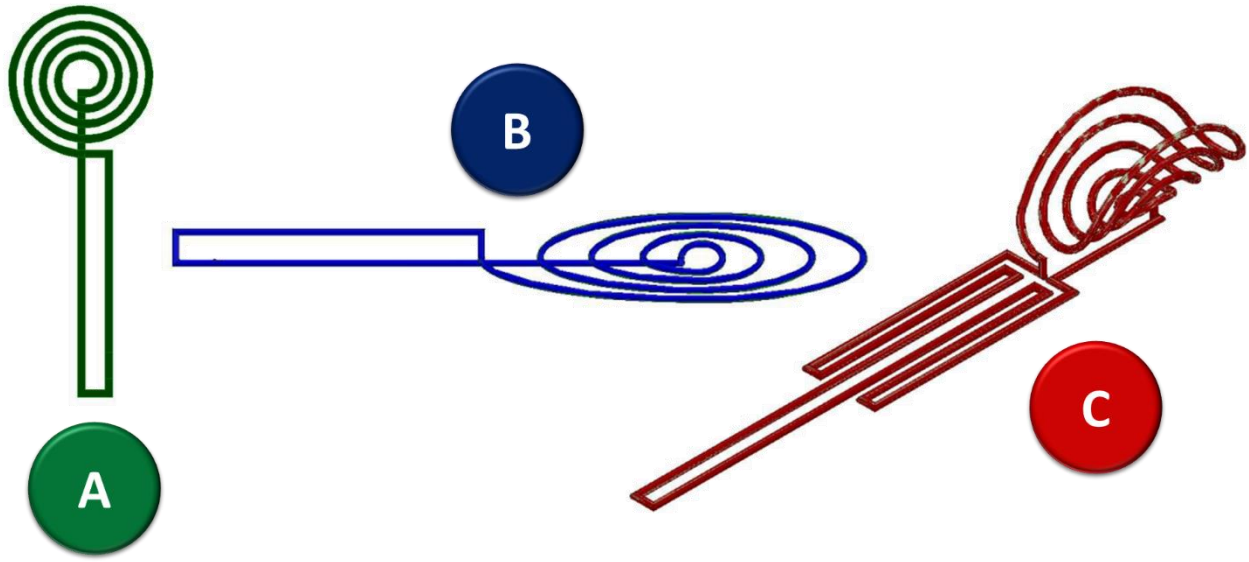

Figure 17: Potential Receiver Coil Designs Modeled in Solidworks & ANSYS. (A) 4 turns of 30 AWG wire with a circular geometry, resulting in 5 mm outer diameter. (B) 4 turns of 30 AWG wire with elliptical geometry, resulting in 4 mm width and 20 mm height. (C) 4 circular turns folded into a half-cylinder and 3 meandering turns of a 30 AWG wire, resulting in width of 3 mm, height of 15 mm, and depth of 2 mm.

Using the Eddy Current solver in ANSYS Maxwell, we simulated the magnetic (B) field, inductance, resistance, and coupling coefficient resulting from the 13.56 MHz alternating current (AC) in the transmitting coil and its impact on the receiving coil. The simulation profile was established with Current Excitation in the transmitter and receiver with a 90-degree phase shift in the receiver AC current. The meshing was set up as follows:

1. To increase accuracy of the numerical model, a denser mesh was necessary near the surface of the coil. This modification was essential since the majority of current would be flowing near the coil surface as a result of the skin effect. To achieve this increased mesh

density near the surface without increasing density throughout the geometry cross-sectional area, two skin layers were generated. Each skin layer maintained the same shape as the target geometry, but with a smaller diameter. The diameter of the skins was determined as shown in Equation **(**11**)** based on the skin depth at the selected frequency as computed by Equation (9):

$$d = D - n\delta \tag{11}$$

where d is the skin diameter, D is the coil diameter, n is the skin layer, δ is skin depth as a result of the skin effect.

2. The mesh for each skin layer was then generated using the Surface Approximation mesh operation.
3. The mesh for the coil geometry was generated using adaptive curved surface meshing and classic mesh method.

An air box geometry of size 500 x 500 x 500 mm with a Radiation boundary was created to surround the transmitter and receiver coils. Convergence was established with a 2 percent error.

The B-field results of the simulation for the half-cylindrical receiver coil with meandering tail can be seen **Figure 18** demonstrating the exponentially waning magnetic field captured by the receiver coil as the distance between the two conductors increased from 1.0 cm to 3.0 cm.

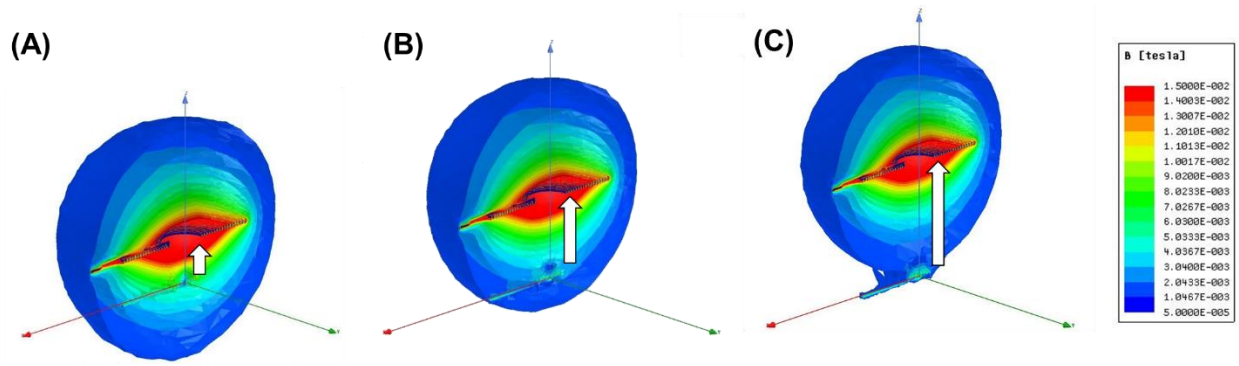

Figure 18: B-Field Simulations. (A) Magnetic field experienced by the receiver coil at 1 cm distance. (B) Magnetic field experienced by the receiver coil at 2 cm distance. (C) Magnetic field experienced by the receiver coil at 3 cm distance. All displayed B-fields are based on half-cylindrical receiver coil with meandering tail.

The coils' internal resistance and inductance as well as the coupling coefficient between the interacting components were computed by the solver and imported into PSPICE Electronic Circuit Optimization & Simulation software. We simulated the circuit of **Figure 9** with a 500-ohm load at the receiver, which is representative of the impedance of a typical standard-impedance pacemaker stimulation lead electrode. We measured the power transfer efficiency based on the voltage across the load in the receiver given an input voltage of 5 V and power of about 250 mW to the transmitter. This instantaneous input power would be equivalent to 250 µW of average power given a 1 ms pulse duration and 60 BPM target heart rate.

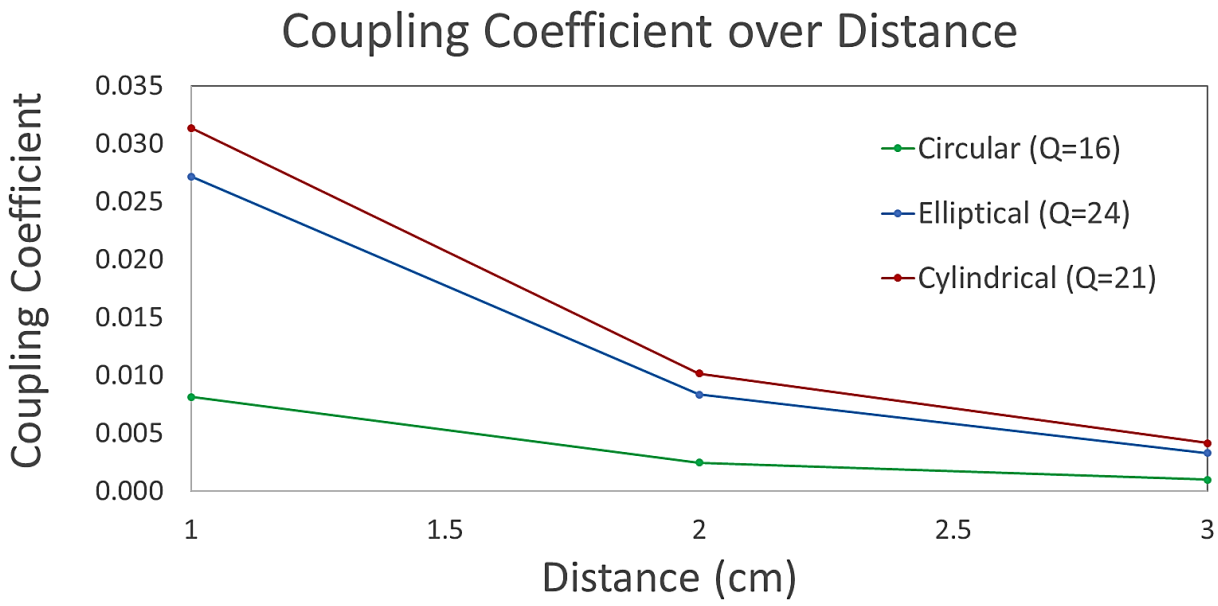

Figure 19: Coupling Coefficient Simulation Results. Coupling coefficient and quality factor computed for each of the three receiver coil geometries through ANSYS Maxwell simulation across 1.0 to 3.0 cm distance between the transmitter and receiver coils. Results indicate higher coupling coefficient for the half-cylindrical geometry with the meandering tail.

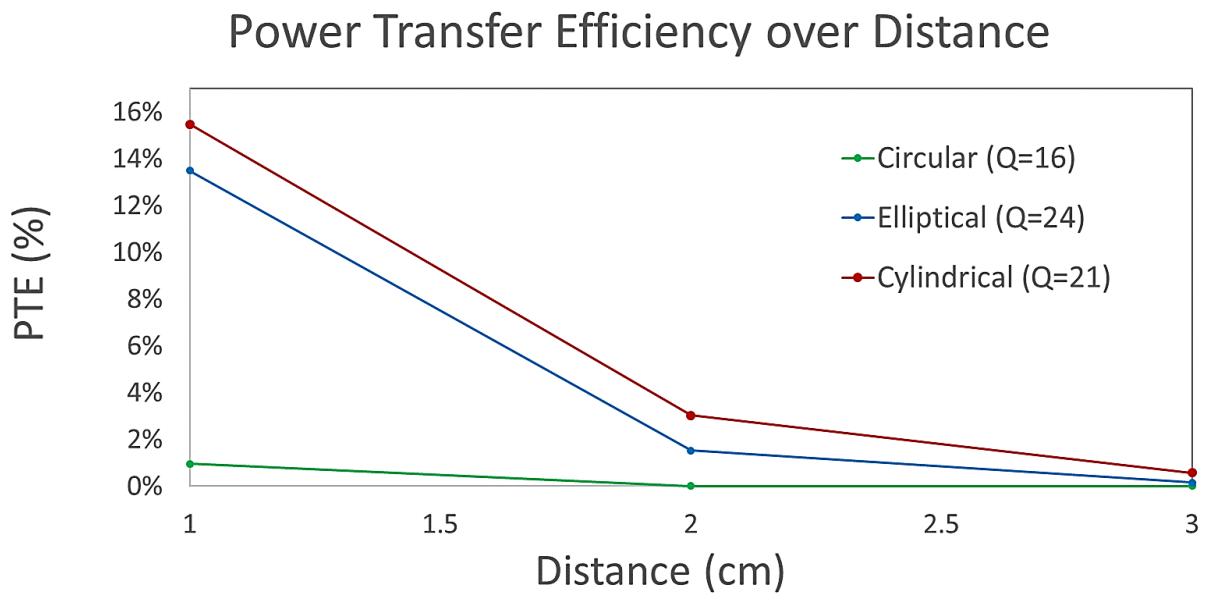

Figure 20: Power Transfer Efficiency Simulation Results. Power transfer efficiency computed in PSPISE software based on coupling coefficient and quality factor computed for each of the three

receiver coil geometries in ANSYS Maxwell simulation. Calculations were made across 1.0 to 3.0 cm distance between the transmitter and receiver coils. Results indicate higher power transfer efficiency for the half-cylindrical geometry with the meandering tail.

Simulation results (**Figure 19** and **Figure 20**) demonstrated the circular coil to have the lowest quality factor, coupling coefficient, and power transfer efficiency. This is expected as the circular coil had the lowest surface area for capture of the magnetic field (impacting *K*) while also experiencing high resistance as a result of the proximity effect (impacting *Q*). The elliptical and cylindrical geometries were closer in outcome due to similar surface area for the capture of the magnetic field. The elliptical coil geometry demonstrated higher quality factor while the cylindrical coil demonstrated higher coupling coefficient. Ultimately, the cylindrical coil was shown to have the highest power transfer efficiency indicating the larger effect of marginal difference in coupling coefficient in comparison to a marginal difference in the quality factor. Furthermore, it is important to note that while the quality factor was higher in the elliptical geometry, it did not necessarily suggest that it would serve as the better receiver coil. This is due to the impact of bandwidth on adaptability in the case of motion-induced changes in displacement and misalignment. While the cylindrical coil had a slightly lower quality factor, it also permitted more leniency in case of these changes.

3.1.6.2. BENCH STUDIES

Upon validation of coil geometries through simulation results, the transmitter and receiver coils were hand-wound and the circuitry was fabricated on a Printed Circuit Board (PCB). The PCB was designed on PCBWeb Designer software on a 2-layer 1.6 mm thickness FR-4 TG130 substrate with 1 oz copper tracings and HASL with lead surface finish. The coils were soldered into the circuit as shown in **Figure 21A**. The output of the receiver was fabricated as an open circuit and

headers were soldered onto the PCB to allow for connection to stimulation electrodes or a representative resistor for bench studies. The power transfer efficiency with each of the three types of receiver coils in **Figure 17A-C** were tested across a range of 20 to 40 mm as shown in **Figure 21B**. Bench tests were performed with a 500 ohm load using a resistor. This value was selected based on estimated impedance in a standard impedance pacemaker lead, taking into account the electrode, tissue-electrode interaction, and tissue in an implanted device.

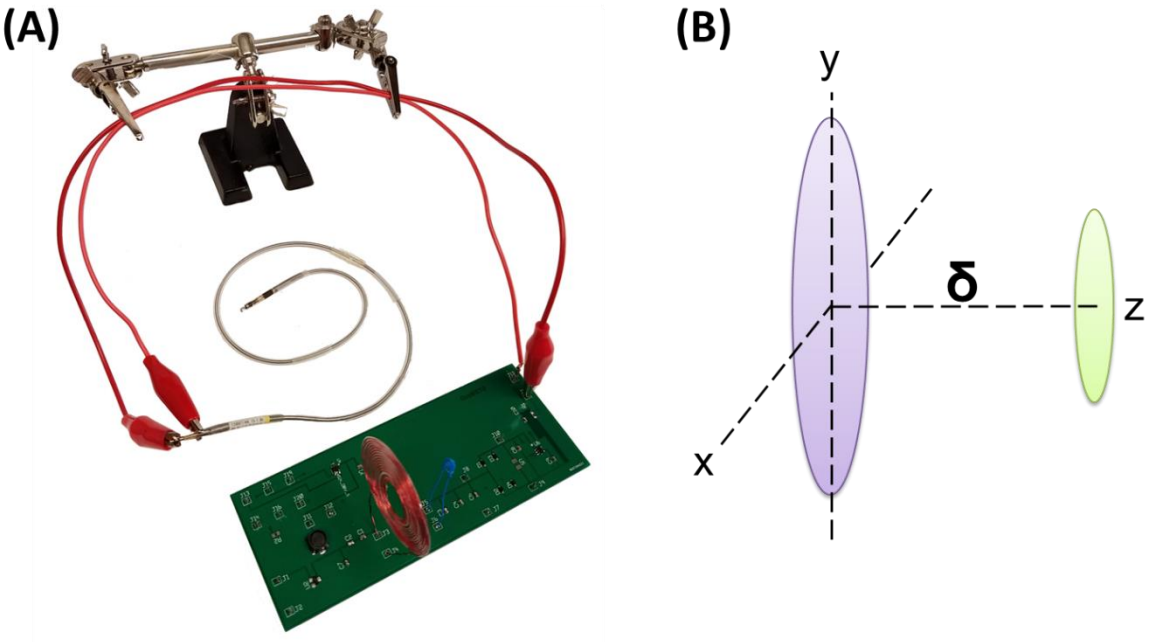

Figure 21: Bench Studies Experimental Setup. (A) PCB with transmitter and receiver circuitry, connected to the transmitter coil (red) and receiver coil (blue) with the output of the receiver system electrically connected to the anode and cathode of an existing bipolar lead; (B) Coil assessment at different distances, δ.

While the power transfer efficiency invariably diminished in response to an increase in distance between the transmitter and receiver coils (**Figure 22**), in all cases, the data indicated that

the wrapped half-cylindrical coil provided the optimal power transfer efficiency. This was in alignment with simulation results in **Section 3.1.6.1 Simulation Studies**.

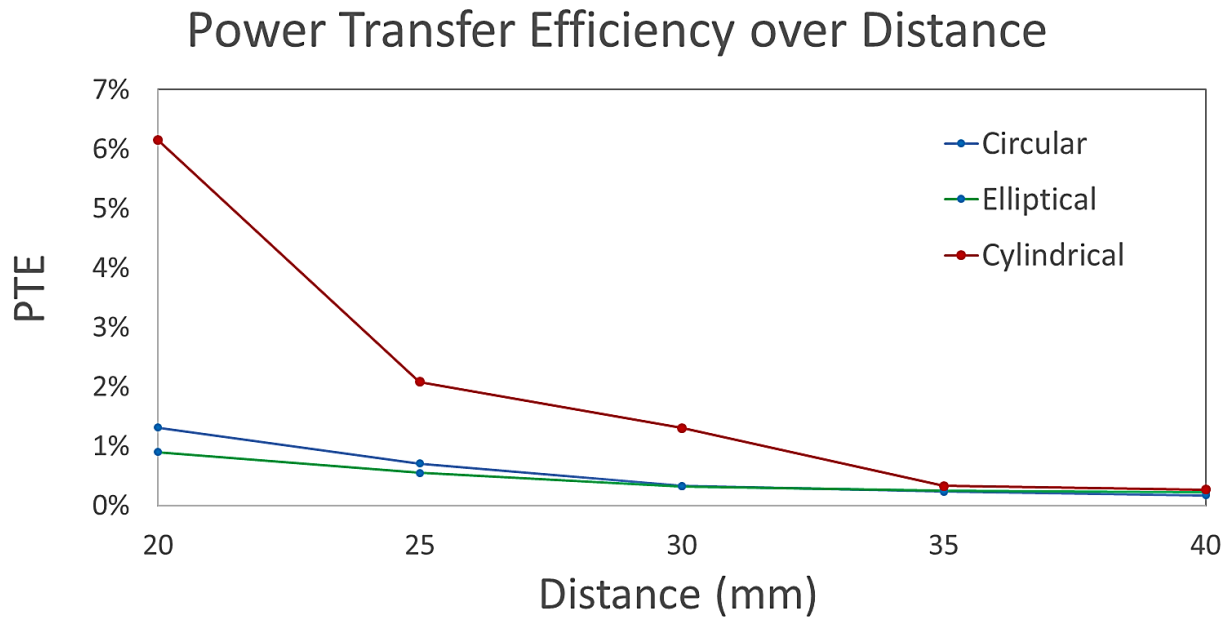

Figure 22: Power Transfer Efficiency over Distance. Assessment of PTE over a distance range of 20 to 40 mm for the three coil geometries demonstrates that the half-cylindrical coil with a meandering tail is the most efficient receiver coil design. Exponentially decreasing power transmission over distance minimizes differentiation between the three coils at longer ranges.

Given a transmitter supply of 5 V at 0.20 A (1 W of instantaneous power), the half-cylindrical receiver antenna was capable of reaching a 2 V voltage amplitude with a 500-ohm load at >30 mm without misalignment. This is over twice the mean pacing threshold of 0.8 V [65] and 10 mm above the mean displacement between the transmitter and receiver as measured and discussed in **Section 3.1.5. Coil Displacement Measurements**.

3.1.7. Comparison of Power Transfer Efficiency Over Angular Misalignments

The power transfer efficiency with each of the three types of receiver coils in **Figure 17A-C** were tested under three additional conditions as shown in **Figure 23A-C**: (1) x-axis angular misalignment between coils up to 45 degrees with a distance of 20 mm apart, (2) y-axis angular misalignment between coils up to 45 degrees with a distance of 20 mm apart, and (3) displacement misalignment between coils up to 45 degrees with a distance of 20 mm apart. Relative coil misalignments were examined at a constant displacement of 20 mm based on the mean displacement between the transmitter and receiver as measured and discussed in **Section 3.1.5. Coil Displacement Measurements**.

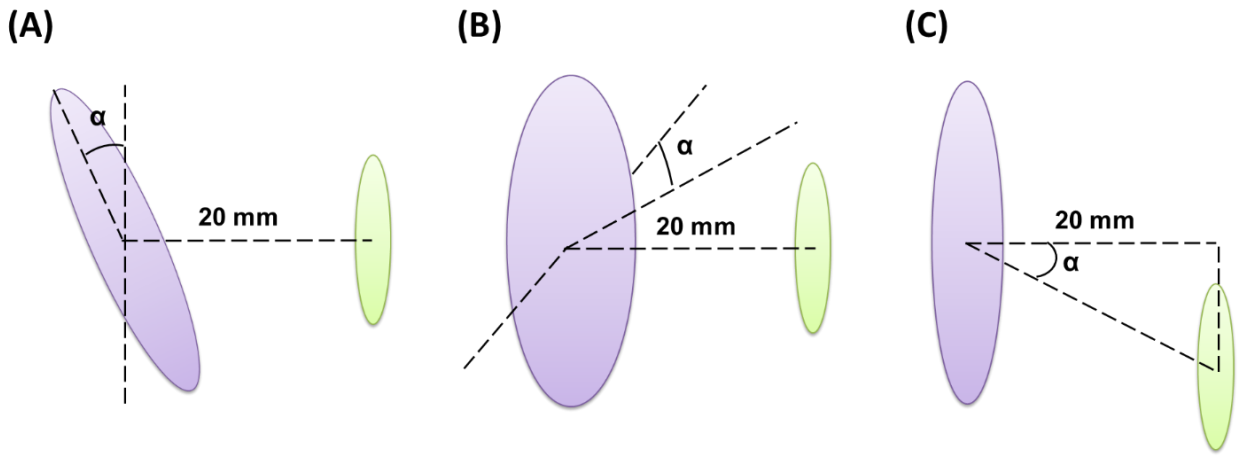

Figure 23: Angular Coil Assessment. (A) Coil assessment with x-axis angular misalignment at angle, α, (B) Coil assessment with y-axis angular misalignment at angle, α, and (C) Coil assessment with displacement misalignment at angle, α.

Bench tests for the assessment of angular misalignment were performed with a 500-ohm load using a resistor. As before, this value was selected based on estimated impedance in a standard impedance pacemaker lead, taking into account the electrode, tissue-electrode interaction, and tissue in an implanted device.

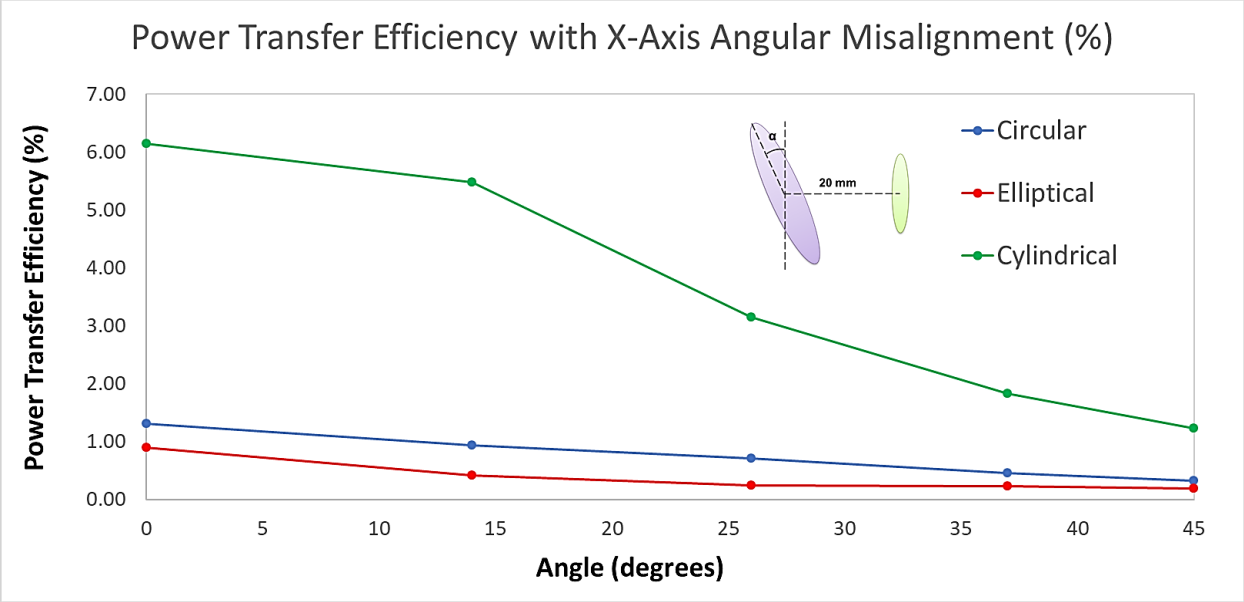

Figure 24: X-axis angular misalignment from 0 to 45 degree. The half-cylindrical coil geometry with the meandering structure provided the optimal power transfer efficiency as compared to the circular and elliptical configurations.

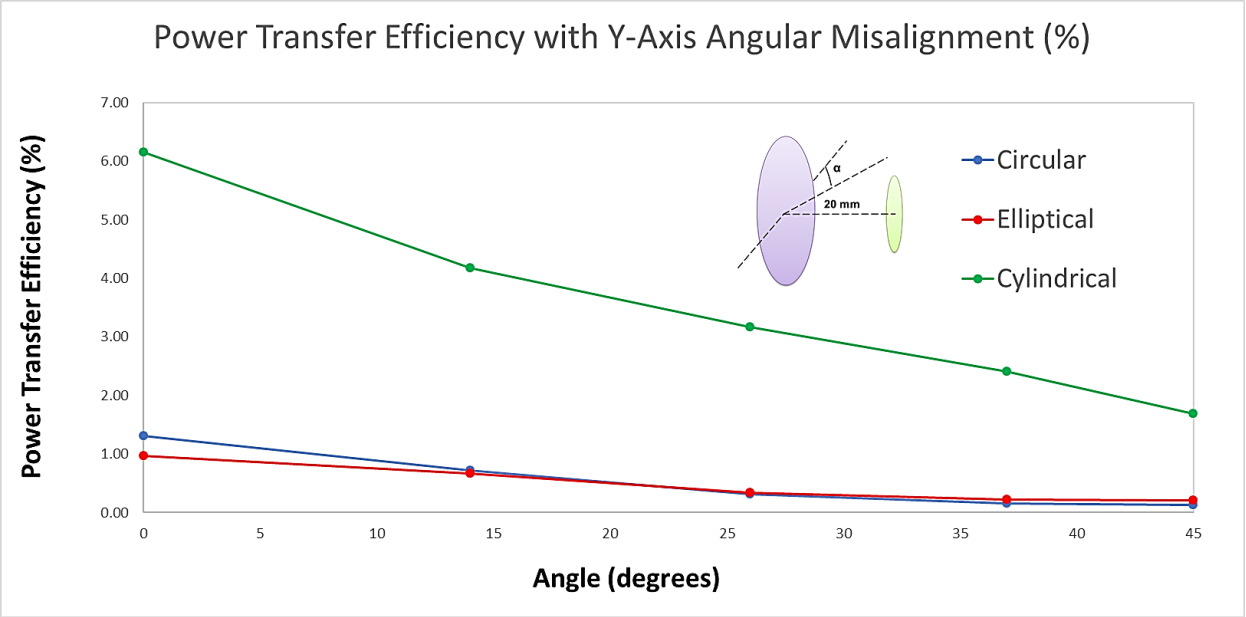

Figure 25: Y-axis angular misalignment from 0 to 45 degree. The half-cylindrical coil geometry with the meandering structure provided the optimal power transfer efficiency as compared to the circular and elliptical configurations.

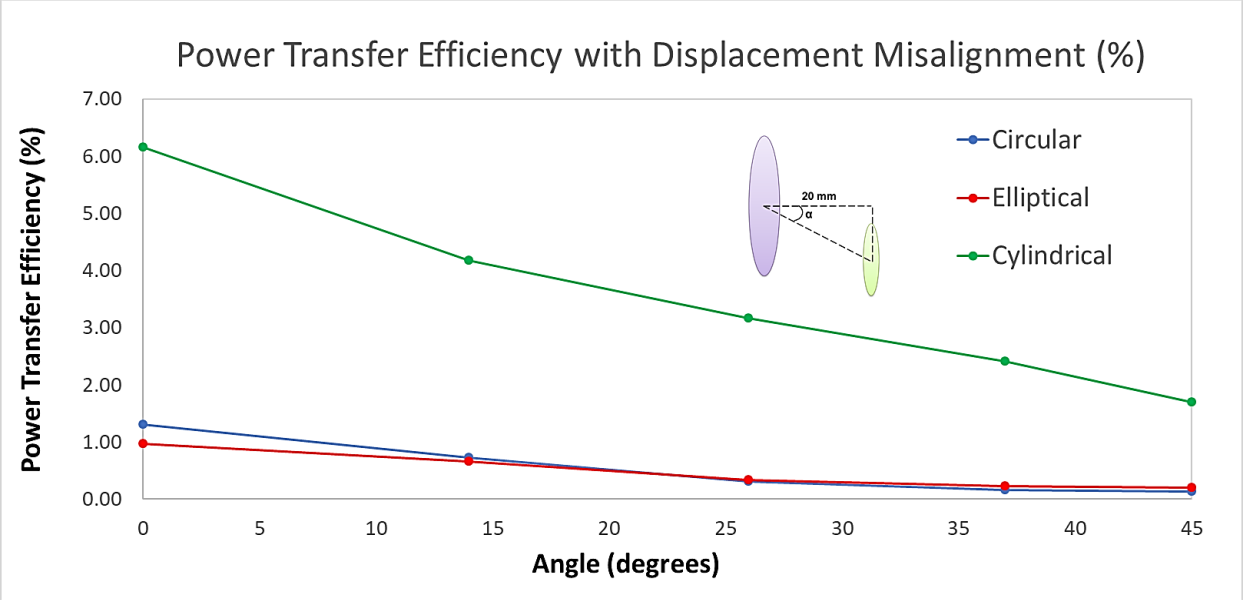

Figure 26: Displacement misalignment from 0 to 45 degrees. The half-cylindrical coil geometry with the meandering structure provided the optimal power transfer efficiency as compared to the circular and elliptical configurations

Given a transmitter supply of 5 V at 0.20 A, the half-cylindrical receiver coil with the meandering tail was capable of reaching a 2 V voltage amplitude with a 500-ohm load at 20 mm with 45^{o} displacement misalignment, 20 mm with 45^{o} x-axis angular misalignment, or 20 mm with 45^{o} y-axis angular misalignment. The ability to maintain output power at over twice the mean pacing threshold of 0.8 V [65] over misalignments that mimiced cardiac motion-induced changes in transmitter and receiver relative positions revealed a necessary capability for the function of a cardiac stimulation device.

Furthermore, in both distance and misalignment studies, despite continuous wireless transmission requiring 1 W of power, intermittent power transmission at 1 Hz and 1 ms pulse width engendered a power reduction to 1 mW. Also notable is that testing was performed with a 1 ms

pulse width, as opposed to the commonly performed pulse width of < 0.5 ms, which would further reduce the power requirement.

3.1.8. EX VIVO EVALUATION OF PACEMAKER FUNCTIONALITY IN PORCINE MODEL

A postmortem study was performed to demonstrate the feasibility of our pacing system in a male Yucatan miniature pig (S & S Farms, Ranchita, Calif). All animal studies were approved by the UCLA Office of Animal Research in compliance with the UCLA IACUC protocols. A thoracotomy was performed to expose the epicardium for external pacing by an experienced veterinarian from the UCLA Department of Animal and Laboratory Medicine. The transmitter and receiver coils were aligned and spaced at 20 mm apart. The output of the system was connected to electrodes of an existing standard impedance bipolar lead (**Figure 21A**), the St. Jude Tendril SDX Model 1388T with previously reported short-term ventricular lead impedance of 553±106 ohms [66]. The lead was fixated into the epicardium of the pig heart near the anterior cardiac vein at the RV apex. The distal electrode, acting as the cathode, was electrically connected to the fixated helix; the proximal electrode, acting as the anode, was sutured in place (**Figure 27A**).

External pacing was initiated immediately post-euthanasia to minimize cellular apoptosis and release of intracellular electrolytes (Na^+, K^+, Ca^{2+}). A pacing amplitude of 2 V, pulse width of 1 ms, and heart rate of 60 BPM were delivered via the bipolar lead electrodes. Simultaneous Electrocardiogram (ECG) recordings allowed for monitoring cardiac rhythm and assessing pacemaker effectiveness (**Figure 27B**).

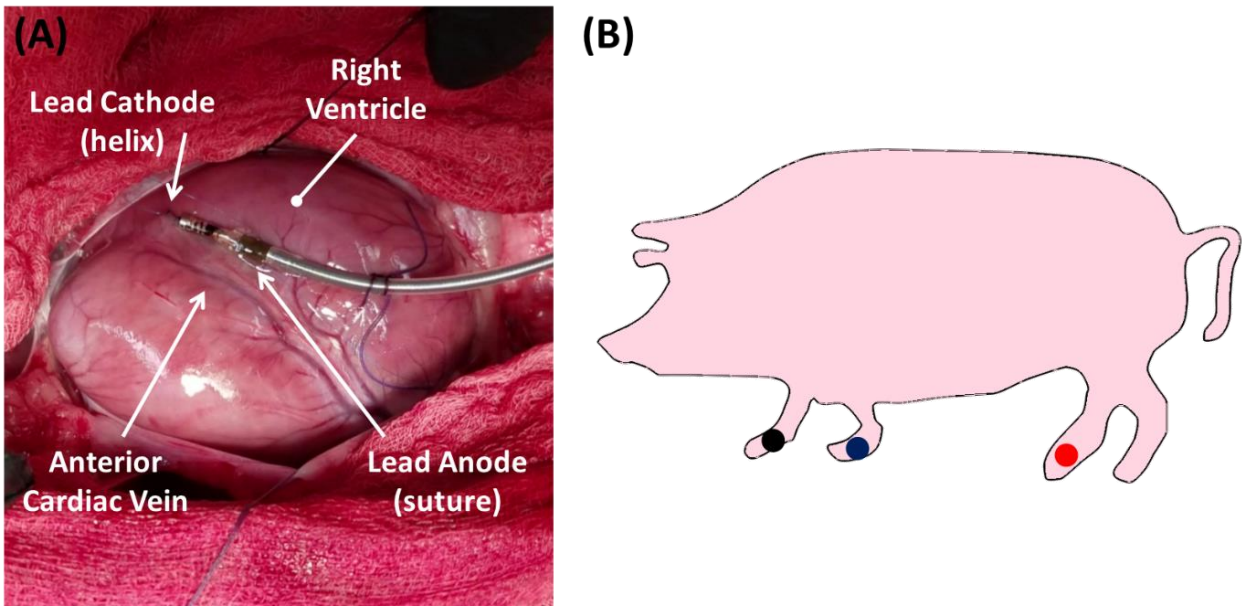

Figure 27: Porcine Studies Experimental Setup. (A) Implant location of the bipolar lead on the porcine heart with the cathode at the distal tip fixated via helix into the epicardial wall and the anode proximal to the cathode in the form of a ring fixated via sutures; (B) ECG lead placement shown via the blue, red, and black dots.

Based on bench test data of transfer efficiency, the wrapped half-cylindrical receiver coil with the meandering structure (**Figure 17C**) was determined as the optimal design for the *ex vivo* investigation of the pacemaker. To determine the efficacy of paced cardiac rhythms, we assessed the surface ECG readings pre-euthanasia, post-euthanasia, and during experimental pacing. Prior to euthanasia, the ECG exhibited a typical P wave for atrial contraction, QRS for ventricular depolarization, and T wave for ventricular repolarization (**Figure 28A**). Post-euthanasia, epicardial stimulation generated a wide-complex paced rhythm as anticipated for ventricular pacing (**Figure 28B-C**). During the pacing period, we were able to restore mean arterial blood pressure (MAP) from 0 to 37 mmHg. Thus, our *ex vivo* pacing via the wrapped half-cylindrical coil with a

meandering tail in combination with a remote stimulation control provided sufficient power to energize a postmortem porcine heart.

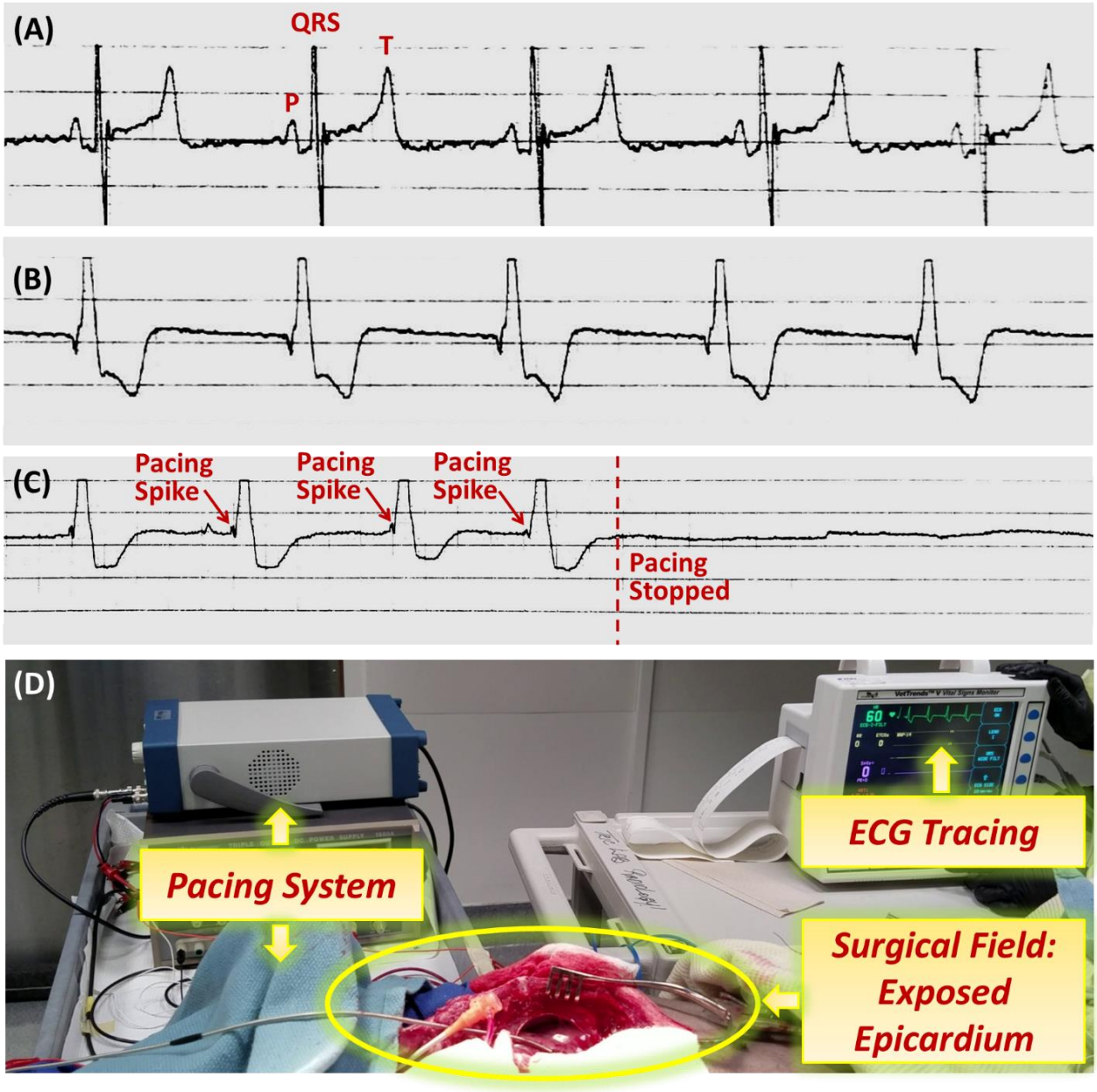

Figure 28: Porcine Studies Experimental Setup and Results. (A) Prior to euthanasia of the animal, ECG recordings revealed a heart rate of 77 BPM, MAP of 90 mmHg, and normal P, QRS, and T waves that indicate normal sinus rhythm. (B) After euthanasia and during the pacing period, ECG recordings revealed a heart rate of 60 BPM and MAP of 37 mmHg. The wide-complex paced rhythm

indicates successful pacing via the remote-controlled wireless pacing system. (C) Zoomed-in view of the ECG tracing highlights the pacing spikes that appropriately stimulates ventricular contraction. When pacing was deactivated, electrical activity was absent as indicated by a flat line on the ECG, thus supporting the pacer-dependency of the post-mortem animal's heart and effectiveness of the remote-controlled pacemaker's ability to stimulate appropriate electrical activity in the mammalian heart. (D) Wide-angle image highlights the setup for post-euthanasia pacing of a pig heart accompanied by simultaneous ECG recording.

3.2. MICRO-PACER TRANSLATION TO PRACTICE

3.2.1. INTRAVASCULAR PACER DESIGN AND FABRICATION

Successful preliminary studies for the designation of the receiver and transmitter coil geometry were followed by fabrication of the microscale pacer system in its intended form-factor for intravascular deployment and implantation.

The transmitter (Tx) coil geometry was maintained as previously demonstrated. The diameter of 40 mm was guided by current pacemaker pulse generator size and the planar design was guided by the desire to reduce the aesthetic impact on the patient by using minimal thickness (0.57 mm); the transmitter circuitry was, however, enlarged by 15-fold to facilitate experimental handling (**Figure 30A**). The complete transmitter system was embedded in polydimethylsiloxane (PDMS) for insulation against water.

The receiver (Rx) coil geometry was slightly modified in order to allow for packaging into a 3 mm diameter hollow tubing. The primary design as a half-cylindrical coil with a meandering tail was maintained as a means to optimize power transfer efficiency in a highly constrained position that experiences changes in alignment with respect to the transmitter. The changes in geometry were as follows:

1. The number of turns in the circular portion of the coil was increased from 4 turns to 5 turns.
2. The length of the turns with respect to the length of the meandering tail was increased. Specifically, in the original design, the 15 mm length of the full coil consisted of 8 mm from the circular turns and 7 mm from the meandering tail. In the second-generation device, the 15 mm length of the full coil consisted of 10 mm from the circular turns and 5 mm from the meandering tail.
3. Magnet wire was utilized instead of polytetrafluoroethylene wire. Magnet wire has a very thin layer of insulation, such that the turns of the coil were separated by air and epoxy instead of the insulation material.

The PCB was designed on PCBWeb Designer software and printed on a 2-layer 0.13 mm thickness flexible polyimide substrate with 1 oz copper tracings and immersion gold surface finish (**Figure 29**). The components were soldered onto the PCB and the electrodes were surface treated with a layer of platinum for optimal contact impedance with the tissue.

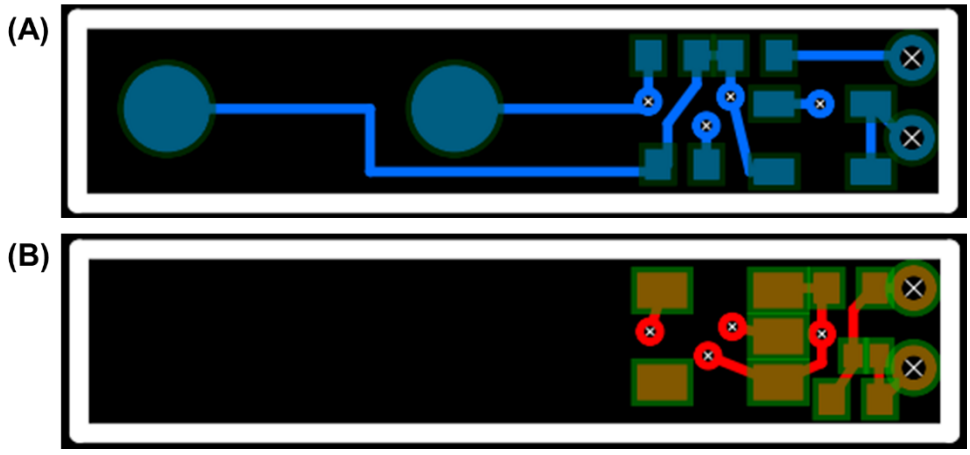

Figure 29: PCB Design. (A) Top layer of the PCB with five components and two circular electrodes. (B) Bottom layer of the PCB with four components.

The receiver coil was soldered onto 0.35 mm through-holes on the edge of the flexible PCB. The combined coil and circuitry were lubricated with oil and inserted into a 9 Fr catheter (3 mm diameter) consisting of natural polyetheretherketone 381G material (inner diameter of 0.118 inch, outer diameter of 0.128 inch). The surface of the electrical components was covered with PDMS for insulative encapsulation against water. The final packaging was a hollow cylindrical configuration as shown in **Figure 30B**. The hollow configuration of the internal components allowed for blood flow through the pacer and for fixation analogous to a stent. Finally, the stimulation electrodes were folded to the outside of the PEEK catheter to allow for contact with tissue (**Figure 30C**). The electrodes were connected to the tubing using epoxy.

The two-coil device was thus configured for the designated implant locations for the transmitter and receiver based on the three criteria for: (1) minimal distance between the communicating components, (2) ease of deployment, (3) minimal impact by complications such as stenosis of the selected vessel.

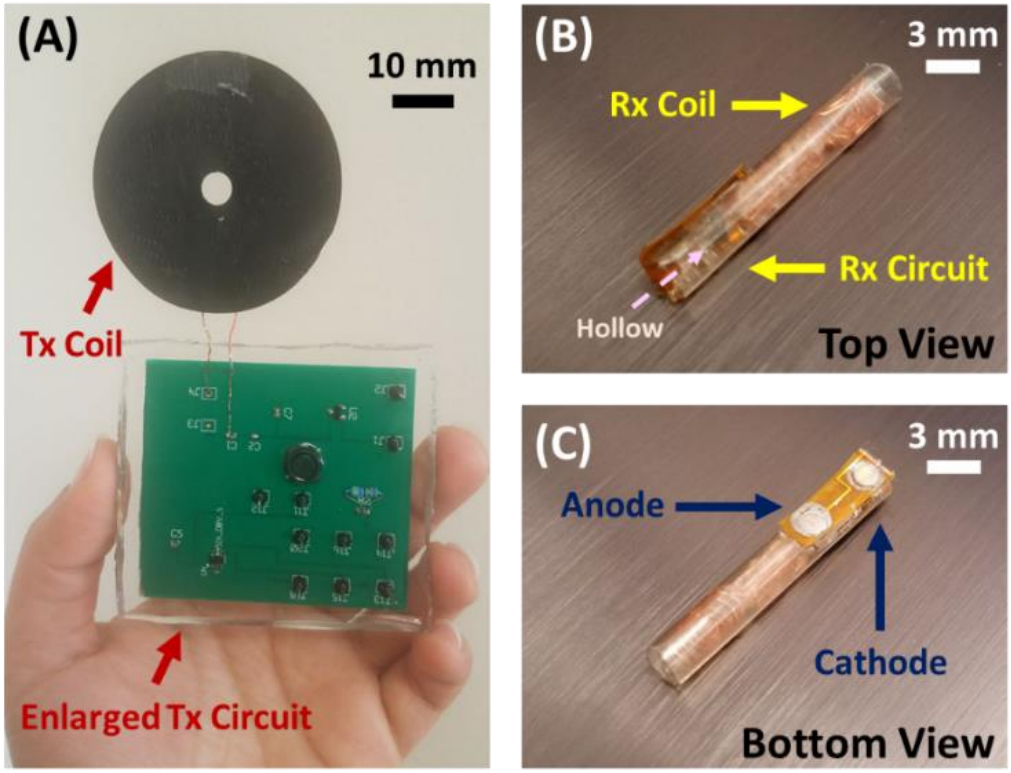

Figure 30: Fabricated Device. (A) The subcutaneous component consists of a planar transmitter (Tx) coil of 40 mm diameter (black enclosure) that is connected to the transmitter circuitry with black headers to allow for connection to the power supply. (B) The pacer component consists of a cylindrical receiver coil measured at 3 x 3 x 15 mm that is connected to the receiver (Rx) circuitry. (C) The pacer stimulation electrodes are electrically connected to the receiver circuitry and externally positioned to allow for direct contact with cardiac tissue.

3.2.2. Assessment of Wireless Transfer Range

To determine the range of function for the miniaturized pacer, we placed the transmitter and receiver at varying distances apart and with different degrees of misalignment. The average distance between the two implant positions (subcutaneous for the transmitter and inside the ACV for the receiver) was set to 20 mm as demonstrated in **Section 3.1.5. Coil Displacement Measurements** [55]. We thus examined wireless power transfer capacity at distances of 10 mm to

30 mm between the transmitter and receiver. Due to myocardial contractility, the angle between the two components also varies over the cardiac cycle. Thus, we measured up to 45^{o} misalignment in four directions: (1) horizontal x-axis misalignment, (2) horizontal y-axis misalignment, (3) vertical x-axis misalignment, and (4) vertical y-axis misalignment (**Figure 31**).

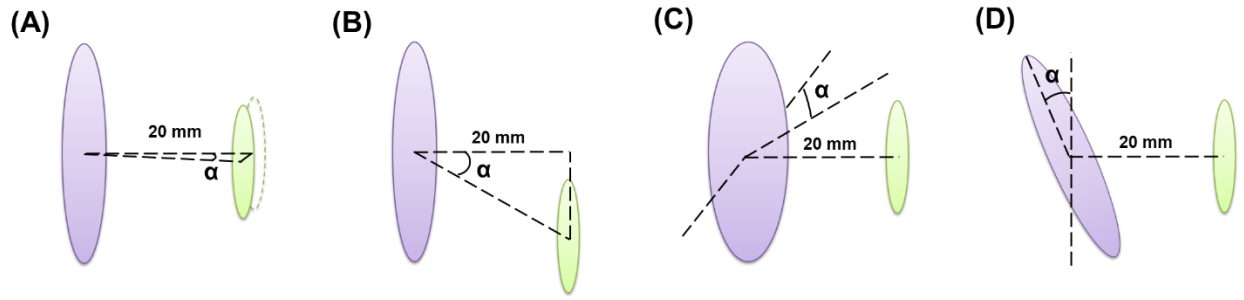

Figure 31: Misalignment Assessment. (A) Coil assessment with horizontal x-axis angular misalignment at angle, *α*, (B) Coil assessment with horizontal y-axis angular misalignment at angle, *α*, (C) Coil assessment with vertical x-axis misalignment at angle, *α*, and (D) Coil assessment with vertical y-axis misalignment at angle, *α*.

All of the measurements were performed with a segment of bovine tissue that included bone, muscle, adipose, and connective tissue, placed between the transmitter and receiver coils (**Figure 32**). We compensated for the change in distance between the components via the addition or removal of layers of swine muscle tissue (which has the greatest level of absorption due to its dielectric properties).

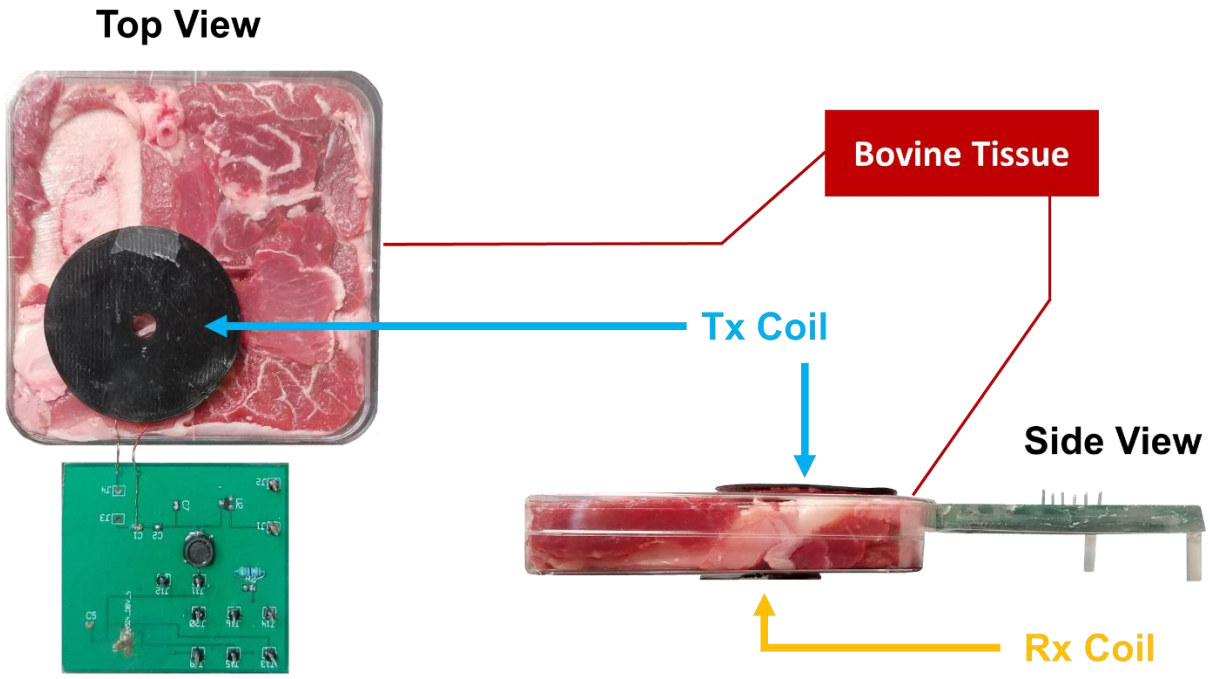

Figure 32: Benchtop Experiments for Miniature Pacer. Photo of experimental setup for benchtop analysis of power transfer efficiency over various distances and misalignments levels. A segment of bovine tissue containing a mixture of muscle, adipose, and bone was placed in between the two coils to mimic the environment of the body.

Output voltage was compared against the mean pacing amplitude of 0.80 V [65] (dotted line at the upper boundary of the red zones in **Figure 33, Figure 34**, and **Figure 35**) and maximum potential amplitude of the market-released leadless pacemaker at 5 V [13] (dotted line at the upper boundary of the green zones in **Figure 33, Figure 34**, and **Figure 35**). To evaluate the potential safety margin for the proposed system, we defined four conservative conditions for testing the wireless pacer:

(1) With pacing durations typically established between 0.2 ms to 1 ms, we elected a 1 ms pulse duration to examine the maximum total power consumption. This power consumption can be reduced up to 80% with a shorter pulse duration (< 1 ms).

(2) In the setting of short intermittent pulse delivery, Specific Absorption Rate (SAR) can be reduced to significantly below the limits set by the Federal Communications Committee (FCC) [38]. We performed our studies using 1.26 W of instantaneous power, equivalent to a low average input power of 1.26 mW as a result of the 1 ms pulse width. The pacer has the potential for a higher voltage amplitude at the stimulating electrodes by increasing this input power.

(3) Cardiothoracic Magnetic Resonance Images (MRI) have demonstrated a mean distance of 20 mm between the location of the subcutaneous transmitter (Tx) in the anterior chest, and the location of the pacer (Rx) in the ACV (**Section 3.1.5. Coil Displacement Measurements**) [55]. The distance between the Tx and Rx was examined at 10 mm greater than the mean anatomical displacement to assess safety margins. As power transfer efficiency (PTE) decreases exponentially over distance, a 30 mm Tx-to-Rx separation demonstrates the extent of the positional safety margin with the given parameters.

(4) To demonstrate the effect of cardiac motion, we simulated Tx-to-Rx misalignment at up to two-fold the angular change measured throughout a cardiac cycle in our MRI-Phantom studies. This wide-range analysis allowed for the assessment of the angular safety margin available in the designed pacer.

As expected, and as shown in **Figure 33B**, output voltage decreased significantly over increasing distance. However, the voltage remained above the 5 V maximum pacing threshold at the mean 20 mm distance from MRI measurements and continued to remain above the 0.8 V

average pacing threshold at up to 10 mm above the estimated distance between the transmitter and receiver implant positions. This is important as it establishes a safety margin for variations in patient anatomy.

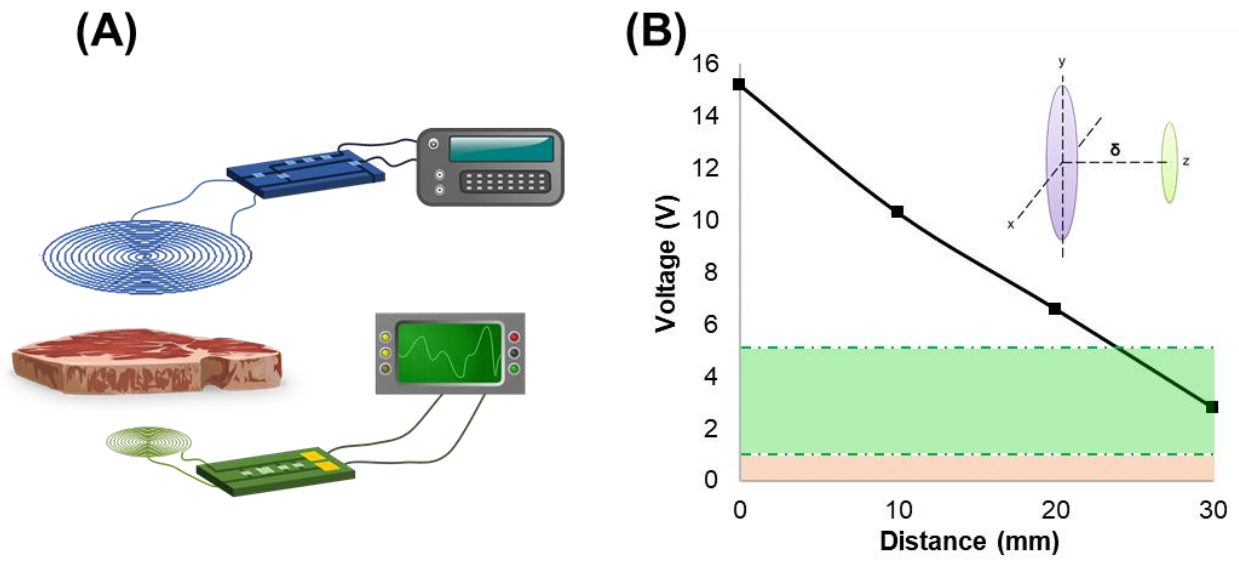

Figure 33: Benchtop Experiments for Displacement Assessment. (A) A schematic of the experimental configuration illustrates the transmitter and receiver position across a segment of bovine tissue. (B) Output voltage decreased as the displacement between the transmitter and receiver, δ, increased from 0 to 30 mm at δ = 20 mm and δ = 30 mm. Output voltage was compared against the average pacing amplitude of 0.80 V (dotted line at the upper boundary of the red zones) and maximum potential pacing amplitude of the market-released leadless pacemaker at 5 V (dotted line at the upper boundary of the green zones).

In addition to maintaining sufficient pacing threshold over an effective range, due to potential variability in implant position as well as changes in angular alignment over the course of the cardiac cycle, it was important that voltage output would also be maintained against changes in misalignment. At 20 mm mean displacement and up to 20^{o} of horizontal or vertical

misalignment, the intravascular pacer consistently achieved a pacing amplitude > 5 V (**Figure 34** and **Figure 35**). The amplitude remained above the mean pacing threshold of 0.80 V in nearly all combinations of displacement and misalignment, except for horizontal misalignments > 40°. At a displacement of 30 mm (10 mm above the mean), the pacing amplitude remained more than twice the mean amplitude of 0.80 V in all cases except for horizontal misalignments > 20°.

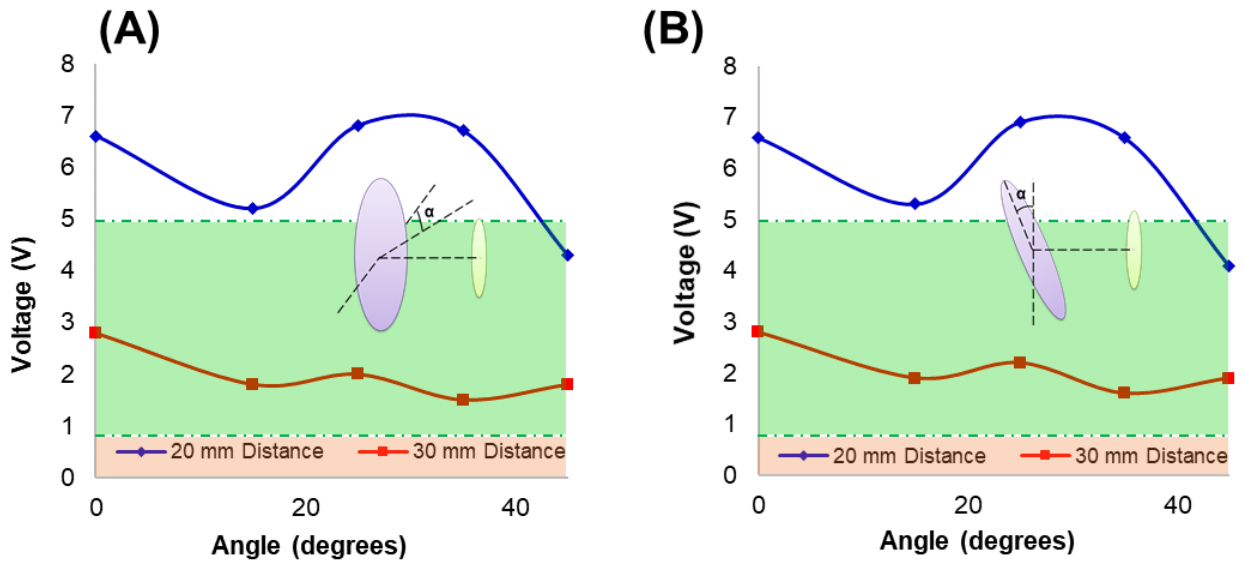

Figure 34: Benchtop Experiments for Vertical Misalignment Assessment. (A) Output voltage fluctuated in response to x-axis vertical misalignment, α, ranging from 0 to 45 degrees at δ = 20 mm and δ = 30 mm. (B) Output voltage fluctuated in response to y-axis vertical misalignment, α, ranging from 0 to 45 degrees at δ = 20 mm and δ = 30 mm. Output voltage was compared against the average pacing amplitude of 0.80 V (dotted line at the upper boundary of the red zones) and maximum potential pacing amplitude of the market-released leadless pacemaker at 5 V (dotted line at the upper boundary of the green zones).

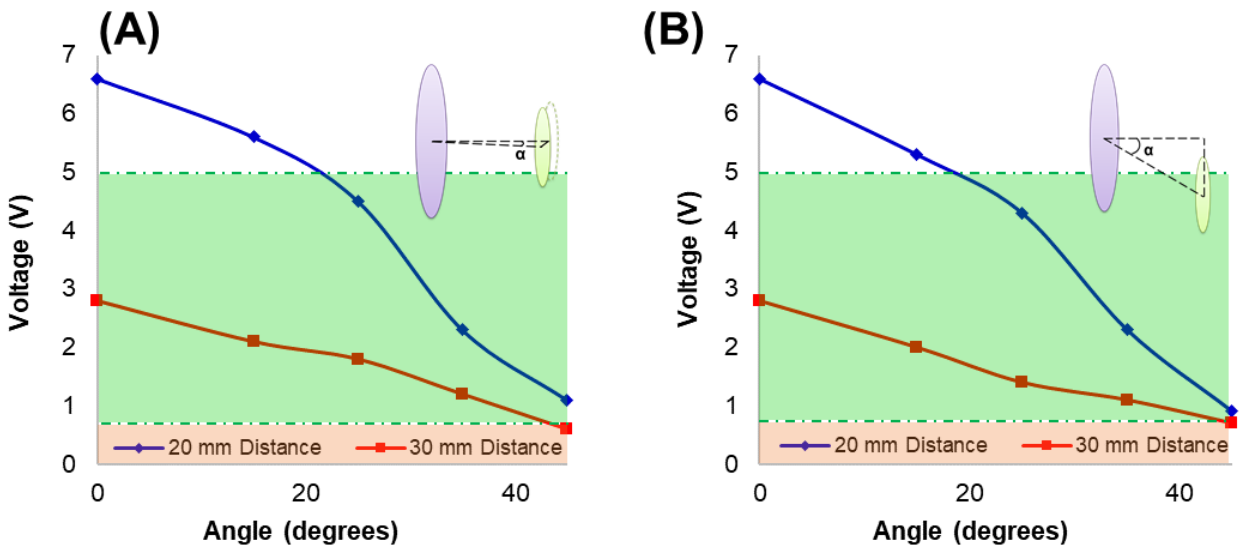

Figure 35: Benchtop Experiments for Horizontal Misalignment Assessment (A) Output voltage decreased in response to x-axis horizontal misalignment, α, ranging from 0 to 45 degrees at δ = 20 mm and δ = 30 mm. (B) Output voltage decreased in response to y-axis horizontal misalignment, α, ranging from 0 to 45 degrees at δ = 20 mm and δ = 30 mm. Output voltage was compared against the average pacing amplitude of 0.80 V (dotted line at the upper boundary of the red zones) and maximum potential pacing amplitude of the market-released leadless pacemaker at 5 V (dotted line at the upper boundary of the green zones).

Also notable is the non-linear relationship between vertical misalignment and voltage amplitude, where power transfer efficiency increased with some degrees of misalignment. This angular adaption is an important characteristic of the designed receiver coil of the pacer unit. The bending of the circular planar loop into the z-axis generates a diagonal capture of the magnetic field; thus, negating the power losses from changes in angular misalignment (**Figure 36**). Notably, in accordance with the illustrated magnetic field lines, this wrapped receiver geometry primarily impacted vertical misalignment as opposed to horizontal misalignment. This phenomenon is also demonstrated in **Figure 34** and **Figure 35**, in which output voltage fluctuations were shown to be

present in vertical misalignment, but not in horizontal misalignment. Furthermore, power transfer efficiency followed this same pattern, with vertical misalignment maintaining a high output threshold at up to 45^{o} misalignment. Finally, this advantage was supplemented by the coil's hollow shape to allow for blood flow through the cylindrical pacer unit.

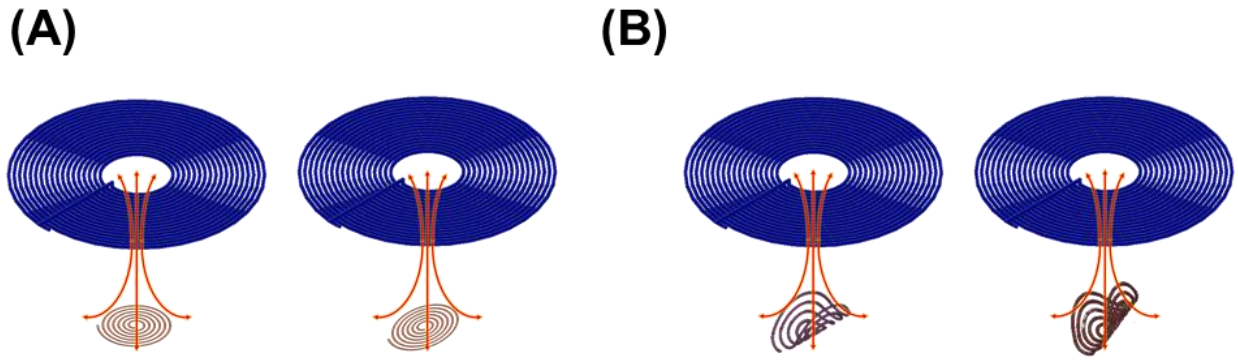

Figure 36: Comparison of Circular vs. Wrapped Half-Cylindrical Coil Geometry (A) The effect of B-field (red arrows) capture is shown with a planar circular receiver coil in the presence of absence of misalignment. (B) The effect of B-field (red arrows) capture is shown with a half-cylindrical receiver coil in the presence of absence of misalignment.

3.2.3 Simulating Pacing Function Across a Cardiac Cycle

We analyzed 4-dimensional (3-dimensions + time) coronal magnetic resonance images (MRIs) of the thorax through a cardiac cycle to determine the relative motion between the implanted transmitter and receiver components. The transmitter, to be implanted in the thoracic cavity anterior to the ribs and sternum, was simulated as an immobile object. The receiver position was simulated by inserting a phantom object in the MRI slices at the location of the ACV (**Figure 37**). We adjusted the size of the phantom to the nearest voxel size relative to the actual device size, resulting in a rectangular phantom object of size 4.14 x 3.60 x 21.31 mm.

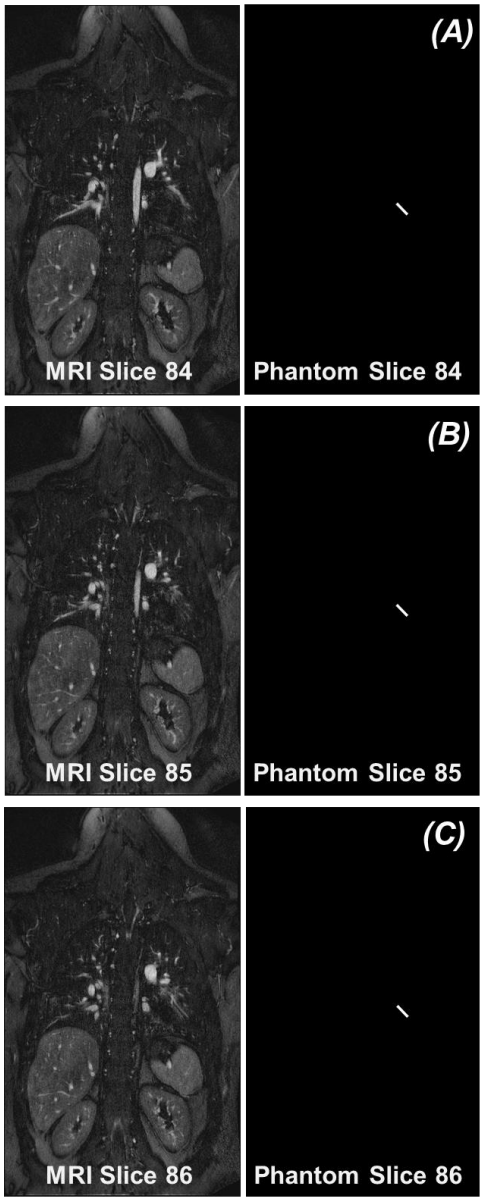

Figure 37: Cardiac Cycle MRI Analysis. (A)-(C) Three layers of coronal MRI slices shown on the left with corresponding "pacer" phantom placements across the three slices on the right to represent the pacer object thickness overlapping with its predicted position in the ACV.

Next, we created four versions of the 3-D phantom image, each containing a red marking in one of the four corners on the larger surface (4.14 x 21.31 mm) of the phantom. These markers served as representative landmarks of the surface of the phantom that would have the greatest

contact with the epicardium. As previously described [67], deformable image registration (DIR) was applied on each time point of the 4-D thoracic MRI to generate 3-D displacement fields that represented the instantaneous cardiac motion at discrete time points in the cardiac cycle. To simulate the moving phantom at any given time point, the 3-D phantom image of the previous time point was transformed using the 3-D displacement field that was calculated for the given time point. Thus, a 4-D phantom image was generated for each marked version of the original 3-D phantom to simulate its motion throughout the cardiac cycle.

To spatially track the landmarks over time, we first extracted the red color spectrum from each marked 4-D phantom image. In each 3-D image of each 4-D phantom image, we determined the 3-D location of the landmark by calculating the weighted average of non-zero pixel, using the pixel intensities as the weights. The resulting output was four 3-D points in each time point representing four corners of the phantom in a single averaged slice (**Figure 38**).

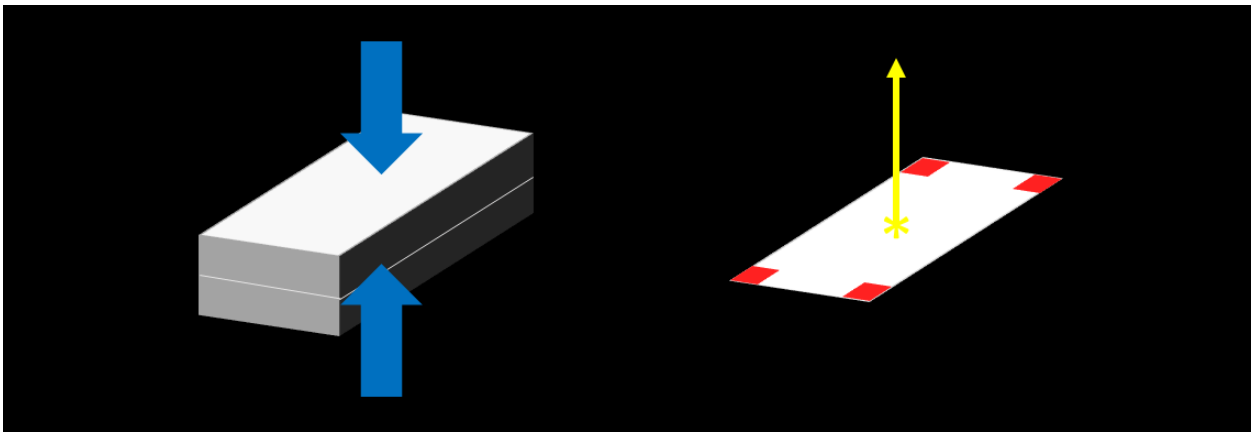

Figure 38: Phantom Tracing Method. The location of the red landmarks was calculated by taking the average of their position to create a 2-D version of the object. The centroid and normal vector were then computed based on the averaged red marks that represented the four corners.

Next, we computed the centroid of the four points in each time point to trace the changing 3-D position of the phantom relative to the initial position. We also calculated for the normal vector to the four points in each time point to trace the changing angular alignment of the phantom relative to the initial time point (**Figure 38**).

We started simulating the device motion effects by first modeling the transmitter and receiver coils in Solidworks software (outlined in red in **Figure 39A**). The transmitter was modeled with 18 circular turns of a 23 AWG wire with spacing equivalent to the wire diameter, resulting in an inner diameter of 10 mm and outer diameter of 40 mm. The receiver was modeled with 5 circular turns of a 30 AWG wire with spacing equivalent to the wire diameter connected to a meandering tail, all of which was folded into a half-cylindrical shape with a diameter of 3 mm and length of 15 mm. Next, we imported the components into ANSYS Maxwell simulation software and positioned them at an initial mean distance of 20 mm apart. The position and angle of the receiver in each frame was adjusted based on computed centroid position and normal vector of the phantom from the MRI tracings.

Using the Eddy Current solver in ANSYS Maxwell, we simulated the magnetic (B) field, inductance, resistance, and coupling coefficient resulting from the 13.56 MHz alternating current in the transmitting coil and its impact on the receiving coil. The simulation profile was established with Current Excitation in the transmitter and receiver with a 90-degree phase shift in the receiver AC current. The meshing was set up as described in **Section 3.1.6.1 Simulation Studies**. An air box geometry of size 500 x 500 x 500 mm with a Radiation boundary was created to surround the transmitter and receiver coils. Convergence was established with a 2 percent error.

The coils' internal resistance and inductance as well as the coupling coefficient between the interacting components were computed by the solver and imported into PSPICE Electronic

Circuit Optimization & Simulation software. We simulated the circuit of **Figure 39A** with a 1000-ohm load, which is the impedance of a typical high-impedance pacemaker stimulation lead electrode. We measured the voltage across the load in the receiver given an instantaneous input power of 1.26 W to the transmitter (equivalent to 1.26 mW of power consumption using 1 ms pulse duration and 60 BPM heart rate).

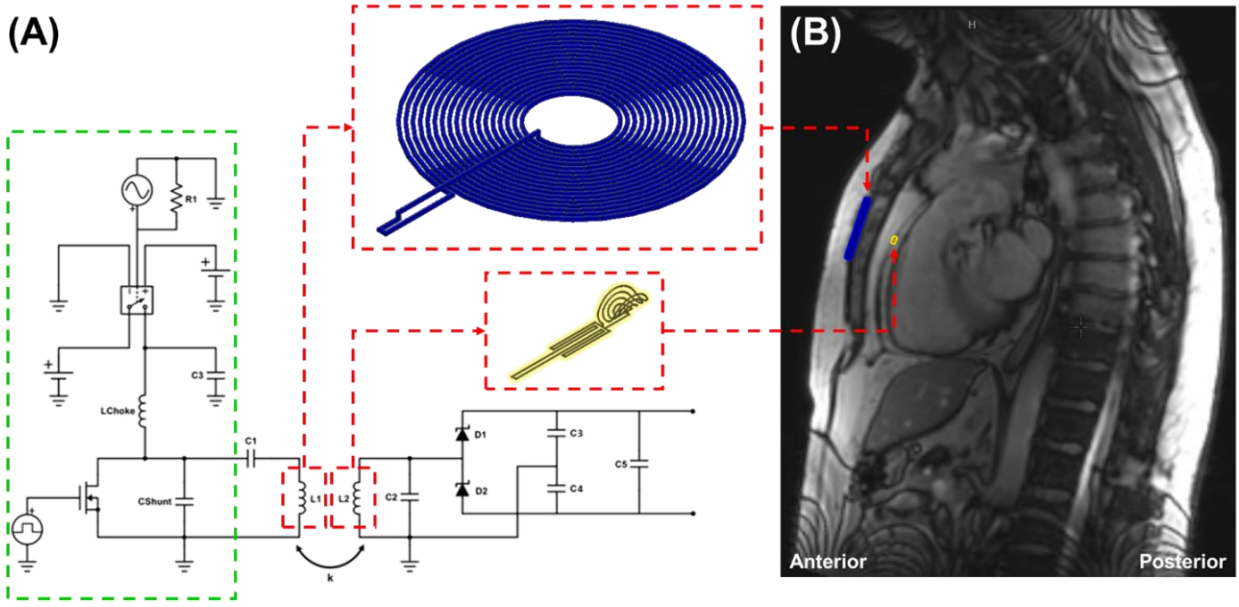

Figure 39: Circuit and Coil Design. (A) Transmitter and receiver circuit design. Highlighted in the green box is the control circuitry that determines pacing rate, rhythm, and level of power input. Highlighted in red are the transmitter and receiver coils as positioned in the circuit as well as their structure. (B) Anatomical position of the subcutaneous transmitter in blue and intravascular receiver in yellow, depicted on a sagittal section of a human MRI.

The results of the phantom tracing throughout the cardiac cycle for the determination of the relative motion (position and angle) between the subcutaneous transmitter and pacer unit can be seen in **Figure 40A-i-ix**.

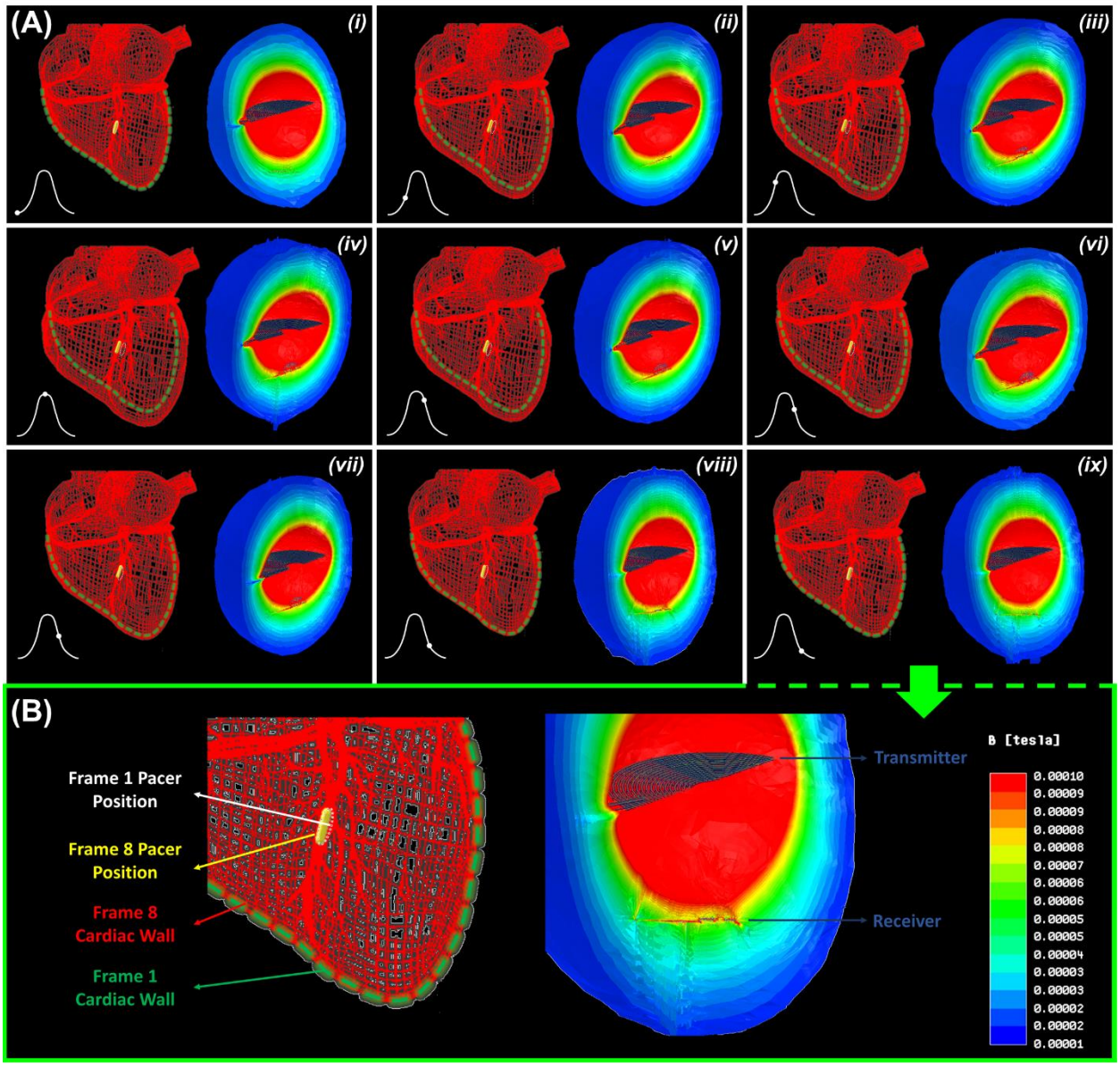

Figure 40: Cardiac Cycle Simulation Experiments. (A) Each box represents a single time frame in the cardiac cycle in (i)-(ix). Cardiac contraction and consequential pacer positional and angular motion are shown in the schematic on the left inset. Stimulation of the interaction between the transmitter and receiver coil is demonstrated by the magnetic field shown on the right inset. (B) demonstrates a zoomed-in view of the events in box (ix).

The magnetic field (B) generated from the AC excitation in the transmitter coil was determined over nine time points in the cardiac cycle (right inset of **Figure 40A-i-ix**). Inductive power transfer simulations at the end of systole (**Figure 40A-i**) and diastole (**Figure 40A-iv**) demonstrated sufficient power transfer at the two spectra of the cardiac cycle. The change in pacer position compared to the initial time frame and the resulting B-field interaction between the pacer and its transmitter (enhanced in zoomed-in view in **Figure 40A-x**) revealed the effect of cardiac contraction-mediated transmitter-receiver interaction. The maximum difference in field potential was observed when the pacer was in the red region of the B-field (B = 0.0001 T) (**Figure 40A-vi**), as compared to the green region (B = 0.00005 T) (**Figure 40A-i**).

The outcome of the B-field strength was demonstrated in terms of the change in coupling coefficient (**Figure 41A**), which directly correlates with power transfer efficiency (**Figure 41B**). PTE directly affects the output voltage, which remained above the peak voltage capacity of 5V throughout the recorded cycle (**Figure 41C**). The capacity to deliver short intermittent pulses allowed us to maintain this threshold with low power consumption and tissue absorption despite the low PTE ranging from 2.7% to 7.6%.

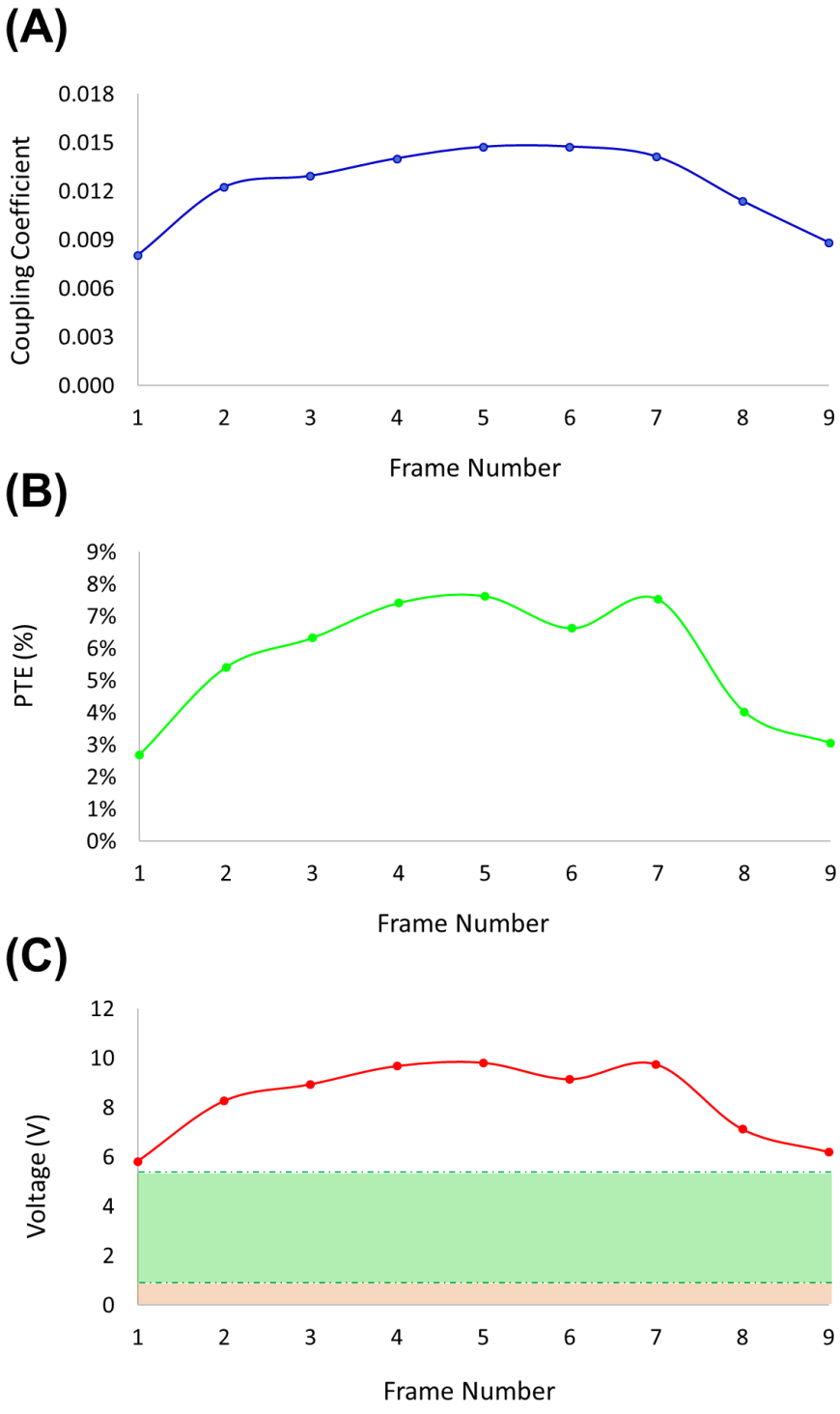

Figure 41: Cardiac Cycle Simulation Results. (A) Computed coupling coefficient over the nine captured frames of the cardiac cycle. (B) Computed PTE over the nine captured frames of the cardiac

cycle (C) Computed maximum potential voltage threshold over the nine captured frames of the cardiac cycle given an average input power of 1.26 mW.

Similar to the bench experiments, small vertical misalignments engendered an increase in the coupling coefficient and, therefore, in power transfer efficiency and output voltage (**Figure 41A-C**). Also, although pacing occurs only once per cycle, our simulation experiments established the fundamental capacity to maintain sufficient power transmission throughout the cardiac cycle.

Finally, we computed SAR using the simulated E-Field in ANSYS Maxwell as needed for Equation **(**12**)**:

$$SAR = \frac{\sigma E^2}{\rho} \tag{12}$$

where σ is the electrical conductivity of the tissue and ρ is the mass density of the tissue.

Notably, SAR remained significantly below the FCC safety limits. The electric (E) field strength at peak coupling (**Figure 42A**) was computed to determine maximum tissue absorption. Based on peak E-field strength (**Figure 42A**), conductivity values, and density values (**Figure 42B**), maximum absorption at 1.26 mW of input power was computed as 0.07 W/kg. This was nearly 23 times less than the FCC safety limit of 1.6 W/kg. For this reason, the simulations established a basis for complying with the SAR safety standards while maintaining the capacity to increase input power to the intravascular pacer in the setting of anatomical variations that deviate significantly from the mean MRI-based measurements.

(A)

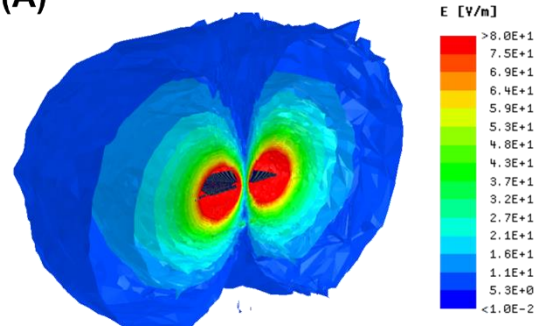

(B)

Tissue	Conductivity (S/m)	Density (Kg/m^3)
Bone (Cancellous)	0.128	1178
Cartilage	0.383	1100
Muscle	0.628	1090
Adipose	0.055	911

Figure 42: Simulation and Data for SAR Calculations. (A) Electric field simulation of Frame 5 of the cardiac cycle at which time point maximum coupling was observed and thus the largest E-field would be present. (B) Various tissue conductivities and densities, which, in combination with the Electric field, determine SAR. The combination generated by muscle tissue would result in the highest absorptions levels.

3.2.4. Ex Vivo Pacing of Porcine Heart

As part of the next validation step, we performed *ex vivo* experiments on male Yorkshire pigs (>50 kg, >14 weeks age, n=4). All animal studies were approved by the UCLA Office of Animal Research in compliance with the UCLA IACUC protocols. The pigs were anesthetized with intramuscular Ketamine and Midazolam. Fentanyl was given for pain control during surgery. 1-3% isoflurane was given to maintain general anesthesia for the duration of the procedure. A 6F introducer sheath was inserted percutaneously using the Seldinger technique into the right or left femoral artery to monitor blood pressure. Bupivacaine and Lidocaine was injected SC in the chest. A midline sternal incision was made to access the thorax and was widened using rib spreaders to expose the heart. The pericardium was incised to access the heart.

The animal was euthanized using a combination of pentobarbital and phenytoin. We then inserted the device via an incision made in the anterior cardiac vein downstream the implant

position. The intravascular pacer was inserted into the vessel through the opening. We positioned the wireless power transmitter at 20 mm distance to the intravascular pacer. Pacing was initiated at a rate of 60 BPM immediately post-euthanasia to minimize cellular apoptosis and release of intracellular electrolytes. EKG readings were observed and recorded to examine pacing function.

A schematic of the deployment of the proposed intravascular pacer (**Figure 43B**) illustrates the accessibility of the coronary sinus similar to that of current pacemaker leads for left ventricular (LV) pacing (**Figure 43A**).

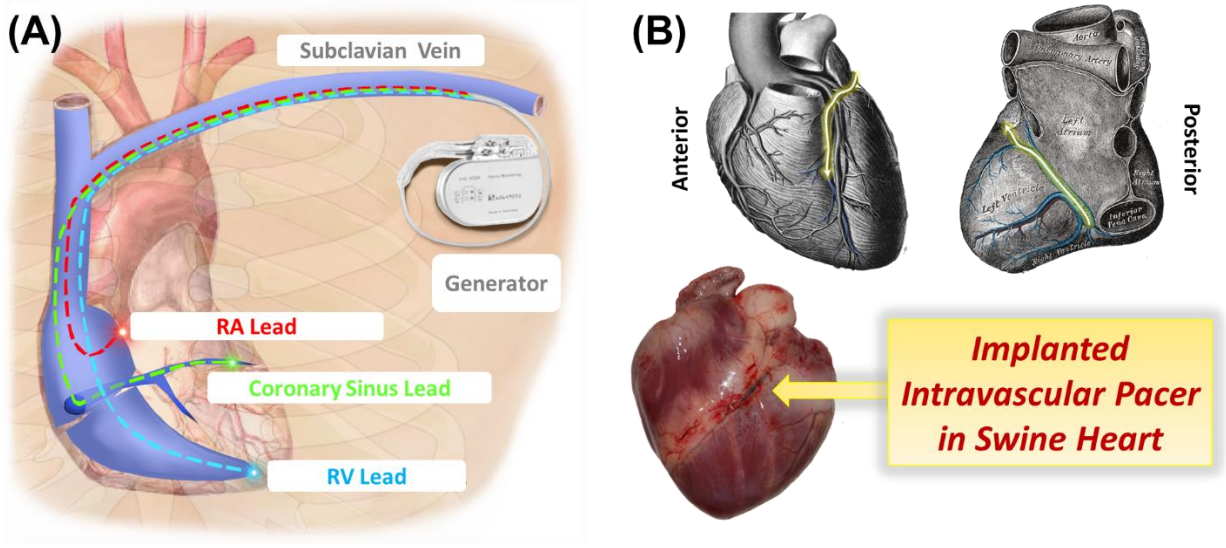

Figure 43: Comparison of Device Access Point (A) A schematic of the deployment of current pacemaker leads (dotted lines). (B) The upper panel depicts the deployment of the proposed intravascular wireless pacer (yellow lines). The lower panel shows the Yorkshire heart with the proposed pacer deployed to the ACV as indicated by the arrow.

The deployed pacemaker into the ACV of Yorkshire pig hearts can be seen in the anatomical photo of **Figure 43B**. Pacing was initiated via the wirelessly powered intravascular pacer at 60 BPM immediately post-euthanasia to minimize the effects of cell death.

In comparison with the normal resting rhythm at 75 BPM with P, QRS, and T waves (**Figure 44A**), the electrocardiogram of artificial pacing demonstrated the paced wide QRS complex rhythm (**Figure 44B**). Once power transmission was terminated from the subcutaneous control unit (**Figure 39A**) and, ultimately the wireless pacer unit, the EKG tracing was converted to a flat-line (shown as the green region in **Figure 44B**), supporting the pacer-dependence of the euthanized pig heart.

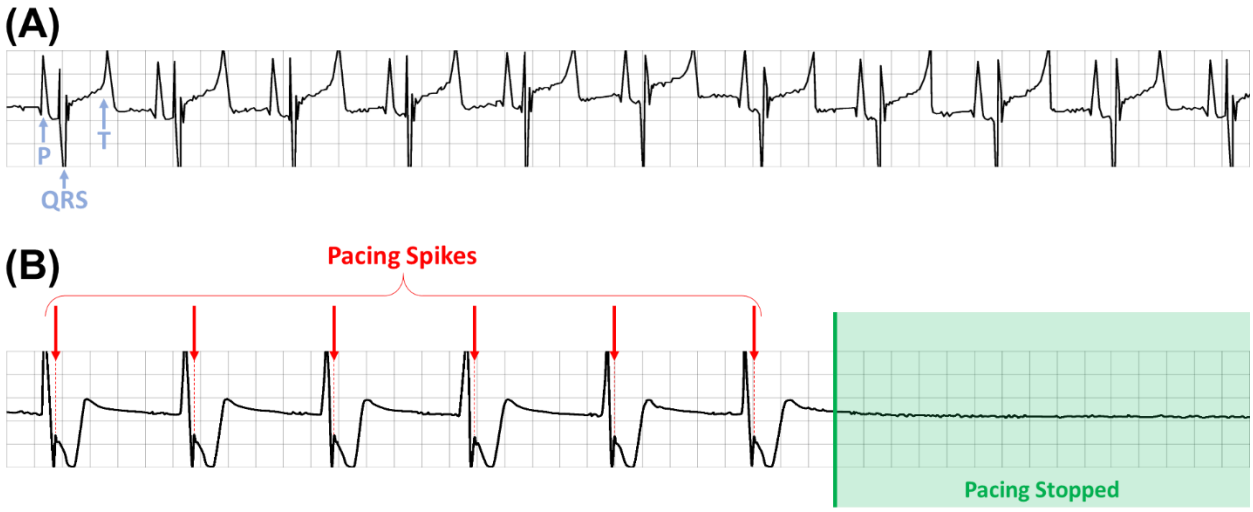

Figure 44: Ex Vivo Animal Experiments. (A) EKG demonstrates normal sinus rhythm with P, QRS, and T waves. (B) EKG of Yorkshire pig post-euthanasia demonstrates wide-QRS complex rhythm with pacing spikes at the set rate of 60 BPM. Upon termination of pacing, the EKG flat line supports the pacing-dependent rhythm post-euthanasia.

3.2.5. In Vivo Pacing of Porcine Heart

We performed *in vivo* experiments on male Yorkshire pigs (>50 kg, >14 weeks age, n=2). All animal studies were approved by the UCLA Office of Animal Research in compliance with the UCLA IACUC protocols. The pigs were anesthetized with intramuscular Ketamine and Midazolam. Fentanyl was given for pain control during surgery. 1-3% isoflurane was given to

maintain general anesthesia for the duration of the procedure. A 6F introducer sheath was inserted percutaneously using the Seldinger technique into the right or left femoral artery to monitor blood pressure. Bupivacaine and Lidocaine was injected SC in the chest. A midline sternal incision was made to access the thorax and was widened using rib spreaders to expose the heart. The pericardium was incised to access the heart. A small incision was made in the distal end of the vessel. A dilator was used to improve delivery into the vessel. It is important to note the challenge in placing the 3 mm diameter pacer inside the pig vessel due to (1) the contraction of the heart during *in vivo* placement, and (2) the size of the pig vessel being smaller than that of humans, thus making implantation more difficult.

The intravascular pacer was inserted into the ACV through the incision (**Figure 45A-C**). We positioned the transmitter against the chest wall at a distance ranging from 15 to 18 mm (**Figure 45D**). Pacing was initiated at a rate of 120 BPM to override the resting heart rate of the animal. EKG readings were observed and recorded to examine pacing function.

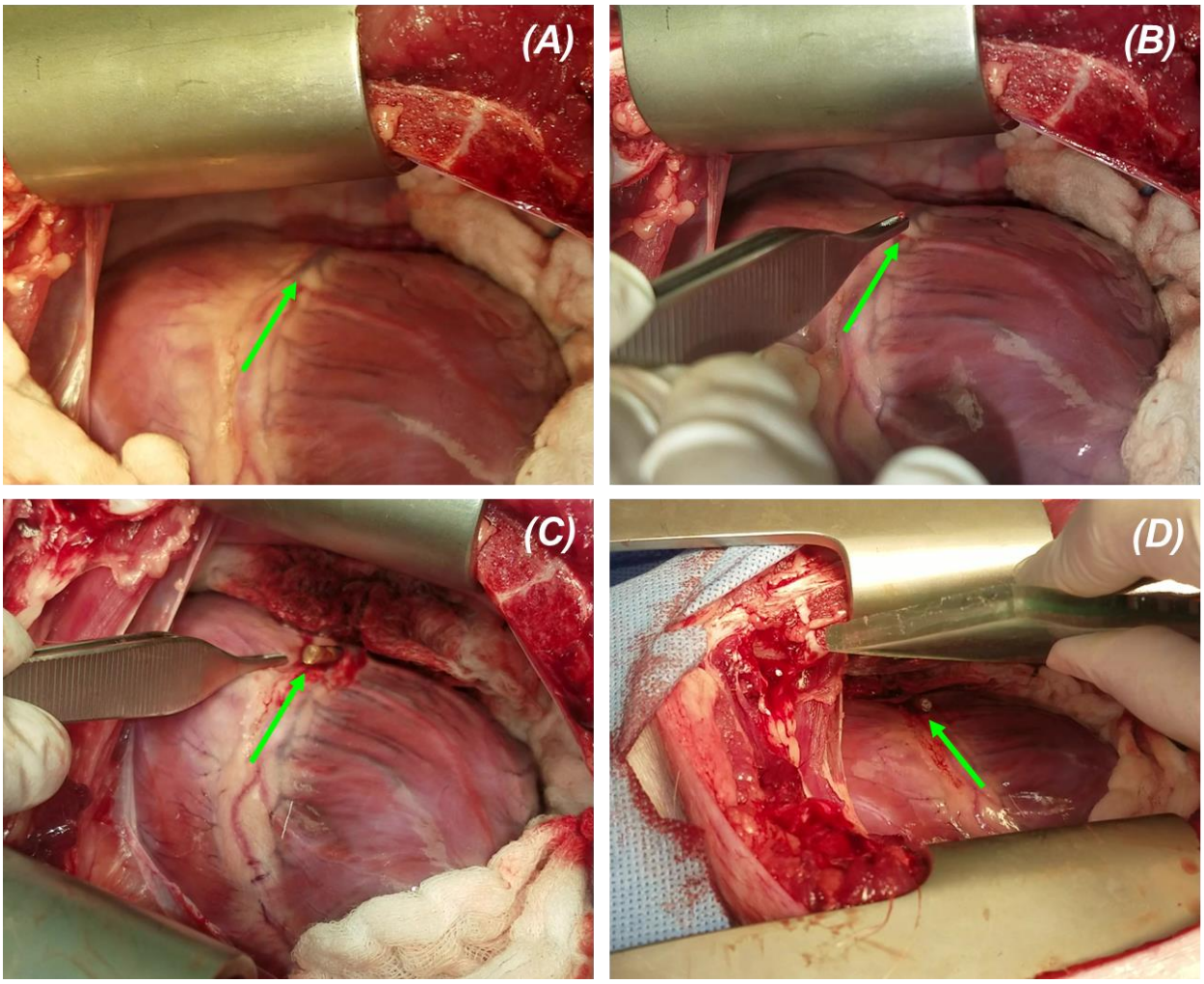

Figure 45: In vivo experimental setup. (A) arrow points to ACV, (B) arrows points to insertion position of the pacer, (C) arrow points to partially inserted pacer, and (D) arrow points to tail end of pacer during pacing with transmitter at 15 to 18 mm above the pacer against the anterior chest wall.

Once the pacing device was deployed to the ACV of the contracting porcine heart, the normal sinus rhythm was overridden by setting the artificial pacing rate above the resting heart rate at 120 BPM. This pacing rate was controlled by modulating the power output of the subcutaneous unit (transmitter) without the requirement of a programming unit inside the pacer (receiver). In comparison to the normal resting rhythm at 75 BPM with P, QRS, and T waves (**Figure 46A**), upon initiation of inductive power transfer, the fast rhythm (120 BPM) of artificial

pacing was observed with visible pacing spikes and wide QRS complex rhythm (**Figure 46B**). Upon termination of pacing, this rhythm converted to the normal sinus rhythm (shown as the green region in **Figure 46B**).

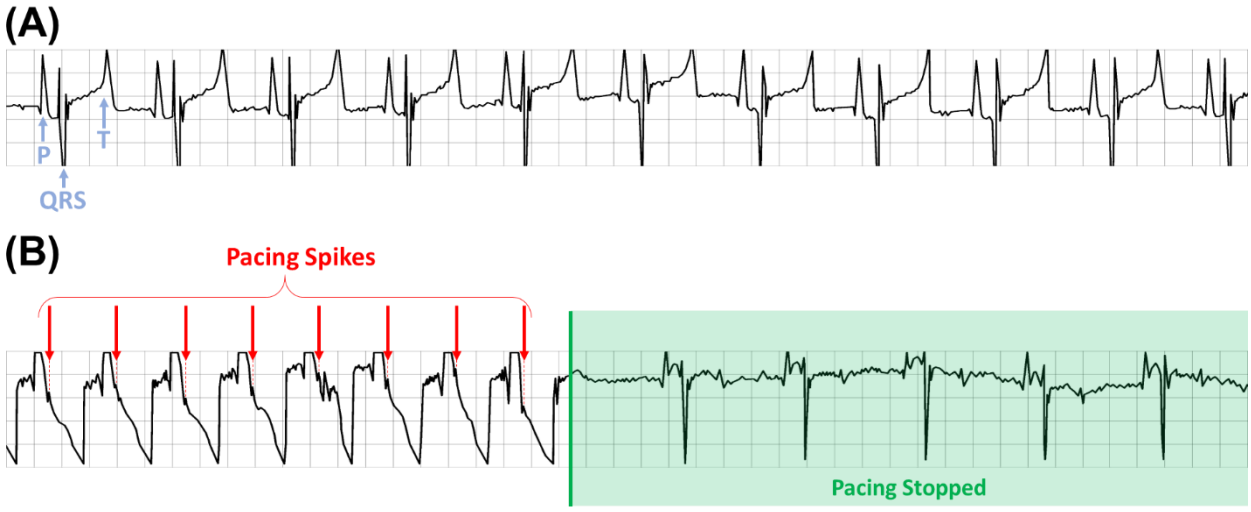

Figure 46: In Vivo Animal Experiments. (A) EKG demonstrates normal sinus rhythm with P, QRS, and T waves. (B) EKG of Yorkshire pig undergoing *in vivo* pacing of at 120 BPM using the proposed wireless pacemaker. Rhythm returned to normal sinus rhythm once pacing was terminated.

As a demonstration of the changes resulting from the implementation of the proposed pacemaker, chest radiographs of a lead-based device implant (**Figure 47A**) and the proposed leadless pacer (**Figure 47B**) are shown. The comparison x-rays reveal the pacer's significant reduction in surface area and volume, which may help reduce infection in addition to the mechanical advantages incurred from an externally positioned pacer.

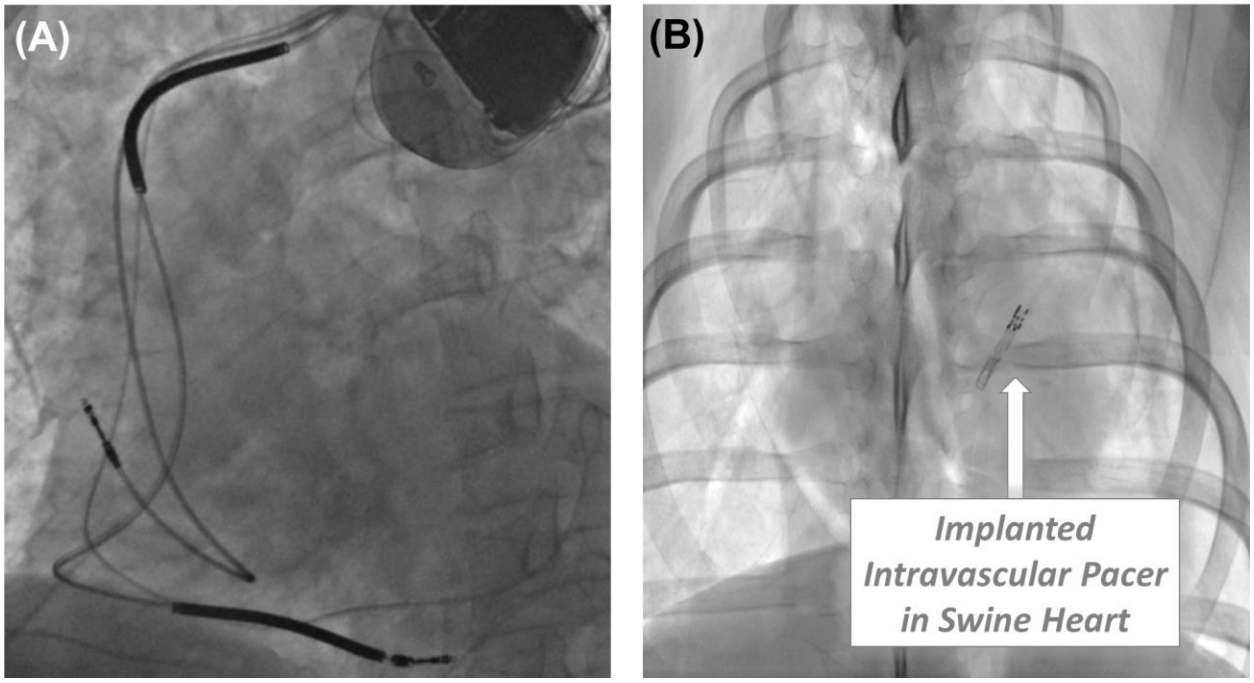

Figure 47: Comparison of Chest Radiographs. (A) X-ray image of current leads deployed to the cardiac chambers in a human [P2]. (B) X-ray image of the proposed wireless pacer as positioned in the ACV of a Yorkshire heart.

4. WIRELESS POWER TRANSFER IN CHARGING SUB-SYSTEM

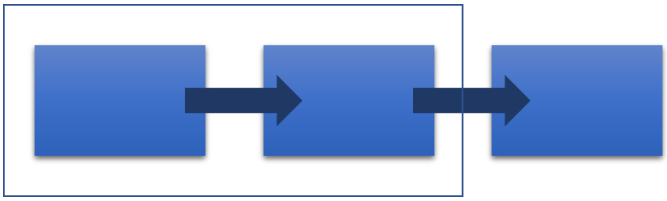

4.1. COIL DESIGN OPTIMIZATION

4.1.1. SIMULATION STUDIES

The external unit of the Charging Sub-System (CSS) is the primary source of power in our multi-level system and encounters the least constraints. The transmitter coil design of this unit was primarily defined by practical size and weight limits of a wearable chest strap. This was set to a maximum volume of 100 mm x 100 mm x 10 mm. The subcutaneous unit, shared between the CSS and SSS, determined the constraints of the CSS receiver coil. Similar to the transmitter coil of the SSS, the receiver coil of the CSS was designed as a planar coil to minimize thickness with a maximum diameter of 40 mm. The operating frequency was set to 6.78 MHz and the power transfer range was set to 25 mm, based on the previously measured mean anatomical distance between the surface of the skin and the sternum [68].

These constraints were implemented in a Monte Carlo simulation for examining all potential combinations to determine the optimal conditions that would result in the highest power transfer efficiency. The variables of the system were defined with a uniform distribution based on the aforementioned conditions as shown in **Table II**.

Table II: Variables for determining optimal design and performing sensitivity analysis for the transmitter (Tx) and receiver (Rx) coils of the CSS.

Variable	Variable Symbol	Distribution
Tx Wire Gauge	G_1	10 AWG - 38 AWG
Tx Inner Radius	$R_{i,1}$	3 mm to 50 mm
Tx Outer Radius	$R_{o,1}$	3 mm to 50 mm
Tx Height	H_1	1 mm to 10 mm
Rx Wire Gauge	G_2	18 AWG - 38 AWG
Rx Inner Radius	$R_{i,2}$	3 mm to 20 mm
Rx Outer Radius	$R_{o,2}$	3 mm to 20 mm

The variables were iteratively inserted into a series of functions to arrive at the output of PTE, as defined by Equation (13) [37]:

$$\eta = \frac{k^2 Q_1 Q_{2L}}{1 + k^2 Q_1 Q_{2L}} . \frac{Q_{2L}}{Q_L} \tag{13}$$

where k is the coupling coefficient, Q_1 is the quality factor of the transmitter coil, Q_2 is the quality factor of the receiver coil, $Q_{2L} = Q_2 Q_L / Q_2 + Q_L$, and $Q_L = R_{Load} / 2\pi f L_2$.

The coupling coefficient is independent of the operating frequency but highly dependent on coil geometry and the relative position of coils [37]:

$$k = \frac{r_1^2 r_2^2}{\sqrt{r_1 r_2}\left(\sqrt{r_1^2 + D^2}\right)^3} \, cos(\theta) \tag{14}$$

where r_1 is the diameter of the transmitter, r_2 is the diameter of the receiver, D is the distance between the transmitter and receiver, and θ is the misalignment angle.

The quality factor of the coils can be determined using Equation (15) [57]:

$$Q = \frac{2\pi f L}{R_{eff}} \tag{15}$$

where f is the operating frequency, L is antenna inductance, and R_{eff} is the effective ohmic losses.

To find R_{eff} at our selected operating frequency, we must first begin with the DC resistance of the coil, as defined by Equation (16) [57]:

$$R_{DC} = \frac{l}{\sigma \pi a^2} \tag{16}$$

where l is the length of the coil, σ is the electrical conductivity of the tissue, and a is the radius of the wire.

We further analyze the ohmic losses by taking into account the impact of alternating current on coil resistance. AC resistance of a coil is impacted by two main factors. The first is the skin effect, which results in the primary distribution of current density to the surface of the current-carrying conductor. This results in an effective reduction in the cross-sectional area through which current travels, thus ultimately increasing resistance. Dowell presented an estimation for this effect by transforming the turns of a coil into an equivalent foil (**Figure 48D**). The AC resistance of the coil for each "foil" layer as a result of skin effect is then defined by Equation (17) [69]:

$$R_{AC} = R_{DC}\xi' \left(\frac{\sinh 2\xi' + \sin 2\xi'}{\cosh 2\xi' - \sin 2\xi'} \right) \tag{17}$$

where ξ' is defined by Equation (18):

$$\xi' = \xi\sqrt{\eta} \tag{18}$$

in which porosity coefficient, η, is defined by Equation (19):

$$\eta = \frac{Na}{b} \tag{19}$$

and ξ is defined by Equation (20):

$$\xi = d/\delta \tag{20}$$

where skin depth, δ, is defined by Equation (21):

$$\delta = \frac{1}{\sqrt{\pi f \mu_o \mu_r \sigma}} \tag{21}$$

where N is the number of turns in the coil, a is each square width, b is the window width, d is the wire diameter, μ_o is the permeability of the surrounding material, and μ_r is the permeability of the conductor material.

The second factor impacting coil AC resistance is the proximity effect, which is a result of further redistribution of current as a result of the presence of a nearby current-carrying conductor. Using the Dowell method, the AC resistance for the *m*th "foil" layer as a result of the proximity effect can be computed using Equation (22) [69]:

$$R_{AC} = \frac{2}{3} R_{DC} \xi' (m^2 - 1) \left(\frac{sinh\, 2\xi' - sin\, 2\xi'}{cosh\, 2\xi' + sin\, 2\xi'} \right) \tag{22}$$

The resistance of the full length of the coil is then defined by Equation (23):

$$R_{AC} = \sum_{m=1}^{M} R_{AC,m} \tag{23}$$

where M is the total number of layers.

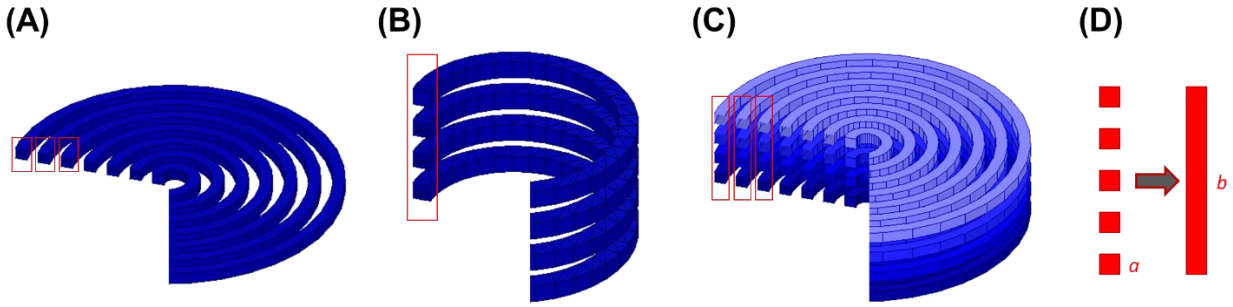

Figure 48: Transmitter Coil Geometries. (A) Planar circular coil with N-turns, (B) multi-layer circular coil with a single turn. (C) Multi-layer circular coil with N-turns. (D) Conversion of turns of coils into an equivalent foil layer, where the red boxes in (A)-(C) represent each of the multi-turn layers that are converted into an equivalent foil layer.

The inductance of each coil was calculated based on the coil geometry. Three potential transmitter coil geometries were examined for this study: (1) planar circular coil with N-turns, (2) multi-layer circular coil with a single turn, and (3) multi-layer circular coil with N-turns (**Figure 48A-C**, respectively).

The inductance for a planar circular coil with N-turns (**Figure 48A**) can be estimated using Equation (24) [70], [71]:

$$L = \frac{(0.3937)\left(N * \frac{r_i + r_o}{2}\right)^2}{8\left(\frac{r_i + r_o}{2}\right) + 11(r_o - r_i)}\ \mu H \tag{24}$$

and the inductance for a multi-layer circular coil with a single turn (**Figure 48B**) can be estimated by Equation (25) [70], [71]:

$$L = \frac{(r_i N)^2}{22.9 r_i + 25.4 h}\ \mu H \tag{25}$$

and the inductance for a multi-layer circular coil with N-turns (**Figure 48C**) can be estimated by Equation (26) [70], [71]:

$$L = \frac{(0.31)\left(N * \frac{r_i + r_o}{2}\right)^2}{6\left(\frac{r_i + r_o}{2}\right) + 9h + 10(r_o - r_i)}\ \mu H \tag{26}$$

where r_i is the inner coil radius (cm), r_o is the outer coil radius (cm), h is coil height (cm), a is wire diameter and spacing between turns, and

$N = \frac{1}{2}\left(\frac{r_o - r_i}{a} + 1\right)$ for a planar circular coil with N-turns

$N = \frac{1}{2}\left(\frac{h}{a}\right)$ for a multi-layer circular coil with a single turn

$N = \frac{1}{4}\left(\frac{r_o - r_i}{a} + 1\right)\left(\frac{h}{a}\right)$ for a multi-layer circular coil with a single turn

Using the variable and function definitions above:

- 147,377,664 total combinations were produced, with
- 9,664,704 combinations for a planar circular transmitter coil with N-turns,
- 24,204,096 combinations for a multi-layer circular transmitter coil with a single turn, and
- 113,508,864 combinations multi-layer circular transmitter coil with N-turns.

The receiver, limited to the confined of the subcutaneous unit, was only simulated as a planar circular coil with N-turns.

The optimal scenario for each coil design is shown in **Table III**, with the most optimal design being a multi-layer circular transmitter coil with N-turns in combination with the planar circular receiver coil with N-turns (**Figure 49**).

Table III: Optimal design variables for the transmitter (Tx) and receiver (Rx) coils

Tx Coil Type	**Planar, N-Turns**	**Multi-Layer, Single Turn**	**Multi-Layer, N-Turns**
Tx Wire Gauge	10 AWG	10 AWG	38 AWG
Tx Inner Radius	10.00 mm	45.00 mm	9.000 mm
Tx Outer Radius	33.31 mm	47.59 mm	36.90 mm
Tx Height	2.590 mm	10.36 mm	9.000 mm
Rx Coil Type	**Planar, N-Turns**	**Planar, N-Turns**	**Planar, N-Turns**
Rx Wire Gauge	19 AWG	19 AWG	28 AWG
Rx Inner Radius	8.000 mm	8.000 mm	3.000 mm
Rx Outer Radius	19.83 mm	19.77 mm	19.32 mm

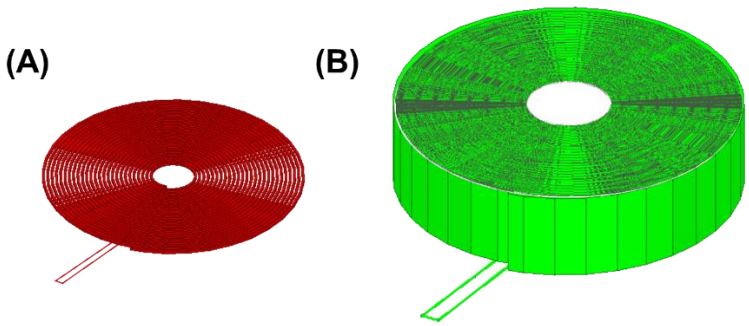

Figure 49: Optimal CSS Coil Designs. (A) Optimal planar coil with N-turns design for the CSS receiver coil. (B) Optimal multi-turn coil with N-turns for the CSS transmitter coil.

Furthermore, the correlation between each variable and PTE was independently plotted. To perform this analysis for each of the three coil designs, all variables, except the variable of interest, were kept constant. The resulting PTE was then plotted against the variable of interest. This process was repeated for up to 1000 random samples, and then normalized and averaged over the selected samples. These normalized values were then plotted for each transmitter coil design as shown in **Figure 50**, **Figure 51**, and **Figure 52** to demonstrate correlations between each variable and PTE.

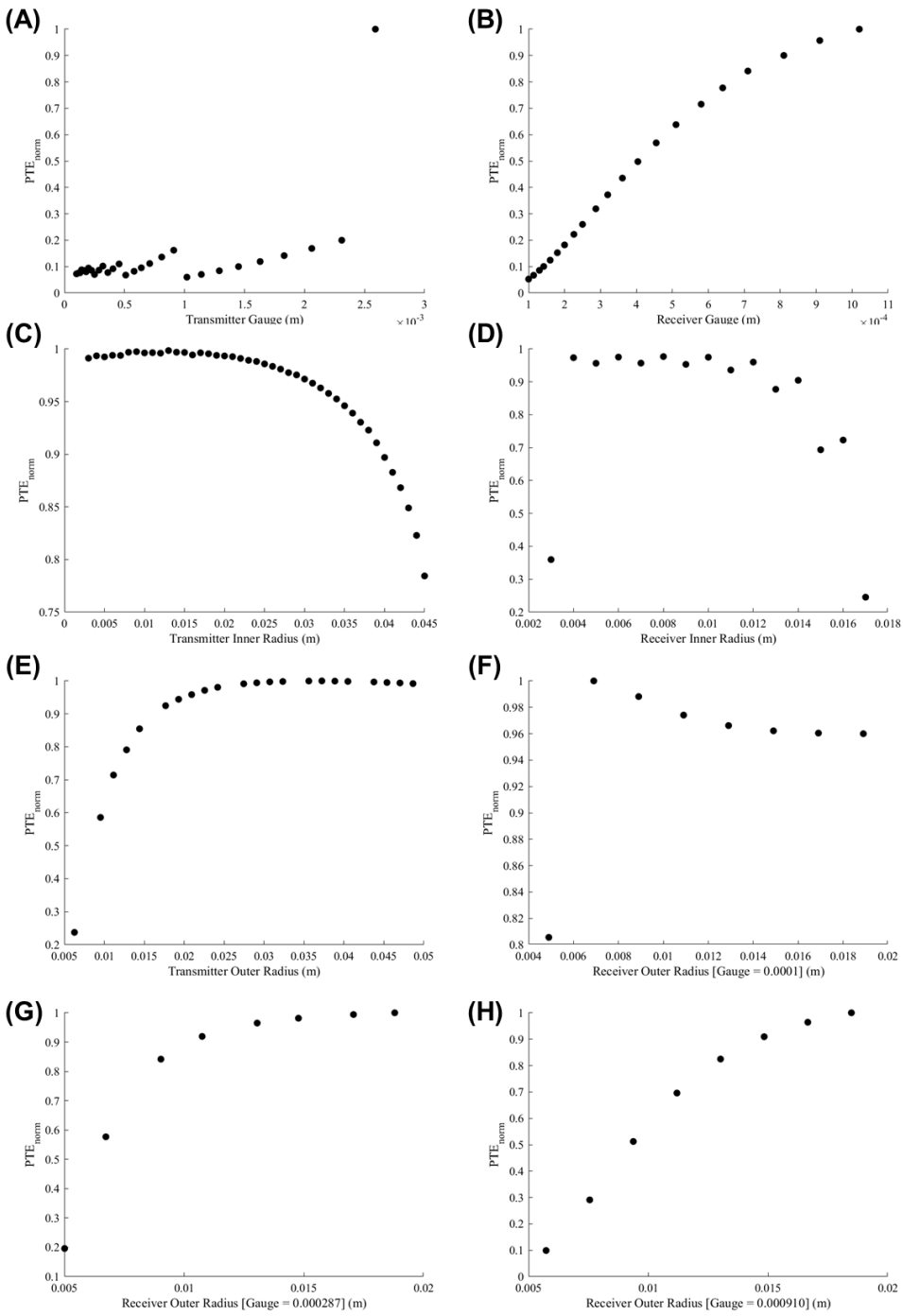

Figure 50: Variable correlations vs. PTE for Planar with N-Turns transmitter (Tx) coil and Planar with N-Turns receiver (Rx) coil (A) Tx gauge, (B) Rx gauge, (C) Tx inner radius, (D) Rx inner radius, (E) Tx outer radius, (F) Rx outer radius at gauge set to 0.0001, (G) Rx outer radius at gauge set to 0.000287, (H) Rx outer radius at gauge set to 0.000910

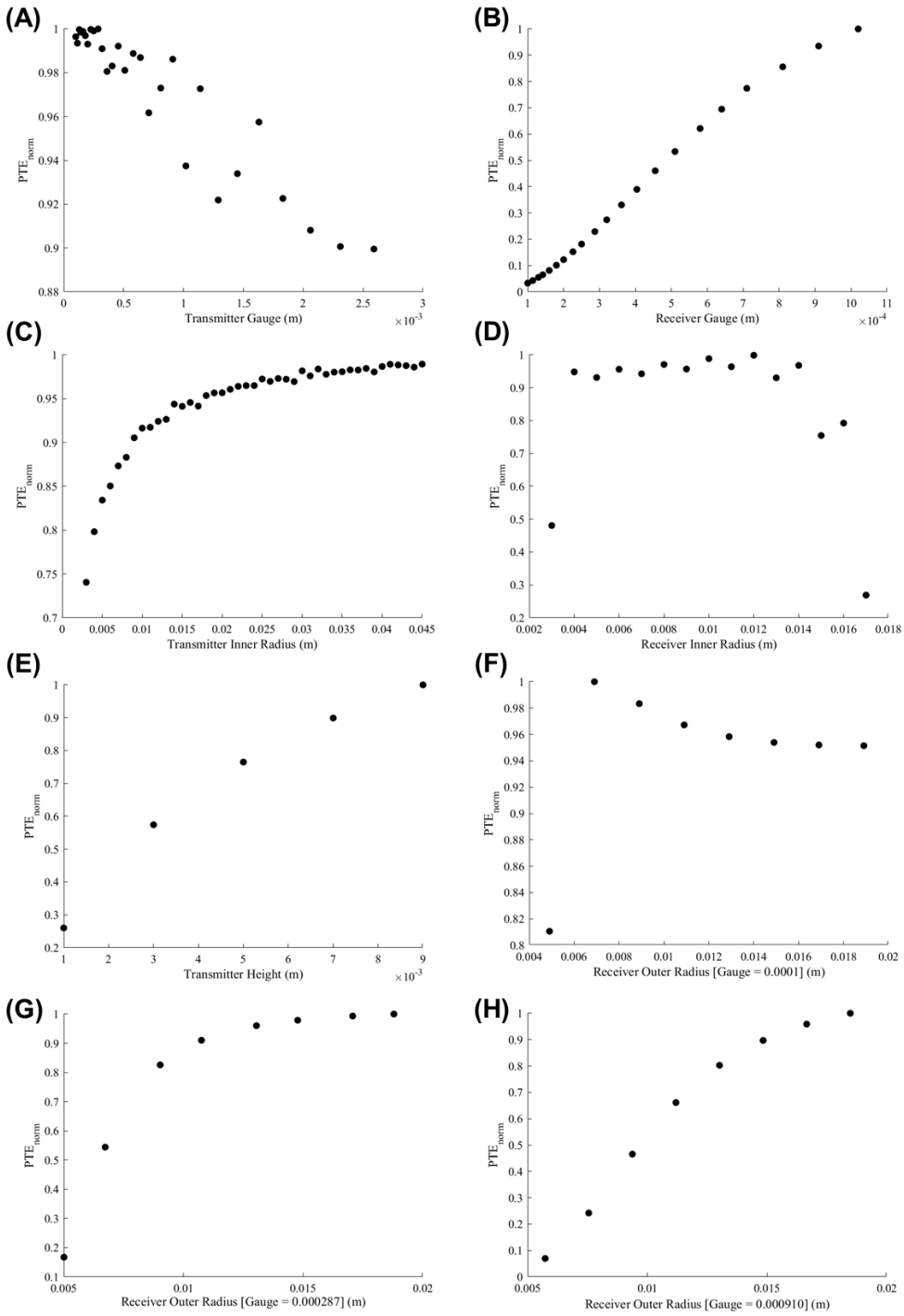

Figure 51: Variable correlations vs. PTE for Multi-Layer with Single Turn transmitter (Tx) coil and Planar with N-Turns receiver (Rx) coil (A) Tx gauge, (B) Rx gauge, (C) Tx inner radius, (D) Rx inner radius, (E) Tx height, (F) Rx outer radius at gauge set to 0.0001, (G) Rx outer radius at gauge set to 0.000287, (H) Rx outer radius at gauge set to 0.000910

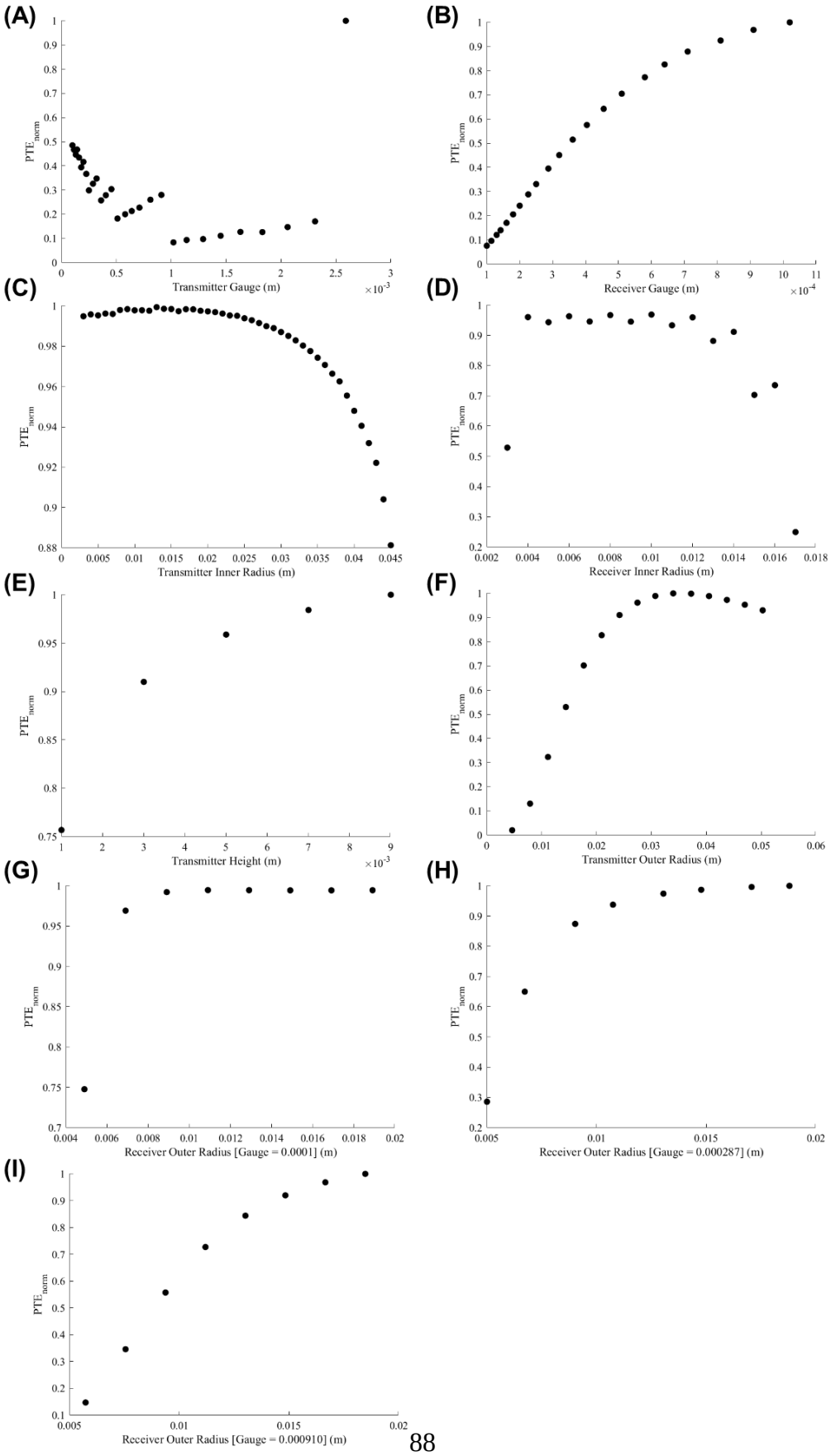
(A)
PTE_norm
Transmitter Gauge (m)
×10^-3
(B)
PTE_norm
Receiver Gauge (m)
×10^-4
(C)
PTE_norm
Transmitter Inner Radius (m)
(D)
PTE_norm
Receiver Inner Radius (m)
(E)
PTE_norm
Transmitter Height (m)
×10^-3
(F)
PTE_norm
Transmitter Outer Radius (m)
(G)
PTE_norm
Receiver Outer Radius [Gauge = 0.0001] (m)
(H)
PTE_norm
Receiver Outer Radius [Gauge = 0.000287] (m)
(I)
PTE_norm
Receiver Outer Radius [Gauge = 0.000910] (m)

Figure 52: Variable correlations vs. PTE for Multi-Layer with N-Turn transmitter (Tx) coil and Planar with N-Turns receiver (Rx) coil (A) Tx gauge, (B) Rx gauge, (C) Tx inner radius, (D) Rx inner radius, (E) Tx height, (F) Tx outer radius, (G) Rx outer radius at gauge set to 0.0001, (H) Rx outer radius at gauge set to 0.000287, (I) Rx outer radius at gauge set to 0.000910

As shown in the correlation plots:

- For changes in transmitter wire gauge, while there is a noticeable trend between wire gauge and PTE, the correlation could not be clearly modeled to a function for any of the three coil geometries.
- For changes in receiver wire gauge, despite variations in transmitter geometries, the correlation remained logarithmic for all three coil geometries.
- For changes in transmitter inner radius, the planar coil with N-turns geometry and the multi-layer coil with N-turns geometry had the same second-order polynomial correlation, but the multi-layer coil with a single turn followed a logarithmic function.
- For changes in receiver inner radius, the system primarily followed a second-order polynomial function for all three coil geometries; however, an outlier was present when the inner radius was very small. This outlier may be a result of increased parasitic capacitance.
- For changes in transmitter height, the correlation was primarily logarithmic for both coil geometries (note: the planar coil with N-turns geometry did not have height correlation analyses).

- For changes in transmitter outer radius, a logarithmic function was again most fitting of the data (note: the multi-layer coil with single-turn geometry did not have outer radius correlation analyses).
- For changes in the receiver outer radius, the correlation was primarily logarithmic with some minor variations between the three coil geometries. An interesting note for the receiver inner radius was the change in the correlation as a result of changes in transmitter wire gauge.

Finally, a sensitivity analysis was performed to determine the variable that resulted in the highest impact on PTE. The sensitivity was computed by calculating the mean of the variance between each data point in the normalized datasets. As shown in **Table IV**, the receiver geometry plays a larger role than the transmitter geometry, with the wire gauge being most important. The importance of the receiver is expected, based on the larger role of its properties on PTE as shown in Equation (13). Furthermore, as also seen in the correlation plots of **Figure 50**, **Figure 51**, and **Figure 52**, wire gauge was shown to impact sensitivity of the receiver outer radius on PTE. As the diameter of the wire decreased, the sensitivity of outer radius on PTE decreased. This effect may be due to the increasing effect of number of turns and coil resistance relative to the impact of coil surface area on PTE. This phenomenon can play a large role in design parameters where there are limitations on the size of the receiver coil.

In the case of the multi-layer coil with N-turns, the transmitter geometry was uniquely shown to have a larger impact on PTE than receiver geometries, with the outer radius revealed to have the largest sensitivity on PTE. This effect may be as a result of the large number of turns possible in the multi-layer coil with N-turns, leading to a largely increasing inductance that overcomes other variable effects.

Table IV: Mean variance between each data point in the normalized dataset demonstrating the sensitivity of change in PTE as a result of change in the selected variable

Tx Coil Type	Planar, N-Turns	Multi-Layer, Single Turn	Multi-Layer, N-Turns
Tx Wire Gauge	0.0301	0.0013	0.0396
Tx Inner Radius	0.0041	0.0037	0.0014
Tx Outer Radius	0.0379	N/A	0.1155
Tx Height	N/A	0.0880	0.0160
Rx Wire Gauge	0.1057	0.1037	0.1030
Rx Inner Radius	0.0647	0.0526	0.0540
Rx Outer Radius	0.0037 [G_2 = 38 AWG] 0.0811 [G_2 = 29 AWG] 0.1103 [G_2 = 19 AWG]	0.0033 [G_2 = 38 AWG] 0.0876 [G_2 = 29 AWG] 0.1198 [G_2 = 19 AWG]	0.0074 [G_2 = 38 AWG] 0.0634 [G_2 = 29 AWG] 0.0975 [G_2 = 19 AWG]

4.1.2. VALIDATION STUDIES

We performed two validation studies on the output of our Monte Carlo simulation. Due to the reliance on approximations for our analytical models, in the first study, we examined the error rate of our outputs by performing a Finite Element Analysis (FEA) using ANSYS Maxwell on the

interaction between the transmitting and receiving coils for one sample in each of the three coil designs (**Figure 53**).

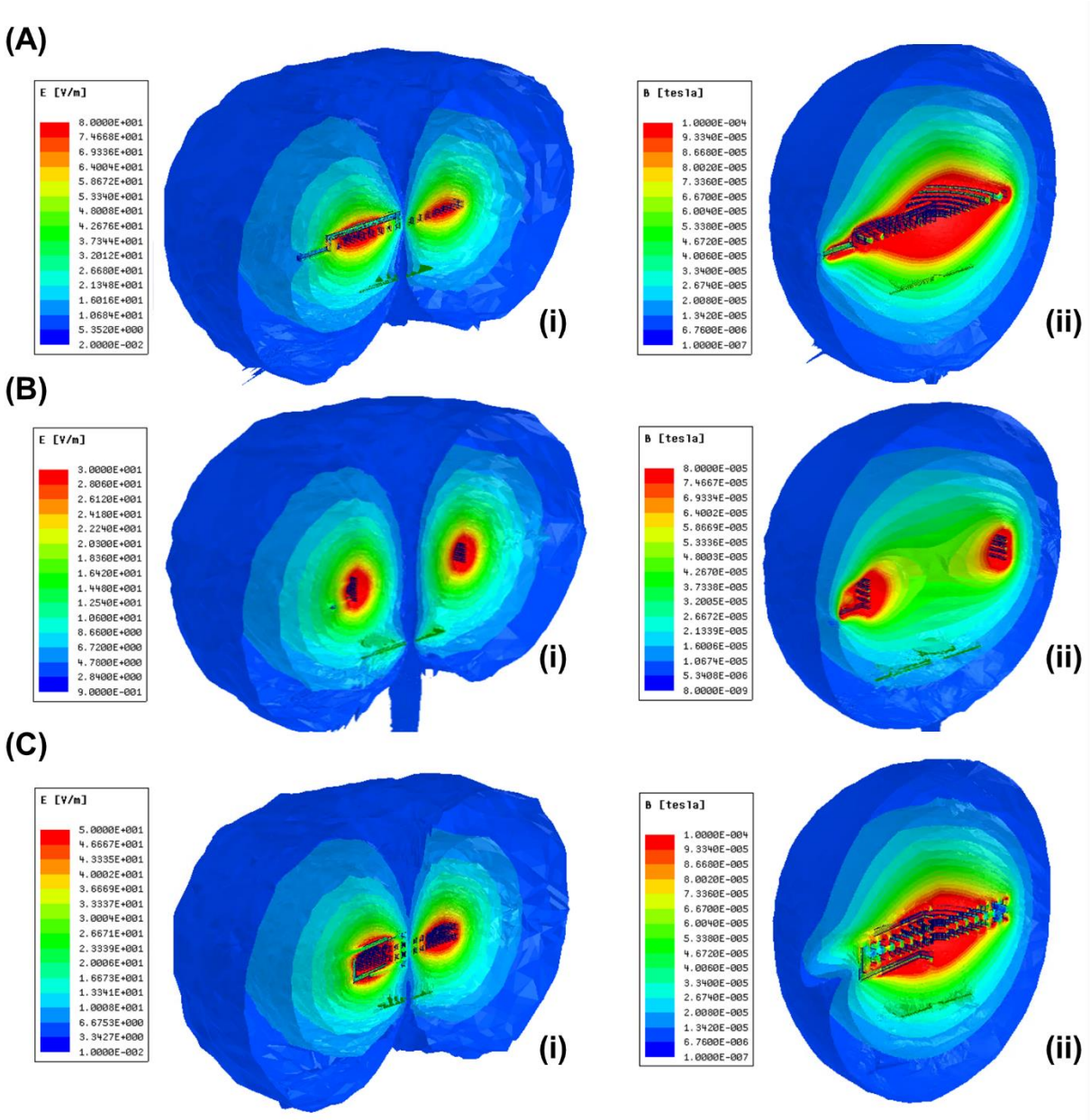

Figure 53: Finite Element Analysis Results. (A) Simulation results for planar coil with N-turns (i) E-field (ii) B-field. (B) Simulation results for multi-layer coil with single turn (i) E-field (ii) B-field. (C) Simulation results for multi-layer coil with N-Turns (i) E-field (ii) B-field.

Percent errors between analytical and numerical models are shown in **Table V**. The largest error is seen with quality factor computations, with the primary effect on Q of the multi-layer coil with N-turns design. This is due to inherent errors in the analytical approximation for coil AC resistance using the Dowell method. This percent error has been shown to be impacted primarily by the operating frequency [69], which was kept constant for all simulations, thus establishing consistency between samples. Furthermore, it is important to note that the primary focus of this optimization study was to determine relative, rather than absolute, impact on PTE, which was the focus of our second validation study.

Table V: Comparison of analytical model results used for Monte Carlo simulation and numerical model results used in ANSYS Maxwell simulations

	Tx: Planar, N-Turns	Rx: Planar, N-Turns
Inductance	2.4%	0.8%
Quality Factor	30.1%	1.7%
Coupling Coefficient	4.9%	
	Tx: Multi-Layer, Single Turn	Rx: Planar, N-Turns
Inductance	0.2%	0.7%
Quality Factor	21.1%	6.7%
Coupling Coefficient	9.7%	
	Tx: Multi-Layer, N-Turns	Rx: Planar, N-Turns
Inductance	2.4%	0.1%
Quality Factor	72.2%	2.7%
Coupling Coefficient	3.1%	

Since nearly 150 million combinations were examined in the optimization analysis, we evaluated the persistence of the same level of accuracy in the remaining datasets using a subsequent validation step. This analysis was performed using the correlation data from above. The variance between each data point in the normalized samples was computed. The variance of these variances was used to validate computational consistency in which a lower value would indicate higher repeatability. The results of this analysis are shown in **Table VI**, indicating reliability throughout the analysis.

Table VI: Variance of sample variance to examine model reliability in which a lower value would indicate higher repeatability.

Tx Coil Type	**Planar, N-Turns**	**Multi-Layer, Single Turn**	**Multi-Layer, N-Turns**
Tx Wire Gauge	1.175×10^{-5}	9.990×10^{-7}	5.732×10^{-5}
Tx Inner Radius	3.231×10^{-5}	1.292×10^{-5}	1.009×10^{-5}
Tx Outer Radius	3.741×10^{-4}	N/A	2.147×10^{-4}
Tx Height	N/A	4.377×10^{-4}	5.275×10^{-4}
Rx Wire Gauge	2.480×10^{-5}	1.162×10^{-5}	7.395×10^{-5}
Rx Inner Radius	5.629×10^{-4}	4.082×10^{-4}	3.586×10^{-4}
Rx Outer Radius	6.790×10^{-8}	1.996×10^{-8}	2.893×10^{-6}

4.2. CHARGING SYSTEM ANALYSIS

As revealed in **Figure 11**, the stimulation unit and subcutaneous unit of the pacemaker function based on intermittent charging intervals from the external unit. Charging frequency and duration are dependent on battery capacity and effective coupling in the CSS. We utilized the LP204965

ultrathin Lithium Polymer rechargeable battery for our pacemaker due to an optimal compromise between size and power capacity. The LP204965 carries a 1100 mAh battery capacity and 3.7 V output with dimensions of 65 mm x 49 mm x 2 mm.

The SSS was estimated to consume 1.04 mW of power based on previous measurements for a patient that requires continuous pacing at 60 BPM [55] in addition to power requirements for an EKG sensor [72] and control circuitry [36]. The full capacity of the battery would thus provide sufficient power for nearly 5.5 months.

Charging duration is dependent on charge rate current, as shown in Equation (27):

$$time\ to\ charge\ (h) = \frac{battery\ capacity\ (Ah)}{charge\ rate\ current\ (A)} \tag{27}$$

The time to charge is thus limited by the coupling efficiency and power output of the inductive power transfer system. To measure this value, coil properties and the coupling coefficient were implemented in the circuit model of **Figure 54** and simulated using PSPICE Electronic Circuit Optimization & Simulation software.

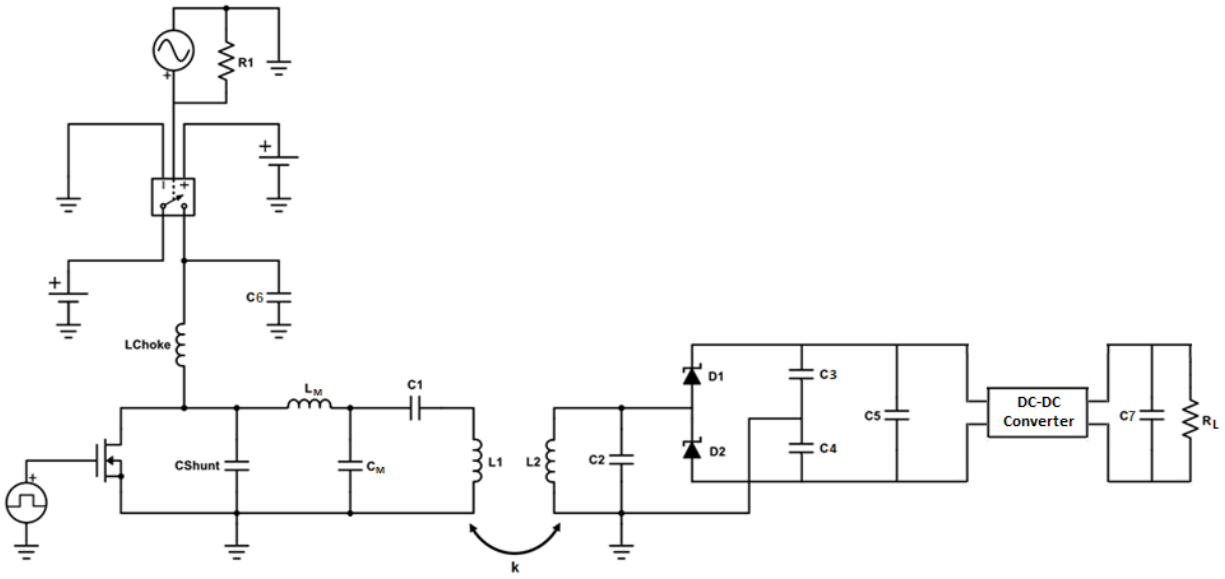

Figure 54: Charging Sub-Unit Circuit Model. The circuit model is simulated in PSPICE software using computed coil properties and coupling coefficient.

Using the system output and Equation (27), an 8-hour charging session was estimated. This session can either be completed once every 5.5 months (e.g. overnight charging) or separated into two 4-hour charging sessions once every 2.5 months depending on patient preference and compliance. It is important to note that these estimations were based on maximum power consumption for a patient that would be in need of continuous pacing with maximum voltage threshold of 5 V at a pulse duration of 1 ms. This is in comparison to the significantly lower average voltage threshold of 0.8 V at pulse duration of 0.5 ms [21], which would result in lower power consumption. Furthermore, artificial pacing would only be activated once an abnormal rhythm is detected. In most patients, this is not continuous, thus further extending battery life.

5. DISCUSSION

For decades, implantable electronics have paved the way for life-changing therapies, including artificial pacing for cardiac rhythm disorders and neural stimulation for movement disorders, gastric mobility, and bladder contraction. However, a fundamental design challenge for implantable devices is the power source and its resulting impact on device size and fixation mechanism. In this work, we presented a system architecture that allowed for long-range wireless power transfer to a small batteryless implant (see **Section 2. Design of a Miniature Pacing System**). The proposed batteryless and wireless pacer thus enabled an unprecedented stent-like intravascular deployment mechanism (**Figure 43**) made only possible by significant device miniaturization and wireless powering. The demonstrated potential for stent-like deployment and fixation can help reduce device failure from exposure to hemodynamic and myocardial contractile forces present in the cardiac chambers.

Due to the need for a small transmitter and receiver device size within anatomical constraints, inductive power transfer systems in medical implants often encounter very low power transfer efficiency that either demands reduction in wireless power transfer range or increase in power transmission that may surpass SAR limits. We circumvented these limitations by implementing a four-coil design (**Figure 11**) consisting of two independent two-coil sub-systems (see **Section 2.2. Three-Tiered Pacemaker Design** and **Section 4. Wireless Power Transfer in Charging Sub-System**).

While various multi-coil architectures have been proposed [49]–[53], their reliance on an interdependent relay system demands continuous presence of all coils for power transmission to the final device (**Figure 8**). To minimize the number of implants and surgical incisions, the

stimulator of the presented system functions entirely independent from the primary power source present in the external unit. This architecture is made possible through the application of remote-controlled power transfer in each sub-system, thus allowing for sufficient wireless power transfer range while avoiding multiple position-limited implants (**Figure 13**).

The control architecture of a wirelessly powered system is fundamental to its application in implantable devices. The control circuitry of most inductive power transfer systems is placed inside the stimulating unit, thus requiring continuous power delivery [16–41]. Two approaches have been sought to address this architecture: (1) direct wireless power transfer (**Figure 6**) or (2) battery-based power delivery (**Figure 7**). The former entails sufficient direct wireless power transfer to satisfy both the internal control circuit and tissue stimulation. This direct transfer requires significant power delivery in the setting of weak coupling between the transmitter and a small-scale receiver, resulting in tissue heating over multi-centimeter ranges. The latter addresses the limitations of direct wireless power at the expense of an integrated battery and, consequently, device size. Thus, currently available inductive power transfer systems demand sacrifice in either size or efficiency (see **Section 1.3.3. Near-Field Wireless Power Transfer**).

In our intravascular pacer, we placed the control circuity for pulse modulation inside the transmitter (**Figure 10**); thus, the solution to size and inefficiency were not forced into mutual exclusivity. Using the transmitter as the primary controller, we compartmentalized the function of the receiver to only a transformation unit that is activated solely during the short period of stimulation. Thus, eliminating the battery mitigated the size issue, and transmitting intermittent wireless pulses compensated for power transfer inefficiency (see **Section 2.1. Remote-Controlled Stimulation**).

Notably, intermittent power delivery allowed for reduced receiver size by tolerating a more weakly-coupled system while supplying sufficient power for stimulation. The tolerance for amplifying wireless power transmission is prominently constrained by SAR limits, which is in turn dependent on the duration of power transfer. Thus, the instantaneous power delivery could be amplified by providing short-length pulses rather than continuous transmissions. The coupling coefficient is impacted by the distance between the interacting coils and their geometry as defined by Equation (5), re-written below:

$$Coupling\ Coefficient = \ k = \frac{r_1^2 r_2^2}{\sqrt{r_1 r_2}\left(\sqrt{r_1^2 + D^2}\right)^3} \cos(\theta)$$

where r_1 is the radius of the transmitter, r_2 is the radius of the receiver, D is the distance between the transmitter and receiver, and θ is the misalignment angle.

A system that tolerates weak coupling thus allows for a small receiver coil (r_2) with a large distance (D) between the transmitter and receiver, rendering our control architecture optimal for biomedical implants which face anatomical constraints and variations. In this context, the anatomic constraint of a coronary vein in the anterior cardiac wall warranted a receiver coil design with < 3 mm diameter. As elucidated in our simulation and bench experiments (see **Section 3.2. Micro-Pacer Translation to Practice**), the resulting power transfer efficiency was measured to be below 10% in response to a combination of displacements and misalignment (**Figure 33**, **Figure 34**, **Figure 35**, and **Figure 41**). Nevertheless, sufficient power for pacing was established while remaining below the SAR limits (**Figure 42**). This outcome enables further increases in power delivery from the transmitter in the setting of anatomical constraints and cardiac motion.

Furthermore, intermittent power transmission in the case of the stimulation sub-system significantly reduced power consumption and tissue absorption by eliminating the majority of power needs through wireless means and relying primarily on wired power transfer for all functions except stimulation (**Figure 9**). Finally, while the inductive power transfer system efficiency is low in both sub-systems and collectively, due to the utilization of intermittent power transfer, sufficient power for a short pulse stimulation is nonetheless achieved to a miniature intravascular implant over a total distance of 55 mm (20 mm SSS and 25 mm CSS) while remaining below SAR limits (**Figure 12**).

6. FUTURE WORK

While our pacer has been circumferentially configured for intravascular deployment to the anterior cardiac vein, further length reduction would allow for navigation through the tortuous coronary anatomy. A reduction in length by ~5 mm would be realized by implementing Complementary Metal-Oxide-Semiconductor (CMOS) [82] integrated chip technology for the receiver circuitry. Furthermore, receiver coil length can be reduced by implementing optimization designs on a parylene-C flexible PCB substrate [83], [84] (**Figure 55**).

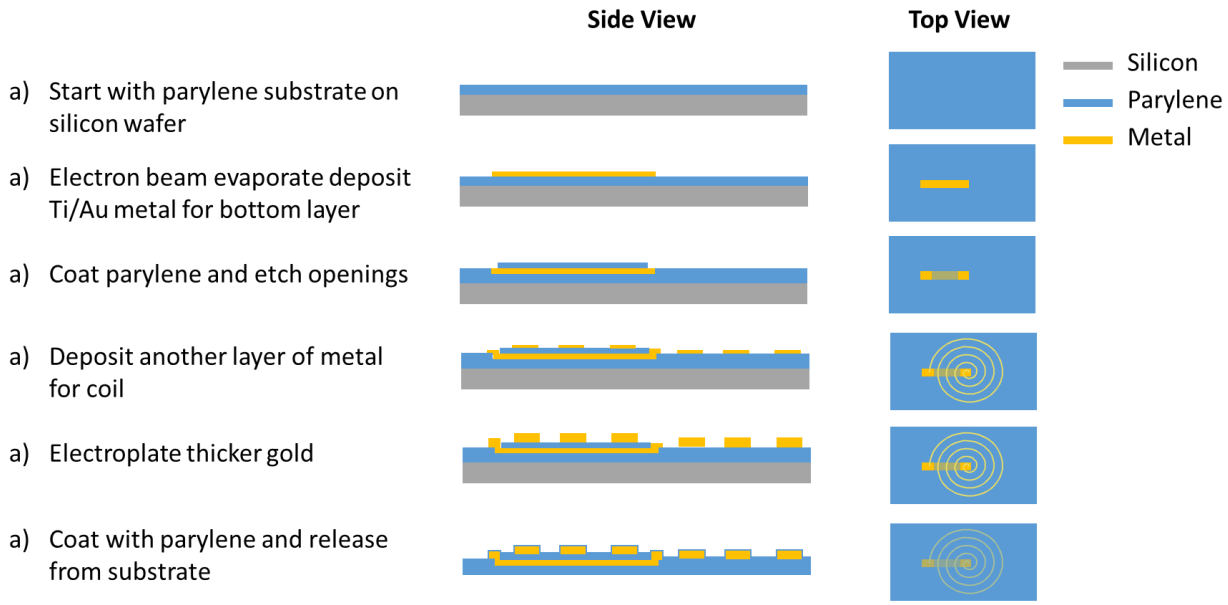

Figure 55: Micro-fabrication process. The receiver coil and circuitry will be placed on a flexible substrate using the illustrated fabrication technique.

We propose three potential design configurations to increase power transfer efficiency within the defined ACV parameters:

(1) Adding a secondary relay coil resonant at 13.56 MHz, positioned opposite to the original receiving coil; the relay coil will focus the magnetic field due to the presence of an intermediate repeater [85] (**Figure 56A**).

(2) Converting to a dual spiral design fabricated as planar coils on two opposing layers of the substrate. Upon folding, the direction of current will be additive. Upon structuring into a cylindrical configuration to circumscribe around the catheter cross-sectional perimeter, both spirals contribute to the magnetic coupling, thus optimizing the coil design within the confines of the ACV. Two-layer fabrication will be implemented to realize the design and an additional via will connect the two coils (**Figure 56B**).

(3) Adding a ferromagnetic material above the receiving coil to increase the magnetic coupling. The ferromagnetic material may be soft iron, ferrite ceramic, or a nanostructured flexible magneto-dielectric material as reported by Tang *et al*. [86]. The ferromagnetic material will be deposited below the copper trace of the coil or across the entire surface area of the substrate underneath the coil tracings (**Figure 56C**).

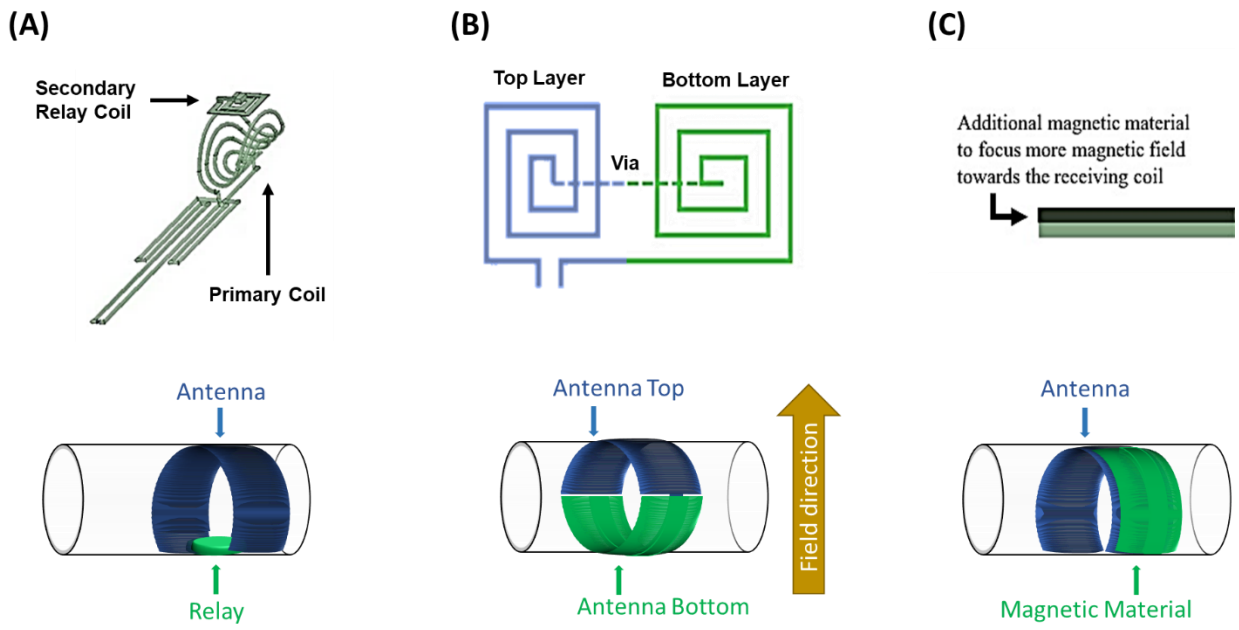

Figure 56: Future Directions. Three design configurations to increase magnetic coupling between the transmitting and receiving coils. (A) An additional relay coil is positioned opposite to the original receiving coil. (B) Two coils with opposite spiral directions increase the magnetic coupling. (C) Additional magnetic material is deposited above the receiving coil to increase the magnetic coupling.

While the proposed pacer was designed for intravascular deployment to the ACV, alternative methodologies for implantation and fixation could be applied. For instance, intravascular fixation in the Great Cardiac Vein (diameter > 8 mm) would allow for an increase in receiver coil size (r_2) to improve efficiency and to facilitate catheter-based intravascular deployment. The proposed design could also be deployed to the right ventricle for endocardial fixation, similar to current pacemaker implantation. By eliminating an integrated battery and reducing device size and mass, the wireless design is able to minimize the risk for dislodgment or embolization. In addition, inductive power transfer systems have the capacity to integrate data transfer on top of the power transmission signal, thus providing the potential to perform multi-chamber pacing and signal encryption [87]–[93].

While the presented work introduces a new direction in wireless stimulation devices, we recognize the prospective roadmap to achieving a clinically viable system. It is important to note, however, that the fundamental design rules established here provide the essential architecture for future technical adaptations. These include (1) adding an EKG sensor and accelerometer in the space-tolerant transmitter for feedback-based pacing, without the need to increase intravascular pacer size; (2) mitigating intra-device thrombosis by treating the surface chemistry with anti-thrombotic coating similar to drug-eluting stents; (3) fabricating electrodes in the form of a ring using a porous structure to engender high impedance electrodes similar to current pacemaker leads; and (4) establishing chronic biocompatible packaging; the transmitter can be packaged using metal encapsulation with feed throughs for the coils [94]; the receiver can be packaged using glass encapsulation [75]–[81], [95] or flexible silicone rubber and oil-based parylene encapsulation [96], [97]. Furthermore, while the current device has been designed via gold-covered copper wiring to optimize biocompatibility, further risk reduction can be achieved with the use of platinum tracings similar to existing pacemaker leads.

7. CONCLUSION

Wireless power transfer through radiofrequency (RF) serves as a promising endeavor in eliminating the need for implanted batteries in medical devices. While some challenges remain in achieving safety and efficacy of a long-term implantable system, novel system designs have presented us with opportunities to eliminate inherent limitations of electromagnetic-based wireless power transfer systems. Device miniaturizations and increases in power transfer efficiency have allowed for new applications in the medical device field, including deep neural implants that necessitate significant size reductions, cardiac implants that must withstand variations from contractile motion, gastrointestinal implants that must withstand challenging environments, and more. In overcoming these challenges, wireless power transfer can meet many of today's unmet clinical needs.

Overall, the successful implementation of the wirelessly powered batteryless pacer presented in this work provides a basis for the development of the next generation of wireless long-term implantable pacemakers, with clinical implications for neural and gastrointestinal stimulation in both the young and elderly populations.

8. APPENDICES

8.1 PERMISSIONS

Below are references to figures obtained through the Creative Commons licensing agreement.

[P1]

Author: Npatchett

Modifications: Yes

License: https://creativecommons.org/licenses/by-sa/4.0/deed.en

[P2]

Author: Gregory Marcus, MD, MAS, FACC

Modifications: No

License: https://creativecommons.org/licenses/by/3.0/deed.en

[P3]

Authors: PJ Bhattacharyya, S Agrawal, JC Barkataky, AK Bhattacharyya

Modifications: No

License: https://creativecommons.org/licenses/by-nc-nd/4.0/

[P4]

Author: Chetvorno

Modifications: Yes

License: https://creativecommons.org/publicdomain/zero/1.0/deed.en

[P5]

9. REFERENCES

[1] H. G. Mond and A. Proclemer, “The 11th world survey of cardiac pacing and implantable cardioverter-defibrillators: Calendar year 2009 - A world society of Arrhythmia’s project,” *PACE - Pacing Clin. Electrophysiol.*, vol. 34, no. 8, pp. 1013–1027, 2011.

[2] R. E. Kirkfeldt, J. B. Johansen, E. A. Nohr, O. D. Jorgensen, and J. C. Nielsen, “Complications after cardiac implantable electronic device implantations: An analysis of a complete, nationwide cohort in Denmark,” *Eur. Heart J.*, vol. 35, no. 18, pp. 1186–1194, 2014.

[3] E. E. Gul and M. Kayrak, “Common Pacemaker Problems : Lead and Pocket Complications,” in *Modern pacemakers - Present and future*, M. R. Das, Ed. InTech, 2011, pp. 299–319.

[4] E. O. Udo *et al.*, “Incidence and predictors of short- and long-term complications in pacemaker therapy: The FOLLOWPACE study,” *Hear. Rhythm*, vol. 9, no. 5, pp. 728–735, 2012.

[5] D. Klug *et al.*, “Systemic infection related to endocarditis on pacemaker leads: clinical presentation and management.,” *Circulation*, vol. 95, no. 8, pp. 2098–107, 1997.

[6] Y. S. Lin *et al.*, “Risk factors influencing complications of cardiac implantable electronic device implantation: infection, pneumothorax and heart perforation: a nationwide population-based cohort study,” *Med.*, vol. 93, no. 27, p. e213, 2014.

[7] R. G. Hauser, W. T. Katsiyiannis, C. C. Gornick, A. K. Almquist, and L. M. Kallinen, “Deaths and cardiovascular injuries due to device-assisted implantable cardioverter-

defibrillator and pacemaker lead extraction," *Europace*, vol. 12, no. 3, pp. 395–401, 2010.

[8] M. R. Myers, V. Parsonnet, and A. D. Bernstein, "Extraction of implanted transvenous pacing leads: A review of a persistent clinical problem," *American Heart Journal*, vol. 121, no. 3 PART 1. pp. 881–888, 1991.

[9] P. J. Bhattacharyya, S. Agrawal, J. C. Barkataky, and A. K. Bhattacharyya, "Medial subclavicular musculotendinous complex and insulation break: Rare cause of late pacemaker lead malfunction," *Indian Heart J.*, 2015.

[10] O. Wazni and B. L. Wilkoff, "Considerations for cardiac device lead extraction," *Nature Reviews Cardiology*. 2016.

[11] J. Sperzel *et al.*, "State of the art of leadless pacing," *Europace*, vol. 17, no. 10, pp. 1508–1513, 2015.

[12] "FDA Executive Summary Memorandum General Issues: Leadless Pacemaker Devices," Gaithersburg, 2016.

[13] "Micra ™ MC1VR01 Clinical Manual," Minneapolis, 2016.

[14] P. Ritter *et al.*, "The rationale and design of the Micra Transcatheter Pacing Study: Safety and efficacy of a novel miniaturized pacemaker," *Europace*, 2015.

[15] R. Borgquist, E. Ljungström, B. Koul, and C.-J. Höijer, "Leadless Medtronic Micra pacemaker almost completely endothelialized already after 4 months: first clinical experience from an explanted heart," *Eur. Heart J.*, 2016.

[16] G. T. Hwang *et al.*, "Self-powered cardiac pacemaker enabled by flexible single crystalline PMN-PT piezoelectric energy harvester," *Adv. Mater.*, vol. 26, no. 28, pp. 4880–4887,

2014.

[17] M. A. Karami and D. J. Inman, “Powering pacemakers from heartbeat vibrations using linear and nonlinear energy harvesters,” *Appl. Phys. Lett.*, vol. 100, no. 4, 2012.

[18] P. Glynne-Jones, S. P. Beeby, and N. M. White, “Towards a piezoelectric vibration-powered microgenerator,” *IEE Proc. - Sci. Meas. Technol.*, vol. 148, no. 2, p. 68, 2001.

[19] R. Tashiro, N. Kabei, K. Katayama, F. Tsuboi, and K. Tsuchiya, “Development of an electrostatic generator for a cardiac pacemaker that harnesses the ventricular wall motion,” *J. Artif. Organs*, vol. 5, no. 4, pp. 239–245, 2002.

[20] A. Auricchio, P. P. Delnoy, F. Regoli, M. Seifert, T. Markou, and C. Butter, “First-in-man implantation of leadless ultrasound-based cardiac stimulation pacing system: Novel endocardial left ventricular resynchronization therapy in heart failure patients,” *Europace*, vol. 15, no. 8, pp. 1191–1197, 2013.

[21] K. L. Lee, “In the wireless era: leadless pacing.,” *Expert Rev. Cardiovasc. Ther.*, vol. 8, no. 2, pp. 171–174, 2010.

[22] S. Ozeri, D. Shmilovitz, S. Singer, and C. C. Wang, “Ultrasonic transcutaneous energy transfer using a continuous wave 650 kHz Gaussian shaded transmitter,” *Ultrasonics*, vol. 50, no. 7, pp. 666–674, 2010.

[23] S. Ozeri and D. Shmilovitz, “Ultrasonic transcutaneous energy transfer for powering implanted devices,” *Ultrasonics*, vol. 50, no. 6, pp. 556–566, 2010.

[24] E. Lefeuvre, S. Risquez, M. Woytasik, M. Deterre, B. Boutaud, and R. Dal Molin, “Energy harvesting devices as long lasting power sources for the next generation pacemakers,” in *2013 25th International Conference on Microelectronics, ICM 2013*, 2013.

[25] H. Ouyang *et al.*, “Symbiotic cardiac pacemaker,” *Nat. Commun.*, vol. 10, no. 1, 2019.

[26] G. M. Djuknic, “Method of measuring a pattern of electromagnetic radiation,” US6657596B2, 2002.

[27] D. M. Pozar, *Microwave Engineering*. 2009.

[28] S. Nikoletseas, Y. Yang, and A. Georgiadis, *Wireless power transfer algorithms, technologies and applications in ad Hoc communication networks*. 2016.

[29] Y. Zeng, B. Clerckx, and R. Zhang, “Communications and Signals Design for Wireless Power Transmission,” *IEEE Trans. Commun.*, 2017.

[30] W. Brown, “Microwave to DC converter,” 1969.

[31] S. Bakogianni and S. Koulouridis, “Sub-1 GHz far-field powering of implantable medical devices: Design and safety considerations,” in *IEEE Antennas and Propagation Society, AP-S International Symposium (Digest)*, 2015, vol. 2015–Octob, pp. 942–943.

[32] C. Liu, Y. X. Guo, H. Sun, and S. Xiao, “Design and safety considerations of an implantable rectenna for far-field wireless power transfer,” *IEEE Trans. Antennas Propag.*, vol. 62, no. 11, pp. 5798–5806, 2014.

[33] Y. Sun, B. Greet, D. Burkland, M. John, M. Razavi, and A. Babakhani, “Wirelessly powered implantable pacemaker with on-chip antenna,” in *IEEE MTT-S International Microwave Symposium Digest*, 2017, pp. 1242–1244.

[34] J. S. Ho *et al.*, “Wireless power transfer to deep-tissue microimplants,” *Proc. Natl. Acad. Sci. U. S. A.*, vol. 111, no. 22, pp. 7974–7979, 2014.

[35] S. Kim, J. S. Ho, L. Y. Chen, and A. S. Y. Poon, “Wireless power transfer to a cardiac

implant," *Appl. Phys. Lett.*, vol. 101, no. 7, pp. 1–5, 2012.

[36] L. S. Y. Wong, S. Hossain, A. Ta, J. Edvinsson, D. H. Rivas, and H. Nääs, "A very low-power CMOS mixed-signal IC for implantable pacemaker applications," *IEEE J. Solid-State Circuits*, vol. 39, no. 12, pp. 2446–2456, 2004.

[37] K. Finkenzeller, *RFID Handbook: Fundamentals and Applications in Contactless Smart Cards, Radio Frequency Identification and near-Field Communication*, Third. Chippenham, Wiltshire, UK: John Wiley & Sons, 2010.

[38] R. F. Cleveland, D. M. Sylvar, and J. L. Ulcek, "Evaluating Compliance with FCC Guidelines for Human Exposure to Radiofrequency Electromagnetic Fields," Washington, D.C., 1997.

[39] W. J. Heetderks, "RF Powering of Millimeter- and Submillimeter-Sized Neural Prosthetic Implants," *IEEE Trans. Biomed. Eng.*, vol. 35, no. 5, pp. 323–327, 1988.

[40] J. A. Von Arx and K. Najafi, "A wireless single-chip telemetry-powered neural stimulation system," *1999 IEEE Int. Solid-State Circuits Conf. Dig. Tech. Pap. ISSCC. First Ed. (Cat. No.99CH36278)*, no. June 1995, pp. 214–215, 1999.

[41] C. R. Neagu, H. V. Jansen, A. Smith, J. G. E. Gardeniers, and M. C. Elwenspoek, "Characterization of a planar microcoil for implantable microsystems," *Sensors Actuators, A Phys.*, vol. 62, no. 1–3, pp. 599–611, 1997.

[42] H. Ali, T. J. Ahmad, and S. A. Khan, "Inductive Link Design for Medical Implants," in *IEEE Symposium on Industrial Electronics and Applications*, 2009, pp. 694–699.

[43] X. Li, C. Y. Tsui, and W. H. Ki, "A 13.56 MHz Wireless Power Transfer System With Reconfigurable Resonant Regulating Rectifier and Wireless Power Control for Implantable

Medical Devices," *IEEE J. Solid-State Circuits*, vol. 50, no. 4, pp. 978–989, 2015.

[44] U. Jow and M. Ghovanloo, "Design and Optimization of Printed Spiral Coils for Efficient Transcutaneous Inductive Power Transmission," *Optimization*, vol. 1, no. 3, pp. 193–202, 2008.

[45] J. Parramon *et al.*, "ASIC-based batteryless implantable telemetry microsystem for recording purposes," in *Engineering in Medicine and Biology Society, 1997. Proceedings of the 19th Annual International Conference of the IEEE*, 1997, vol. 5, pp. 0–2225.

[46] G. Monti, L. Tarricone, and C. Trane, "Experimental characterization of a 434 MHz wireless energy link for medical applications," *Prog. Electromagn. Res. C*, vol. 30, no. June, pp. 53–64, 2012.

[47] S. Y. Lee *et al.*, "A programmable implantable microstimulator soc with wireless telemetry: Application in closed-loop endocardial stimulation for cardiac pacemaker," in *IEEE Transactions on Biomedical Circuits and Systems*, 2011, vol. 5, no. 6, pp. 511–522.

[48] H. M. Lee and M. Ghovanloo, "A power-efficient wireless capacitor charging system through an inductive link," *IEEE Trans. Circuits Syst. II Express Briefs*, vol. 60, no. 10, pp. 707–711, 2013.

[49] A. Kurs, A. Karalis, R. Moffatt, J. D. Joannopoulos, P. Fisher, and M. Soljacic, "Wireless power transfer via strongly coupled magnetic resonances.," *Science*, vol. 317, no. 5834, pp. 83–6, 2007.

[50] M. RamRakhyani, Anil Kumar and Mirabbasi, Shahriar and Chiao, "Design and optimization of resonance-based efficient wireless power delivery systems for biomedical implants," *IEEE Trans. Biomed. Circuits Syst.*, vol. 5, no. 1, pp. 48–63, 2011.

[51] B. Lee, M. Kiani, and M. Ghovanloo, “A Triple-Loop Inductive Power Transmission System for Biomedical Applications,” *IEEE Trans. Biomed. Circuits Syst.*, vol. 10, no. 1, pp. 138–148, 2016.

[52] M. Kiani, U. M. Jow, and M. Ghovanloo, “Design and Optimization of a 3 Coil Inductive Link for Efficient Wireless Power Transmission,” *IEEE Trans. Biomed. Circuits Syst.*, vol. 5, no. 6, pp. 579–591, 2011.

[53] W. Zhong, C. K. Lee, and S. Y. Ron Hui, “General analysis on the use of tesla’s resonators in domino forms for wireless power transfer,” *IEEE Trans. Ind. Electron.*, vol. 60, no. 1, pp. 261–270, 2013.

[54] E. Astrinsky and S. Furman, “Pacemaker Output Programming for Maximum Safety and Maximum Longevity,” *J. Cardiovasc. Electrophysiol.*, vol. 1, no. 1, pp. 51–58, 1983.

[55] P. Abiri *et al.*, “Inductively powered wireless pacing via a miniature pacemaker and remote stimulation control system,” *Sci. Rep.*, vol. 7, no. 1, 2017.

[56] M. Kiani and M. Ghovanloo, “A figure-of-merit for designing high-performance inductive power transmission links,” *IEEE Trans. Ind. Electron.*, vol. 60, no. 11, pp. 5292–5305, 2013.

[57] S. C. Q. Chen and V. Thomas, “Optimization of Inductive RFID Technology,” *Int. Symp. Electron. Environ.*, no. 2, pp. 82–87, 2001.

[58] S. S. Mohan, M. D. M. Hershenson, S. P. Boyd, and T. H. Lee, “Simple accurate expressions for planar spiral inductances,” *IEEE J. Solid-State Circuits*, vol. 34, no. 10, pp. 1419–1420, 1999.

[59] J. P. Sun, X. S. Yang, Y. Y. Lam, M. J. Garcia, and C. M. Yu, “Evaluation of Coronary

Venous Anatomy by Multislice Computed Tomography," *World J. Cardiovasc. Surg.*, vol. 2, no. 4, pp. 91–95, 2012.

[60] D. M. Dobkin, *The RF in RFID*. Burlington: Elsevier Inc., 2008.

[61] H. M. Madjar, "International, regional and national regulation of SRDs ISM Bands," in *ITU Workshop on Short Range Devices and Ultra Wide Band*, 2014, no. June, pp. 1–35.

[62] M. Grandolfo, P. Vecchia, and O. P. Gandhi, "Magnetic Resonance Imaging: Calculation of Rates of Energy Absorption by a Human-Torso Model," *Bioelectromagnetics*, vol. 11, pp. 117–128, 1990.

[63] A. Hennig and G. vom Bogel, "Analysis of Power Absorption by Human Tissue in Deeply Implantable Medical Sensor Transponders," in *Advanced Microwave Circuits and Systems*, V. Zhurbenko, Ed. InTech, 2010, pp. 407–420.

[64] N. O. Sokal, "Class-E RF Power Amplifiers," *QEX Commun. Quart*, vol. 204, pp. 9–20, 2001.

[65] H. Kristiansen, T. Hovstad, G. Vollan, and S. Faerestrand, "Right ventricular pacing and sensing function in high posterior septal and apical lead placement in cardiac resynchronization therapy," *Indian Pacing Electrophysiol. J.*, vol. 12, no. 1, pp. 4–14, 2012.

[66] "Tendril SDX Active fixation pacing leads User's Manual," Sylmar, CA, 2013.

[67] A. Abiri *et al.*, "Simulating Developmental Cardiac Morphology in Virtual Reality Using a Deformable Image Registration Approach," *Ann. Biomed. Eng.*, vol. 46, no. 369, pp. 1–12, 2018.

[68] S. J. Seol, H. Cho, D. H. Yoon, and S. H. Jang, "Appropriate depth of needle insertion

during rhomboid major trigger point block," *Ann. Rehabil. Med.*, vol. 38, no. 1, pp. 72–76, 2014.

[69] Xi Nan and C. R. Sullivan, "An improved calculation of proximity-effect loss in high-frequency windings of round conductors," in *IEEE 34th Annual Conference on Power Electronics Specialist*, 2003, pp. 853–860.

[70] V. G. Welsby, *The Theory and Design of Inductance Coils*. John Wiley and Sons, Inc, 1960.

[71] F. W. Grover, "Inductance Calculations: Working Formulas and Tables," *Instrum. Soc. Am.*, 1946.

[72] D. Jeon *et al.*, "An Implantable 64nW ECG-Monitoring Mixed-Signal SoC for Arrhythmia Diagnosis," in *IEEE International Solid-State Circuits Conference Digest of Technical Papers (ISSCC)*, 2014, pp. 416–418.

[73] S. Cruciani, T. Campi, F. Maradei, and M. Feliziani, "Numerical simulation of Wireless Power Transfer system to recharge the battery of an implanted cardiac pacemaker," in *IEEE International Symposium on Electromagnetic Compatibility*, 2014, pp. 44–47.

[74] A. Sani, A. Alomainy, and Y. Hao, "Numerical characterization and link budget evaluation of wireless implants considering different digital human phantoms," *IEEE Trans. Microw. Theory Tech.*, vol. 57, no. 10, pp. 2605–2613, 2009.

[75] G. E. Loeb, C. J. Zamin, J. H. Schulman, and P. R. Troyk, "Injectable microstimulator for functional electrical stimulation," *Med. Biol. Eng. Comput.*, 1991.

[76] T. Cameron, G. E. Loeb, R. A. Peck, J. H. Schulman, P. Strojnik, and P. R. Troyk, "Micromodular implants to provide electrical stimulation of paralyzed muscles and limbs," *IEEE Trans. Biomed. Eng.*, 1997.

[77] X. Huang, K. Zheng, S. Kohan, P. M. Denprasert, L. Liao, and G. E. Loeb, "Neurostimulation Strategy for Stress Urinary Incontinence," *IEEE Trans. Neural Syst. Rehabil. Eng.*, 2017.

[78] G. E. Loeb *et al.*, "Design and testing of a percutaneously implantable fetal pacemaker," *Ann. Biomed. Eng.*, 2013.

[79] Y. Bar-Cohen *et al.*, "Preclinical testing and optimization of a novel fetal micropacemaker," *Hear. Rhythm*, 2015.

[80] A. N. Vest *et al.*, "Design and Testing of a Transcutaneous RF Recharging System for a Fetal Micropacemaker," *IEEE Trans. Biomed. Circuits Syst.*, 2017.

[81] Y. Bar-Cohen *et al.*, "Minimally Invasive Implantation of a Micropacemaker into the Pericardial Space," *Circ. Arrhythmia Electrophysiol.*, 2018.

[82] F. M. Wanlass, "Low Stand-By Power Complementary Field Effect Circuitry," *US Pat. 3,356,858*, 1967.

[83] P. Chen, W. Kuo, W. Li, Y. Yang, and Y. Tai, "Q-Enhanced Fold-and-Bond MEMS Inductors," in *3rd IEEE International Conference on Nano/Micro Engineered and Molecular Systems*, 2008, pp. 869–872.

[84] P. J. Chen, S. Saati, R. Varma, M. S. Humayun, and Y. C. Tai, "Implantable flexible-coiled wireless intraocular pressure sensor," in *Proceedings of the IEEE International Conference on Micro Electro Mechanical Systems (MEMS)*, 2009.

[85] J. Besnoff, M. Abbasi, and D. Ricketts, "Ultra-high Data-rate Communication and Efficient Wireless Power Transfer at 13.56 MHz," *IEEE Antennas Wirel. Propag. Lett.*, vol. 16, pp. 1–1, 2017.

[86] Y. Tang, B. Lee, M. Vural, P. Kofinas, and A. Khaligh, “Toward flexible ferromagnetic-core inductors for wearable electronic converters,” *IEEE Appl. Power Electron. Conf. Expo. - APEC*, pp. 2540–2545, 2015.

[87] H. Lyu *et al.*, “Leadless multisite pacing: A feasibility study using wireless power transfer based on Langendorff rodent heart models,” *J. Cardiovasc. Electrophysiol.*, 2018.

[88] L. Bereuter *et al.*, “Leadless Dual-Chamber Pacing,” *JACC Basic to Transl. Sci.*, vol. 3, no. 6, p. 813 LP-823, Dec. 2018.

[89] V. Morrill, “Sub-Miniature Fuse,” 5,027,101, 1991.

[90] Z. Zhang, K. T. Chau, C. Liu, C. Qiu, and F. Lin, “An efficient wireless power transfer system with security considerations for electric vehicle applications,” *J. Appl. Phys. 115*, vol. 115, no. 17, 2014.

[91] Z. Zhang, K. T. Chau, C. Qiu, and C. Liu, “Energy Encryption for Wireless Power Transfer,” *IEEE Trans. Power Electron.*, vol. 30, no. 9, pp. 5237–5246, 2015.

[92] J. D. Dunworth, R. W. Martin, M. B. Selby, D. Maldonado, K. H. El-Maleh, and Y. Karmi, “Systems and methods for selective wireless power transfer,” 8,547,057, 2013.

[93] S. Leng, D. Wing, K. Ng, and R. Schober, “Power Efficient and Secure Multiuser Communication Systems with Wireless Information and Power Transfer,” in *IEEE International Conference on Communications Workshops (ICC)*, 2014, pp. 800–806.

[94] P. Falabella, H. Nazari, P. Schor, J. D. Weiland, and M. S. Humayun, “Argus® II Retinal Prosthesis System BT - Artificial Vision: A Clinical Guide,” V. P. Gabel, Ed. Cham: Springer International Publishing, 2017, pp. 49–63.

[95] J. Halamka, A. Juels, A. Stubblefield, and J. Westhues, “The Security Implications of VeriChip Cloning,” *J. Am. Med. Informatics Assoc.*, 2006.

[96] A. Shapero, Y. Liu, and Y. C. Tai, “Parylene-on-oil packaging for implantable pressure sensors,” in *Proceedings of the IEEE International Conference on Micro Electro Mechanical Systems (MEMS)*, 2016.

[97] A. Shapero and Y.-C. Tai, “Parylene-oil-encapsulated low-drift implantable pressure sensors,” in *2018 IEEE Micro Electro Mechanical Systems (MEMS)*, 2018, pp. 47–50.